Entwicklung neuer Modelle zur Beschreibung von Schüttgutströmungen in Wanderbettwärmeübertragern

Von der Fakultät Energie-, Verfahrens- und Biotechnik der Universität Stuttgart zur Erlangung des akademischen Grades eines Doktors der Ingenieurwissenschaften (Dr.-Ing) genehmigte Abhandlung

Vorgelegt von

Philipp Bartsch
aus Würzburg

Hauptberichter: Prof. Dr. André Thess
Mitberichter: Prof. Dr.-Ing. Prof. E.h. Peter Eberhard

Tag der mündlichen Prüfung: 09/06/2020

Institut für Gebäudeenergetik, Thermotechnik und Energiespeicherung der Universität Stuttgart

2020

Eingeständigkeitserklärung

Ich versichere, dass ich die vorliegende Arbeit selbständig verfasst und keine anderen als die angegebenen Quellen und Hilfsmittel benutzt habe; aus fremden Quellen entnommene Passagen und Gedanken sind als solche kenntlich gemacht.

Name: _____

Unterschrift: _____

Datum: _____

Kurzfassung

Granulare Medien weisen viele Eigenschaften auf, die ihre Verwendung als Wärmeträger- und Wärmespeicher in Solarthermischen Kraftwerken oder Industrieprozessen nahe legen. Wanderbettwärmeübertrager (WBWÜ) mit horizontalen Rohren bieten sich dabei an, um thermische Energie aus heißen Schüttgütern auszukoppeln. Ihre thermische Leistungsfähigkeit wird durch das komplexe, granulare Strömungsprofil im Apparat bestimmt. Daher werden präzise Simulationsmodelle benötigt, um eine Grundlage für neuartige Entwurfswerkzeuge zu bilden.

In dieser Arbeit wird ein Kontinuum-Modell entwickelt, welches die Berechnung des Strömungsfeldes und Wärmetransports in einem WBWÜ ermöglicht. Ergänzend werden Simulationen mit Hilfe eines partikel-diskreten Modells durchgeführt, welches Einblick in Strömungsphänomene gewährt, welche sich auf Ebene der Einzelpartikel abspielen. Ein Fokus der Modellierungsarbeiten ist die genaue Abbildung der leistungsbestimmenden Phänomene.

Beide Modelle sagen übereinstimmend die Bildung einer Stauzone auf dem Rohrscheitel voraus. Unterhalb des Rohres beginnen die Partikel sich von der Rohroberfläche abzulösen und bilden eine Leerzone. Dieser Effekt wird nur durch das partikeldiskrete Modell, nicht aber durch das Kontinuum-Modell erfasst. Um die daraus resultierende Verringerung des Wärmeübergangs zu berücksichtigen wird das Kontinuum-Modell modifiziert.

Die Simulationsergebnisse zum Strömungsfeld werden anhand von optischen Messungen an einem transparenten Wärmeübertrager-Mockup validiert. Die Simulationsergebnisse zum lokalen Wärmeübergang am Einzelrohr werden ebenfalls mit Messdaten verglichen, wobei die Massenstromdichte, die Korngröße und die Rohranordnung variiert werden.

Der Einfluss der Partikelgröße und Massenstromdichte auf den Wärmeübergang wird vom Kontinuum-Modell gut erfasst. Die Abweichungen zwischen Modell und Experiment hinsichtlich des mittleren Wärmeübergangskoeffizienten am Rohr liegen bei weniger als 20 %.

Anhand des partikeldiskreten Modells wird die Abhängigkeit des granularen Strömungsfeldes von unterschiedlichen Einflussgrößen untersucht. Es zeigt sich, dass sich

die Größe und Ausdehnung der Stauzone signifikant durch die Rohranordnung beeinflussen lässt. Gleiches gilt für die Position in der unteren Rohrhälfte, an der die Partikel beginnen, sich von der Rohroberfläche abzulösen.

Die Ausdehnung der Stauzone hängt zusätzlich vom Oberflächenreibungskoeffizient der Rohrwand ab. Andere Größen wie die Massenstromdichte und die innere Reibung der Schüttung zeigen einen geringen Einfluss auf das Strömungsmuster.

Anhand dieser Erkenntnisse wird eine vereinfachte Beschreibung des Wärmeübergangs zwischen einem horizontalen Rohr und einer Schüttung entwickelt. Das vereinfachte Modell wird den Messergebnissen des mittleren Wärmeübergangskoeffizienten am Rohr gegenübergestellt wobei Abweichungen von weniger als 13 % auftreten.

Die Ergebnisse der Arbeit zeigen damit eine deutliche Verbesserung gegenüber bestehenden Modellen, wie dem von Baumann [1], Niegsch [2] oder Schlünder [3], die jeweils eine Abweichung von 40 bis 50 % bezogen auf die experimentellen Daten aufweisen.

Diese Arbeit behandelt somit die im WBWÜ ablaufenden thermophysikalischen Vorgänge auf unterschiedlichsten Detaillierungsgraden und Modellierungsebenen. Sie liefert damit einen wichtigen Beitrag zum kosteneffizienten Einsatz granularer Wärmeträgermedien in solarthermischen Kraftwerken als Teil einer nachhaltigen Energieversorgung. Teile dieser Arbeit wurden in referierten Fachzeitschriften veröffentlicht [4] [5].

Abstract

Granular materials offer many advantages which qualify them for use as heat transfer medium and heat storage material in solar thermal power plants and industrial processes. Moving bed heat exchangers (MBHE) with horizontal tubes are favorable to extract thermal energy from hot granular materials. Their thermal performance is determined by a complex granular flow field in the device. This calls for accurate simulation models on which novel design tools can be based.

In this work a continuum model is developed to calculate the granular flow field and heat transport in a MBHE. The model is supplemented by simulations using a discrete-particle model which provides insight into flow phenomena occuring on the particle level.

Both models agree in predicting the formation of a stagnant area at the top of the tubes. Below the tubes, the particles start to separate from the tube surface and form a void area. This phenomenon is captured only by the discrete particle model but not by the continuum model. To account for the resulting decrease in heat transfer in this area, the continuum model is modified.

The simulation results of the granular flow field are validated based on optical measurements in a transparent heat exchanger mockup. Furthermore, the local heat transfer coefficient at a single tube is examined in detail, varying the mass flow rate, grain size and the tube arrangement.

The continuum model well captures the influence of the mass flow rate and the grain size on the heat transfer rate. The averaged heat transfer coefficient per tube predicted by the continuum model deviates by less than 20 % from the measured results.

Using the discrete particle model, the dependence of the granular flow field on different influencing parameters is studied. It is determined that the size and extent of the stagnant zone can be significantly influenced by the tube arrangement. The same goes for the position in the lower half of the tube where the particles start to detach themselves from the tube surface.

In addition the extent of the stagnant zone depends on the surface friction of the tube wall. Other parameters, like the inner friction of the bulk and the mass flow rate show little influence on the flow pattern.

Based on these findings, a simplified description of the heat transfer between a horizontal tube and a moving bulk is developed. A comparison of the results of the simplified model with the measured data of the averaged heat transfer coefficient per tube shows the deviation to be less than 13 %.

The results of this work show significant enhancement compared to existing models such as the one of Baumann [1], Niegsch [2] or Schlünder [3], who exhibit deviations of 40 to 50 % from the experimental data.

This work hence analyzes the thermo-physical phenomena of a MBHE on different levels of detail and length scale. Its results contribute to a sustainable future energy supply by promoting the cost-efficiency of solar thermal power plants with granular heat transfer fluids. Parts of this work have been presented in journal publications [4] [5].

Table of contents

List of abbreviations

Abbreviations

CAES	Compressed air energy storage
CFD	Computational fluid dynamics
CSP	Concentrating solar power
CV	control volume
D	dimension
DEM	Discrete element method
ED	Event-driven method
EOS	Equation of State
Exp	experiment, experimental
KTGF	Kinetic theory of granular fluids
MBHE	Moving bed heat exchanger
MD	Molecular dynamics
NSCD/CD	(Non-smooth) contact dynamics method
PE	Polyethylene
PIV	Particle image velocimetry
PT	Particle tracking (velocimetry)
px	Pixel
Sim	simulation
TA	Tube arrangement
TC	Thermopcouple
TES	Thermal energy storage

Symbols

a	'shape parameter' of stagnant zone in equation (40)
A	area
b	width/breadth
C_{12}	radiation coefficient
C_D	Coefficient in equation (10)
c_p	specific heat
C_s	Stefan-Boltzmann constant
d	particle diameter
$\boldsymbol{D}$	rate of deformation tensor

D_T	outer tube diameter
e	coefficient of restitution
E	Youngs modulus
$\boldsymbol{F}$, F	force vector, magnitude of force
g	acceleration due to gravity
Gr	Grashof number
h	specific enthalpy
H	height
h_R	(total) surface roughness (see equation (20))
I	electric current, unit tensor
I_s	inertial number
J	inertia troque
k	contact stiffness
Kn	Knudsen number
l	mean free path of gas molecules, length (see equation (67) and equation (60))
m	mass
$\boldsymbol{M}$	torque, moment
$\dot{m}$	mass flow rate
M_f	molecular mass of fluid molecules
$\boldsymbol{n}$	unit normal vector
N	number
Nu	Nusselt Number
p	pressure
P	Power
pp	particle-particle
Q	particulate quantity averaged per control volume (see equation (34))
$\dot{q}$	heat flux, heat transfer rate
R	ohmic/thermal resistance, radius
r,s	exponents in equation (14)
Ra	Rayleigh number
Re	Reynolds number
Re_p	Reynolds Number per particle diameter
R_g	universal gas constant
s	spacing between tubes, overlap between particles (see section 4.2.1)
$\boldsymbol{S}$	deviatoric part of the rate of deformation tensor

t	residence time, time step ‘t’ (superscript)
T	Temperature
T_0	’reduced’ temperature at wall due to thermal contact resistance (see equation (17))
$\boldsymbol{u}$, u	velocity vector, magnitude of velocity vector
V	volume
α	heat transfer coefficient
β	interphase drag coefficient
γ	accomodation coefficient (see equation (75) and (76))
δ	gap width between wall and contacting particle surface
Δ	Delta (difference)
ε	volume fraction
ε_1, ε_2	emission coefficients of wall and bulk
ε_{max}	closest random packing (maximum packing fraction in frictional regime)
ε_{min}	loosest random packing (minimum packing fraction in frictional regime)
λ	thermal conductivity
μ	friction coefficient, shear viscosity
ν	kinematic viscosity
ρ	density
$\boldsymbol{\sigma}$	stress tensor
$\boldsymbol{\tau}$, τ	shear stress tensor, shear stress (scalar)
φ	fraction of (tube) surface covered by particles (see equation (18))
ϕ_i	internal friction angle
ϕ_r	angle of repose
ω	angular position (at tube surface)

Indices

abs	absolute deviation/error
av	average
c	contact
con	conduction
d	dynamic
e	elastic
el	electric
fr	frictional regime

front	front side of simulation geometry (see Figure 11)
fs	interfacial exchange quantity between phases (equation (12))
g	gas phase
H	horizontal
i	internal quantity of the bulk
i,j	substitutes for gas and solid phase
l, ul	loading,unloading case
lim	limiting value
loc	local
m	mean
min	minimum
n	normal direction
p	particle
rad	radiativ, radial
rear	rear side of simulation geometry (see Figure 11)
ref	reference quantity
rel	relativ
roll	rolling
s	solid phase, static
S0	bulk property
sep	’separate’ – point at the tube surface where particles start to detach
sl	’sliding’
SZ	stagnant zone
t	tangential
V	Vertical
VZ	void zone
w	weighting factor (see equation (34))
W	(tube) wall
WP	’wall-particle’

1 Introduction

The steadily increasing demand for electrical and thermal energy by the world population and the associated consequences for our environment and climate are one of the greatest challenges of our time. Although the energy demand is rising more slowly than in the past (2017), it is expected to expand by 30 % between now and 2040 [6]. On the other hand there is consensus both in politics and science that the rise of the average global temperature must be limited to 2 °C ("two-degree target") to prevent irreversible damage to the environment and society [7].

The energy sector accounts for the major part of CO_2-emissions and thus decarbonization of this sector is a vital requirement to meet the above target. To this end, renewable energy technologies need to be further developed. However, the fluctuating availability of wind and sun constitutes a challenge to a flexible and adjustable power supply.

Therefore, these technologies need to be combined with energy storage systems to ensure a secure electricity supply from these renewable sources. Appropriate energy storage systems need to offer high capacities and high powers, long storage times at small losses and short reaction times.

In this situation, thermal energy storage (TES) systems can be a key technology and a central element in several emerging applications: They are the main component in pumped heat electricity storage (PHES) systems. They can also be used to increase the efficiency and the flexibility of other storage technologies (e.g. CAES systems [8]), of industrial processes or of power plants. Common examples can be found in steel industries, where high temperature heat storage systems recuperate excess heat from blast furnaces thus reducing the overall energy consumption. With respect to power generation, TES systems are considered for increasing the flexibility of conventional thermal power plants [9].

TES systems are an integral part of concentrating solar power (CSP) plants, ensuring a demand-oriented electricity production. This type of power plant converts the solar irradiance into thermal energy at a high temperature level which facilitates the integration of heat storage.

Commonly used TES-concepts for CSP plants are based on molten salts or solid materials [10]. Solid materials allow high operating temperatures but need a secondary heat

transfer fluid to charge/discharge thermal energy to/from the storage. Molten salts, on the other hand, can be used both as heat transfer fluid and storage material. However, currently available and cost-effective materials like the commonly used “solar salt” are chemically stable only up to about 550 °C and exhibit a melting point around 200 °C [11].

A further promising alternative is to use flowable, fine grained solid materials which can serve both as a heat transfer fluid and a storage material in the power plant (see Figure 1, left). Such concepts were already proposed in the 1980s [12] [13] [14]. Thus, high operating temperatures are feasible using cost-effective materials, such as natural stones like quartz sand or sintered bauxite particles [15], while no (gaseous) secondary fluid is needed.

Besides the receiver, a key component of such a CSP plant is a particle heat exchanger which is used to discharge the thermal energy from the bulk and transfer it to the working fluid of the power cycle. To this end, different alternatives like rotary kilns, fluidized beds and moving beds have been assessed [1]. Moving bed heat exchangers (MBHE, Figure 1, right) are considered a most promising option due to their low parasitic loads, compact design, low investment cost and little need for maintenance and adjustment controls [16].

In a MBHE the granular material slowly moves in a vertical direction, driven by gravity. Immersed in the moving bed are heat-transferring surfaces such as tubes or plates.

The design of a robust and efficient MBHE relies on detailed knowledge of the fluid- and thermodynamic processes inside the unit. In particular, the effects of the particle flow on the device’s thermal performance are determining. Therefore the aim of the present work is to provide insight into the governing phenomena and to constitute a sound basis for the design and optimization of MBHE.

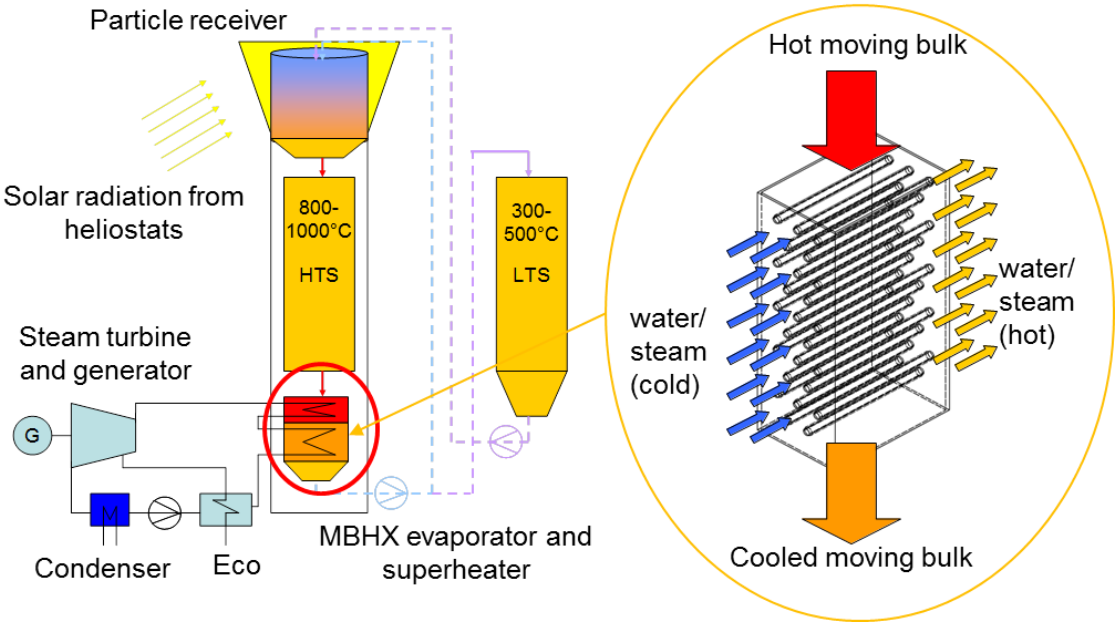

Figure 1. Left: Schematic of solar thermal power plant with granular heat transfer fluid and particle steam generator (HTS = High Temperature Storage, LTS = Low Temperature Storage) [1]. Right: Schematic of moving bed heat exchanger.

2 State of the art

Granular materials display a variety of intriguing features. Most notably, they can exhibit different states of matter, i.e. they can behave like a liquid, a gas, or like a rigid body depending on the way they are handled [17]. This behavior as well as other complex phenomena leads to challenges regarding the description and modelling of granular materials. Furthermore, granular materials usually form a two-phase system. The interstitial fluid between the particles may have considerable impact on the motion, the heat transport and the thermodynamic properties of the bulk.

The following section gives an overview of modelling approaches for granular materials in general. Subsequent to this, prior work specifically related to the heat transfer and flow in moving packed beds is reviewed.

2.1 Modelling of granular flows

Models for the description of granular materials fall into two general groups: Discrete particle models and continuum models. While the former treat the material as collection of distinct particles, continuum models treat it as a continuous medium.

Due to high computational effort, discrete particle models are restricted to relatively small geometries and particle numbers. However, they require no macroscopic input parameters such as the angle of repose. Instead, these macroscopic parameters can be extracted from the simulation as a result of the particle properties like friction and shape [18] [19]. Therefore, discrete particle simulations are a powerful tool to gain insight in the “microscopic” processes on the grain level and can be well combined with continuum models which are applicable to engineering scale geometries but require further information about the macroscopic behavior of the bulk material.

The following sections give a brief overview of the two types of models with a focus on their application in moving bed heat exchangers.

2.1.1 Discrete particle models

Cundall and Strack [20] were the first who introduced a discrete particle approach to model the movement and interaction forces of rock masses and granular materials. Their

approach became known as the discrete element method (DEM) and was very similar in spirit to the so-called molecular dynamics (MD) approach which had been introduced earlier (e.g. [21]). The DEM differs from MD in that the particles are no point masses but possess a finite volume. Both methods evaluate the trajectories of the particles based on the Newtonian equations of motion.

The interaction forces are calculated based on a small (virtual) overlap between particles which is interpreted as an elastic deformation of the particles. The method therefore is also called 'soft particle' method. To translate the overlap into interaction forces, several contact force models were proposed such as continuous potential models (e.g. [22]), linear (e.g. [23]) and non-linear (e.g. [24]) viscoelastic models and hysteretic models (e.g. [25]) for the normal contact forces and linear and non-linear tangential force models (see e.g. [26] for an overview of available models). The geometrical relations of two interacting particles according to the DEM method are illustrated in Figure 1.

The evaluation of the contact forces requires a very fine time step to resolve the small time and length scales involved in the contact interactions.

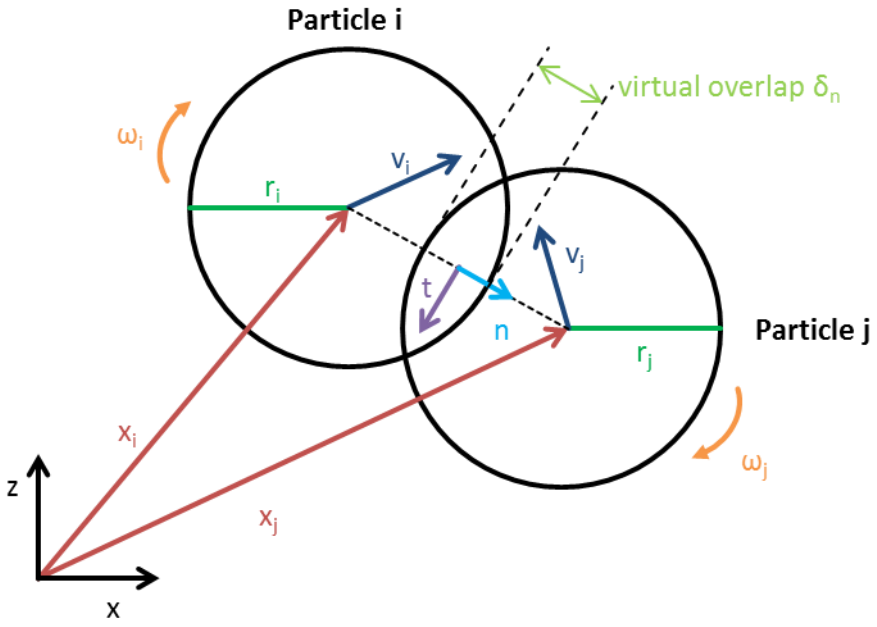

Figure 2. Schematic of DEM method: Geometrical relations between two interacting particles [27].

The DEM has become very popular in the last decades due to the rapid increase of available computational power. It has been used to investigate the behavior of particu-

late solids in different fields such as agricultural [28], chemical, pharmaceutical [29] [30] and heavy industries [31]. It has also been applied in thermal energy storage technology to investigate thermally induced stresses in packed-bed heat storage systems [32].

Besides the soft sphere methods, also hard sphere methods have been developed treating the particles as perfectly rigid bodies. Representatives of this class of models are the event-driven method (ED) [33] [34] which is primarily applicable to dilute and agitated "granular gases" (e.g. [35] [36]) and the (non-smooth) contact dynamics method (CD or NSCD) [37] [38] [39] which was developed for dense particle assemblies with multiple contact partners (e.g. [40] [41]).

Compared to DEM (MD), the CD method offers a much larger time step as the very small length and time scales of the (viscoelastic) particle interactions are not resolved. Instead, the contact forces between particles are determined such that no mutual interpenetration of the particles occurs and that the contact laws (i.e. frictional stick-slip constraints) are satisfied [42]. In a network of particles the set of contact forces which consistently satisfies all constraints usually has to be determined iteratively [43]. Hence, the computational effort per time step and particle is higher for CD than for DEM.

CD is advantageous for quasi-static systems of rigid particles, especially for limited particle numbers. For large systems with finite rigidity of the particles, DEM is favorable [43].

All discrete particle methods may also incorporate heat transport inside the granular matter. However, in this case the interstitial gas between the particles usually has to be taken into account even if the motion of the fluid-phase is not explicitly modelled. For densely packed systems heat transport is commonly modelled by a network of thermal resistances between particles. Different approaches have been proposed for these systems [44] [45] [46] [47].

2.1.2 Continuum models

A continuum model relies on the assumption of a continuous medium with locally averaged properties like density or velocity. The flow field and the density distribution of the continuum are obtained by solving the balance equations for mass and momentum. However, to close the system of equations, constitutive relations for the stresses in the

continuum are required which are provided by rheological models of the granular material.

Rheological models of granular flows fall into two groups depending on the flow regime that is investigated: Models for slow, dense granular flows and models for rapid, strongly agitated flows [17] [48].

In case of strongly agitated flows, such as fluidized beds, particles interact by binary collisions. Models for such rapidly moving granular flows have been developed by analogy with the kinetic theory of gases ("Kinetic theory of granular fluids" – KTGF) [17]. In contrast to molecules, though, collisions between particles are highly inelastic, resulting in a strongly dissipative nature of "granular gases".

The KTGF has been used to investigate various types of the granular flow such as vibrated systems and chutes [49] and fluidized beds [35] [50].

The kinetic theory is based on the assumption of binary collisions between particles. However, if the packing fraction, ε_s, increases ($\varepsilon_s > 0.4$), as is the case in moving packed beds, particles interact by enduring, frictional contacts with multiple neighbors and hence the kinetic theory is no more valid.

The behavior of such slow, dense granular flows is traditionally subject to soil mechanics and the so-called critical state theory [51] [52]. Central phenomena occurring in this type of flows is the transition from a solid-like to a yielding state as well as the dilation and the compaction of the material under shear deformation.

Such (elasto-)plastic deformations of a granular material are modelled based on plasticity theory ([48] [17]). These models, which are mostly based on metal plasticity ([53] in [54]), rely on the concept of a pressure-dependent yield function [54]. The yield function defines whether the material remains rigid or whether it flows under a given state of internal stresses. A simple yield function is the Drucker-Prager yield function [55] which is based on the Coulomb yield criterion according to which the shear stress at failure is proportional to the normal stress and a coefficient of internal friction. In three dimensions the Drucker-Prager yield surface (yield function) has the shape of cone (see Figure 3).

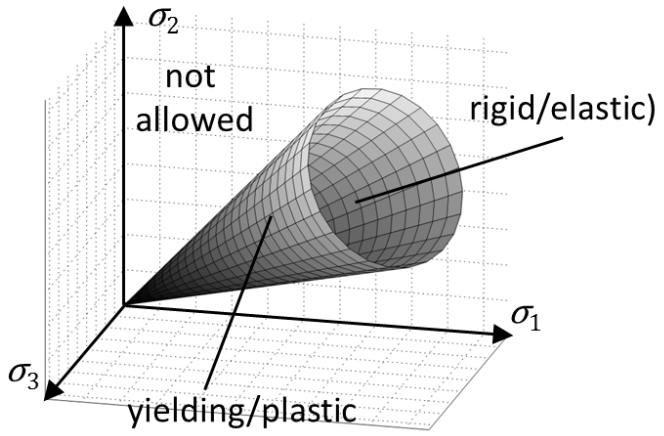

Figure 3. Drucker-Prager yield surface (without cohesion) in 3-D pricipal stress (σ_1, σ_2, σ_3) space. For stress states inside the cone, the material behaves rigid/elastic. For stress states on the surface of the cone, yielding occurs. Stress states outside the cone are not allowed.

Once yielding occurs, a flow rule defines how the plastic deformation takes place by relating the components of the stress tensor, $\boldsymbol{\sigma}$, to those of the rate of deformation tensor, $\boldsymbol{D}$. To this end an additional function, *G,* called the plastic potential is introduced. The gradient of the plastic potential gives the strain direction:

$$D_{ij} = \gamma \frac{\partial G}{\partial \sigma_{ij}}, \tag{1}$$

where γ is a scalar coefficient, often called the granular fluidity. A central feature of equation (1) is that the major principal axes of the two tensors are aligned ('coaxiality'), i.e. that stresses cause deformations preferentially in the same direction [56] [57]. In many studies the plastic potential function is chosen identical with the yield function which is called an 'associated flow rule'.

Several extension to this basic approach have been proposed, such as non-associated flow rules (e.g. [58]) or curved yield surfaces (e.g. [59]) to include effects like dilatancy and contractancy, hardening and improved energy dissipation. Furthermore, there are models to include also angular momentum (Cosserat models [60]) or models which do not involve a yield condition but assume that stress rate can be expressed as a function of the stress tensor, rate of deformation tensor and the solids fraction ("Hypoplastic models" [61] [62]). An overview of different model extensions can be found in [54].

In many cases of continuously flowing granular materials it has turned out that the elastic part of the deformation can be neglected [54] and that the material deforms at approximately constant volume ("critical state approximation") [58] [48] [63] which leads to a simplification of the constitutive relations.

Plasticity models have been used to calculate the granular flow in hoppers [59], bunkers and bins [64] [58], geophysics [57] [65], blast furnaces [66] and snow avalanches [67].

The bridging of both, the frictional flow regime described by plasticity models and the kinetic-collisional flow regime described by the KTGF is still a matter of research. The most common approach is to assume that the net stress in the granular medium is simply the sum of the frictional and the kinetic stresses, each determined as it acts alone [48] [68]. This approach however is only a preliminary step towards a comprehensive theory of the intermediate flow regime. Three other approaches have been proposed [69] [70] [71] which, according to Rao and Nott [48], have ingredients useful for further developments but so far are quite speculative and without a firm basis.

To include heat transport in a continuum model, the corresponding balance equation requires a formulation for the effective thermal conductivity of the bulk. If the motion of the fluid phase is considered, a heat transfer coefficient between the two phases is to be incorporated also. An overview of possible heat transfer correlations between particles and a fluid is given by Syamlal et al. [72].

Models for the effective thermal conductivity of the granular bulk usually assume a stagnant interstitial fluid [73] [3] [74] [75]. Still, they are also commonly used for moving packed beds (e.g. [76] [77]) and also in fluidized beds [78] [79].

2.2 Prior work on heat transfer and granular flow in moving packed beds

Heat transfer between granular media and immersed surfaces has been investigated for a long time. In the 1950s Mickley and Fairbanks [80] introduced the so-called "packet-theory" to account for the heat transfer in fluidized beds. They assumed a "packet" of particles to be in contact with the heat transferring surface for a short residence time t after which it is replaced by a fresh packet from the bulk. Based on the assumption of unsteady heat conduction into a homogeneous packet, they derived an expression of the instantaneous heat transfer coefficient, $\alpha_{t,S0}$, between the packet and the surface. Ac-

cording to their formulation, $\alpha_{t,S0}$ is proportional to the inverse square root of the residence time ($\alpha_{t,S0} \sim t^{-0.5}$).

However, succeeding researchers (e.g. [81]) observed that at very short residence times the heat transfer coefficient approaches a (finite) maximum which primarily depends on the particle size. To account for this result, Baskakov [82] introduced a contact resistance in series with the thermal resistance of the packets introduced by Mickley and Fairbanks. The physical origin of this contact resistance initially remained unclear.

Later, Schlünder [83] suggested that the thermal conductivity of the interstitial gas decreases around the contact point where the gap width s undercuts the mean free path l of the gas molecules ($Kn = l/\delta > 1$). Hence, the heat transfer coefficient remains finite even around the contact point where the gap width approaches zero.

The concept of the series connection of the two thermal resistances (contact resistance $R_c = 1/\alpha_c$ at the surface and penetration resistance $R_{S0} = 1/\alpha_{S0}$ of the packets) is illustrated in Figure 4.

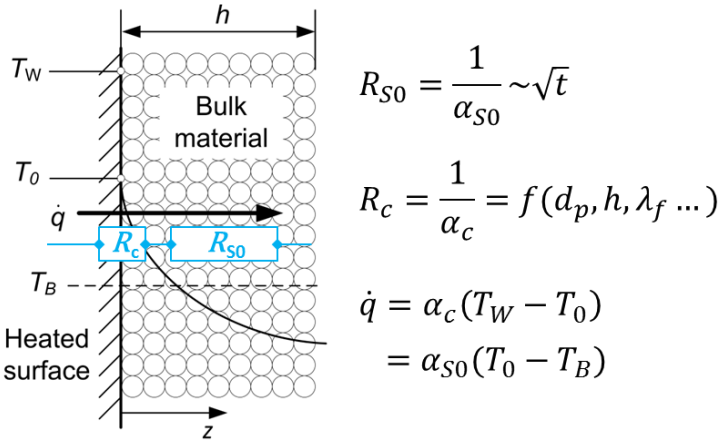

Figure 4. Heat transfer between a surface and a contacting granular bulk material. Concept of a series connection of two thermal resistances, R_c and R_{S0}.

Denloye and Botteril [84] investigated the heat transfer in flowing packed beds using different materials, grain sizes and interstitial gases. They found the heat transfer coefficient to increase with increasing thermal conductivity of the gas, decreasing grain size and decreasing residence time.

Other researchers published similar works (e.g. [85]) in various experimental set-ups and generally confirmed these findings. An overview is given in the works of Obuskovic [77] and Niegsch [86].

Of particular interest with respect to the application in solar thermal power plants are tubular heat exchanger designs. This is due to the fact that the pressure of the secondary fluid – usually water/steam – is very high in this case. The granular material may flow through the shell of the heat exchanger while the pressurized fluid flows inside the tubes.

A comparison between a vertical and a horizontal tube arrangement shows that the latter has the advantage that the heat transferring surface can be distributed over the entire width of the heat exchanger – especially in a staggered tube arrangement. Hence, a greater share of the particles comes in contact with the surface. This is of major importance as the thermal conductivity typically is very low in moving beds. In addition, the flow is laminar and almost no mixing lateral to the main flow direction occurs [86]. The granular flow pattern in a horizontal arrangement is more complex but leaves more potential for optimization as will be shown in the following paragraphs.

Several works addressed the heat transfer between horizontally arranged tubes and a moving packed bed [76] [87] [88] [89] [86] [2] [1] of which three are to be emphasized here. These three studies also investigated the granular flow field around the tubes.

Niegsch [86] [2] was the first who studied the heat transfer rate between a moving bed and a bundle of horizontally arranged tubes. He investigated different staggered and aligned tube arrangements and several materials like glass beads, corundum particles, ash and quartz sand. The heat transfer rate in the bundles increased with the mass flow rate but approached an upper limit at high flow rates.

Besides the overall heat transfer of the tube bank, Niegsch also measured the local heat transfer coefficient along the circumference of a single tube of the bundle. He observed small heat transfer rates at the top and below the tube and high heat transfer rates at the lateral sides. He associated the measured profile with the granular flow pattern around the tubes.

To visualize the granular flow, he used layers of colored quartz sand in a transparent acrylic glass tank and observed a stagnant area on top of the tubes, high flow speeds at the side and a cavity below the tubes. Therefore, he concluded that the stagnant zone

and the cavity constitute additional thermal resistances which hamper the heat transfer in the corresponding areas.

Niegsch developed an empirical model to describe the bulk solids movement and the heat transfer at the tube surface. However, his model was based on certain assumption regarding the size, shape and extent of the stagnant zone and the void zone which have not been verified. For example he assumed that the stagnant area is solely dependent on the friction parameters of the bulk and the tube surface.

Takeuchi [89] performed similar experiments with a bank of one to three tube rows in a moving bed of polypropylene particles. He measured the local heat transfer coefficient at a single tube and found a profile similar to the one of Niegsch. Furthermore, he varied the relative position of the tubes and showed that a staggered arrangement yields by far higher heat transfer rates than an aligned arrangement.

To measure the granular flow field he tracked a horizontal layer of tracer particles using X-ray video technique. He noticed that the stagnant zone at the tube vertex remained independent of the mass flow rate but changed with the tube arrangement. Especially at the first row of tubes and in case of large horizontal pitches he reported that the stagnant zone disappeared. In these cases significantly more heat was transfer at the top of the tube.

Baumann [1] performed heat transfer measurements at elevated temperatures (> 500 °C) for the specific application of MBHE in CSP plants using quartz sand and sintered bauxite proppants. He examined two staggered tube arrangements with different horizontal spacing. The narrower arrangement showed distinctly higher heat transfer rates which was attributed to smaller residence times due to elevated flow speed in the constricted flow cross-section between the tubes. However, similar to the findings of Niegsch the heat transfer rate approached an upper limit with increasing mass flow rate.

Baumann used particle image velocimetry (PIV) to analyze the granular flow in a transparent acrylic glass heat exchanger mockup. From the results he estimated the size of the stagnant zone, which primarily depended on the tube arrangement while the flow speed and the type of granular material showed little effect.

Furthermore, Baumann measured the granular flow speed along the tube surface. Depending on the tube arrangement he observed a significant acceleration of the granular flow in the lower half of the tube. He inferred that the stagnant zones on top of the tubes grew into the space between the upstream tubes and thus reduced the effective flow

cross section. Due to the reduced cross section, he argued, the flow speed in the lower part of the tubes increased.

He found the void area below the tubes to remain independent of the tube arrangement and the mass flow rate. The inclination of the flanks of the void area was of the order of the repose angle of the material.

Baumann proposed a 2D CFD[1]-model to calculate the flow field around the tubes which also included heat transport inside the bulk. However, his model didn't capture the formation of the stagnant areas at the tube vertex. Furthermore, at elevated mass flow rates (flow speeds) the model tended to considerably overestimate the heat transfer rate. Nevertheless, Baumann considers the continuum model a promising approach which should be followed up in future works.

The three works summarized in the preceding paragraphs primarily focused on the experimental investigation of moving bed heat exchangers. They revealed the overall flow pattern around the tubes and the general heat transfer characteristics. However, besides the well-known dependence of the heat transfer on the residence time, no systematic studies exist on how the thermal performance of the device can be optimized. For example, it is not known whether the size and extent of the stagnant areas, which are hampering the heat transfer at the top of the tubes, can be influenced by certain measures.

Especially, no comprehensive model of the granular flow around the tubes exists. The model of Niegsch relies on simplifying assumptions regarding the flow pattern which is also the case for the model of Lee et al. [90]. In the model of Baumann less 'a priori' information about the flow pattern is included but the stagnant area is not captured and the results regarding the heat transfer rate obviously are erroneous, especially at high mass flow rates. So, obviously there is still a need for further work regarding the modelling and the understanding of moving bed heat exchangers.

2.3 Scope of investigation

As shown in the previous section, a reliable and comprehensive tool for the design and optimization of moving bed heat exchangers with staggered, horizontal tubes is still missing. This work contributes to filling this gap by the accurate modelling of the hy-

[1] CFD = Computational Fluid Dynamics

dro- and thermodynamic processes in the device. To this end, a two-step proceeding is chosen:

Firstly, a comprehensive continuum model is developed which captures both the granular flow field around the tubes as well as the heat transport inside the granular material. In particular, it captures the influence of granular-specific flow phenomena like stagnant and void zones. As it is expected that effects occurring on particle scale will also be relevant for the heat transfer process, the continuum model is to be supplemented by a discrete particle model providing insight into these phenomena. The results of the discrete particle model are used to modify the continuum model and to increase its precision.

The simulation results of the different models are validated by means of appropriate experiments. This includes the measurement of the flow pattern of the moving bed around the tubes. In addition, the heat transfer at a single heat exchanger tube is to be assessed in detail.

Secondly, a simplified model of the heat transfer between the tubes of an MBHE and the moving bulk is to be developed. This model is based on the findings of both the discrete particle and the continuum model and provides a computationally efficient way to assess different heat exchanger designs. Furthermore, such a simplified model can be used in system simulations of industrial or power plant processes using a moving bed heat exchanger.

The validated models are used to assess the influence of different operating, design and material parameters on the granular flow pattern with respect to the thermal performance of the heat exchanger.

The work is structured as follows:

In chapter 3 the experimental infrastructure and measurement setup used for the validation of the numerical models is introduced. In chapter 4 the continuum model and the discrete particle model are introduced as well as the considered boundary conditions and calibration procedures of the two models. In chapter 5 the validation of the two models is addressed. In a first step the flow pattern is validated which leads to a modification of the continuum model to account for particle-scale effects. The modified continuum model is subsequently validated based on the measurement of the heat transfer at a single tube.

Chapter 6 focuses on a simplified model for the heat transfer between a single tube and the bulk. To this end, the dependence of the flow pattern on several influencing parameters is assessed using the discrete particle model. The results of these parameter studies are subsequently used to develop the simplified model.

The results of the work are summarized in chapter 7.

3 Experimental setup

The moving bed heat exchanger test infrastructure used for this study is shown in Figure 5 (left) and has been described in detail in [91]. It basically consists of a storage container for the granular material, a particle heat exchanger and a conveyor device. From the storage tank the material flows, driven by gravity, through the test section where arbitrary heat exchanger geometries can be inserted. The chain conveyor returns the material back from the heat exchanger outlet into the storage container.

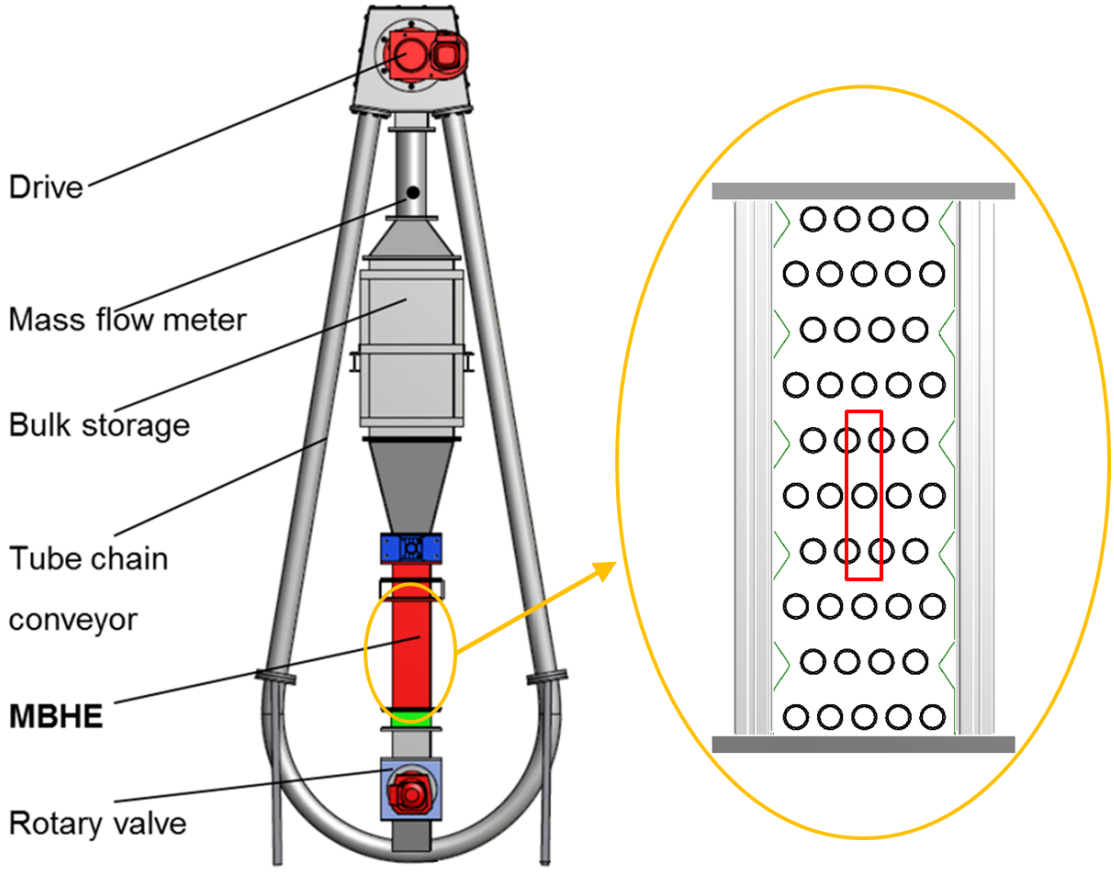

Figure 5. Left: Moving bed heat exchanger test rig. Right: Heat exchanger mockup. The rectangularly framed area marks a representative section of the tube arrangement, which is investigated numerically in later chapters.

The heat exchanger test rig was filled with quartz sand of an average grain size of d_p = 0.6 mm and d_p = 1.2 mm, respectively, depending on the experiment to be conducted. The average flow speed in the free cross-section of the heat exchanger was evaluat-

ed from the mass flow rate of the tube chain conveyor and the bulk density ($\rho_b \approx 1600$ kg/m³). The mass flow rate depended linearly on the rotational speed of the chain conveyor and was calibrated beforehand. The flow speed was varied in the range of $u_{ref} = 1.5…6.0$ mm/s. The measurement uncertainty of the reference velocity is approximately 5 % (see appendix A.3).

To allow a visual inspection of the bulk flow, the heat exchanger was replaced by an acrylic glass mockup which is shown in Figure 5 (right). When operated, the bulk material entered at the top and flowed around the tubes.

Two types of experiments were conducted: On the one hand the granular flow field inside the heat exchanger mock-up was examined using PIV analysis; on the other hand, the local heat transfer rate from a single tube to the bulk was examined.

3.1 Measurement of flow field

Regarding the experimental examination of granular flows, different measurement techniques exist [17]. Though restricted to the inspection of the visible surface of the bulk flow, particle image velocimetry (PIV) and particle tracking (PT) are commonly used. They are easy to handle and are applicable to relatively large objects and measurement setups.

In this work, PIV is used to examine the granular flow inside the mockup. PIV is based on the analysis of successive images of the flow. The images are subdivided by a grid of stationary control volumes. By detecting recurring patterns and determining their displacement in a pair of images the local velocity of the flow can be calculated. Unlike for fluids, in granular flows no extra tracer particles are needed as the patterns are formed by the grains themselves. A more detailed description of PIV in the context of granular flows can be found elsewhere [1] [92].

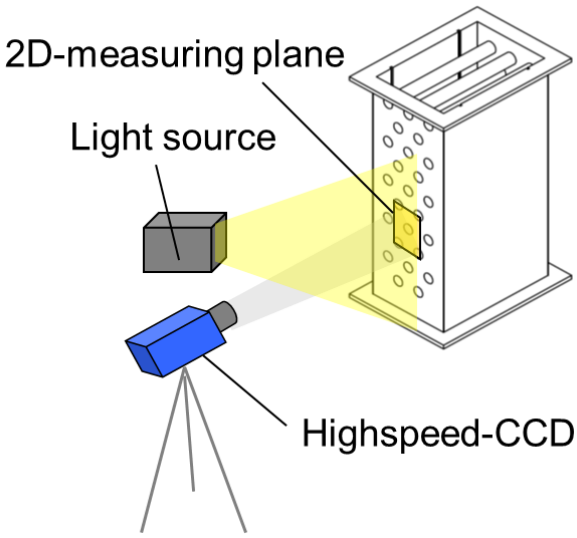

Figure 6. Schematic of the experimental setup for PIV analysis.

Figure 6 shows a schematic of the experimental setup. Pictures were taken at a rate of 25 Hz through the transparent acrylic glass front of the mockup. To reduce temporal fluctuations of the local flow speed the results were averaged over a sequence of 40 pairs of images.

The grid discretization was determined based on the expectant flow speed. The displacement between two images should be about a quarter of the size of the control volumes [93]. As the flow is moving into vertical direction the flow speed in y-direction is generally higher than in x-direction. At a frequency of 25 Hz and an expectant flow speed of $u \approx 10$ mm/s between the tubes, this leads to a vertical discretization of $\Delta y = 1.6$ mm. As the flow speed in x-direction is much smaller, a finer discretization of $\Delta x = 0.4$ mm is used. This means that a control volume contains only two or three particles which is far below the recommended amount of 10…25 particles [93] for conventional PIV measurements. However, in the case at hand the images are rich in contrast and the PIV-algorithm doesn't necessarily track the particles but rather an optical structure in the image which might also be of sub-particle size.

An exemplary vector plot obtained from the PIV analysis is shown in Figure 7.

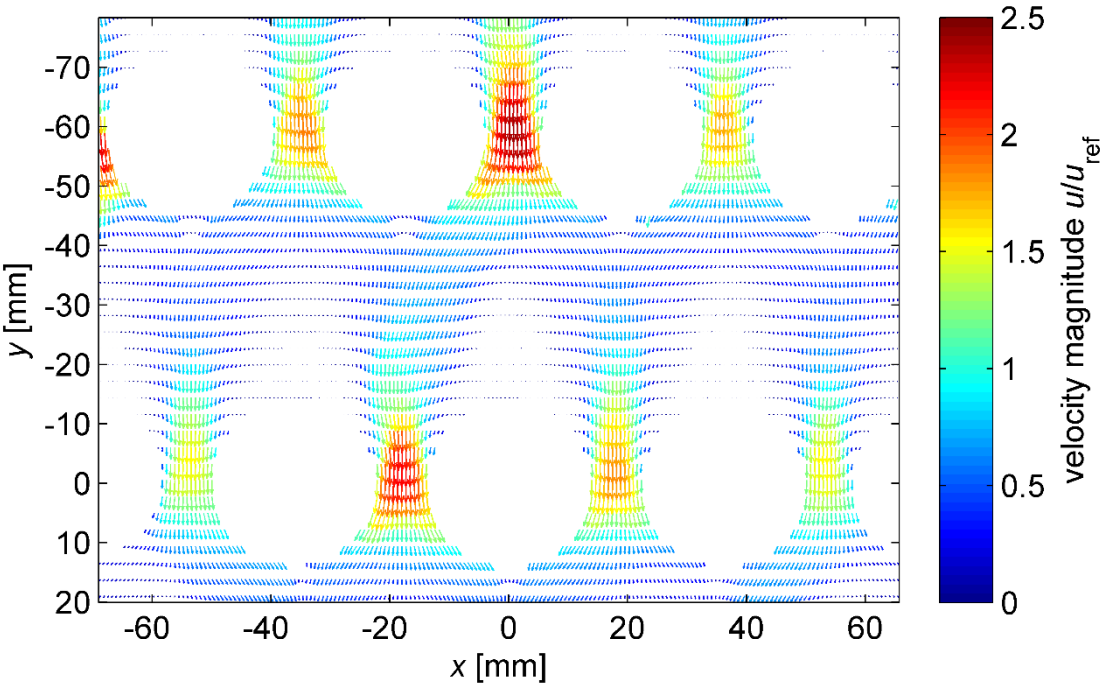

Figure 7. Exemplary vector plot obtained from PIV analysis.

In Figure 8 the velocity profile along the horizontal plane $y = 0$ (see Figure 7) is depicted. Four peaks of the flow speed are found in Figure 8, which belong to the four gaps between the tubes. Due to continuity the mean flow speed, $\bar{u}$, between the tubes (over the entire cross section of the mockup) must be

$$\frac{\bar{u}(y=0)}{u_{\mathrm{ref}}} = \frac{s_{\mathrm{H}}}{s_{\mathrm{H}} - D_{\mathrm{T}}} = 3.7, \tag{2}$$

with s_{H} being the horizontal spacing of the tubes and D_{T} being the outer tube diameter. As visible from Figure 8, the mean flow speed between the tubes in the measurement is $u/u_{\mathrm{ref}} \approx 1.7$, which is attributed to the fact that the flow is slowed down due to surface friction of the acrylic glass front wall. Thus, for comparison of the measurement and simulation results (see section 5.1) the surface friction of the front wall must be taken into consideration in the numerical model. The flow inside the mockup cannot be measured directly.

The flow speed between the tubes deviates by up to 21 % from the average value of $u/u_{\mathrm{ref}} \approx 1.7$. Possible origins for the uneven velocity distribution are disturbing influences of the front wall, the preceding row of tubes, the change of the free cross-section between two subsequent tube rows due to the guiding plates at the lateral sides of the

mockup (see Figure 5 (right)) and the tube chain conveyor (for further discussion of these influences see Appendix A.3).

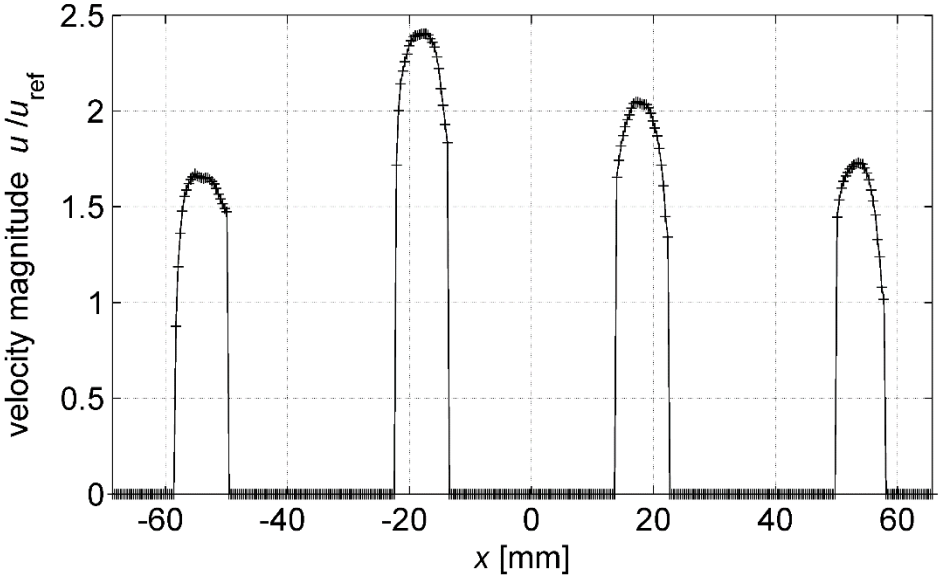

Figure 8. Horizontal velocity profile (velocity magnitude) at $y = 0$ (see Figure 7).

Inaccuracies of the PIV measurement results are mainly caused by two sources of errors: Firstly, by the calibration procedure to find the conversion factor from image to physical space. Here, a conversion factor of 16.6 px/mm was determined based on a known length of 76 mm (1262 px). Assuming that the measurement accuracy is 10 px, the resulting error is approx. 0.8 %.

Secondly, the PIV evaluation algorithm causes an inherent evaluation error of about 0.2 px [93]. Averaging over a series of 39 pairs of images reduces the inaccuracy to 0.03 px. At a frequency of 25 Hz this corresponds to an uncertainty of the calculated flow speed of ± 0.05 mm/s. This uncertainty is especially relevant in areas where the flow speed is low such as in the stagnant area. Based on the velocity in the free cross section of the mockup ($u_{ref} = 4.0$ mm/s) during the experiment, the resulting uncertainty is 1.25 %.

These two sources of measurement errors thus lead to an overall accuracy of approx. 2 % of the PIV measurement results.

3.2 Measurement of local heat transfer coefficient

The local heat transfer coefficient between a single tube and the granular flow was evaluated, following the approach of Takeuchi et al. [89]. It is based on measuring the local surface temperature of a heated test tube under operation. The local heat transfer coefficient is calculated from the heat transfer rate and the local temperature difference, as shown below.

The test tube, made of polyethylene (PE), substituted one of the stainless steel tubes at a central position in the heat exchanger mockup. The PE-tube was covered by a stainless steel foil which was electrically contacted at both sides of the tube. By applying an electric current, the foil was heated up due to its ohmic resistance. The surface temperature T_W of the foil was measured by three thermocouples. The thermocouples were located under the foil in three notches carved into the PE tube with the notches being evenly distributed around the tube circumference (120°-displacement between the thermocouples). A drawing of the test tube is displayed in Figure 9.

The heat generation rate $\dot{q}$ is calculated according to equation (3), assuming a homogeneous current density. Further below it is shown that this assumption is justified.

$$\dot{q} = \frac{P_{\mathrm{el}}}{A} = \frac{I^2 R}{A} \tag{3}$$

In equation (3), A is the area of the foil, I is the current and R is the ohmic resistance of the foil. Assuming adiabatic conditions at the inner surface of the tube (stagnant air), the total of the thermal energy of the foil is transferred to the surrounding granular medium after reaching a stationary state. With respect to the reference temperature T_{ref} the local heat transfer coefficient $\alpha_{\mathrm{loc}}(\omega)$ – at the position angle ω of the thermocouples – was calculated:

$$\alpha_{\mathrm{loc}}(\omega) = \frac{\dot{q}}{T_{\mathrm{W}}(\omega) - T_{\mathrm{ref}}} \tag{4}$$

The reference temperature T_{ref} was defined as the inflow temperature of the heat exchanger mock up which was measured in the center of the heat exchanger inlet. By rotating the test tube around its axis, a 360°-profile of the local heat transfer coefficient around the tube was derived.

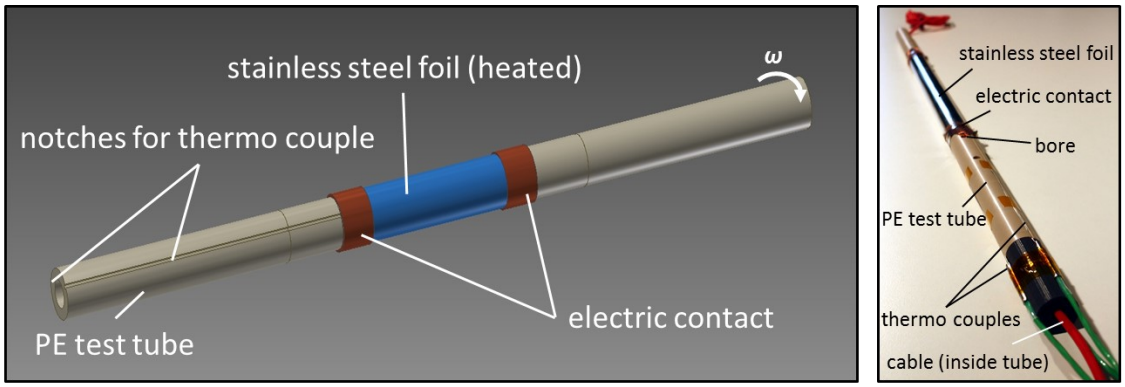

Figure 9. Sketch (left) and photo (right) of the test tube for the measurement of the local heat transfer between tube surface and granular flow.

To evaluate the local heat transfer rate $\dot{q}$ according to equation (3) it was vital that the current density was distributed evenly around the circumference of the tube at the location where the surface temperature of the foil was measured. This prerequisite was tested beforehand: The tube was heated in the environment of stagnating air and the distribution of the surface temperature was measured using an infrared camera. The temperature varied by $\Delta T \approx 0.5$ K around the circumference of the tube which corresponds to an uncertainty of the current density of less than 2.5 %. Together with the measurement uncertainty of the quantities R, I and A in equation (3) the total uncertainty of the heat flux density $\dot{q}$ is approximately 4.5 % (see appendix A.2).

The test tube was inserted into the heat exchanger mockup at a central position. At the beginning of every measurement series the flow rate was adjusted to the desired value and the foil was heated for 30 minutes to reach a stationary state. During the measurement the tube was rotated clockwise in steps of $\Delta\omega = 10°$ beginning at the top of the tube ($\omega = 0°$) and waiting about five minutes at every step before taking the local surface temperature. The local surface temperature appeared relatively constant during the measurement ($\pm$ 0.1 K) except at $\omega \approx 150°$ and $\omega \approx 210°$ where fluctuations are observed of about $\pm$ 1 K were observed. These fluctuations are attributed to the formation of a void area below the tube which will be discussed in more detail in chapter 5.

Figure 10 (left) shows exemplary profiles of the reference temperature T_{ref} at the inlet of the mockup and of the surface temperature T_{W} at the tube wall (of the stainless steel foil). The reference temperature didn´t stay at a constant level but slightly increased during the experiment. The angle-ranges “TC1” to “TC3” denote the ranges recorded by the three different thermocouples.

Figure 10 (right) shows the corresponding profile of the local heat transfer coefficient. The profile is approximately symmetric with maxima at the lateral sides of the tube ($\omega \approx 90°$, $\omega \approx 270°$), a minimum below the tube ($\omega = 180°$) and intermediate values at the top of the tube ($\omega \approx 0°$, $\omega \approx 360°$). The results are discussed in detail in section 5.2.3 where they are compared them to corresponding simulation results.

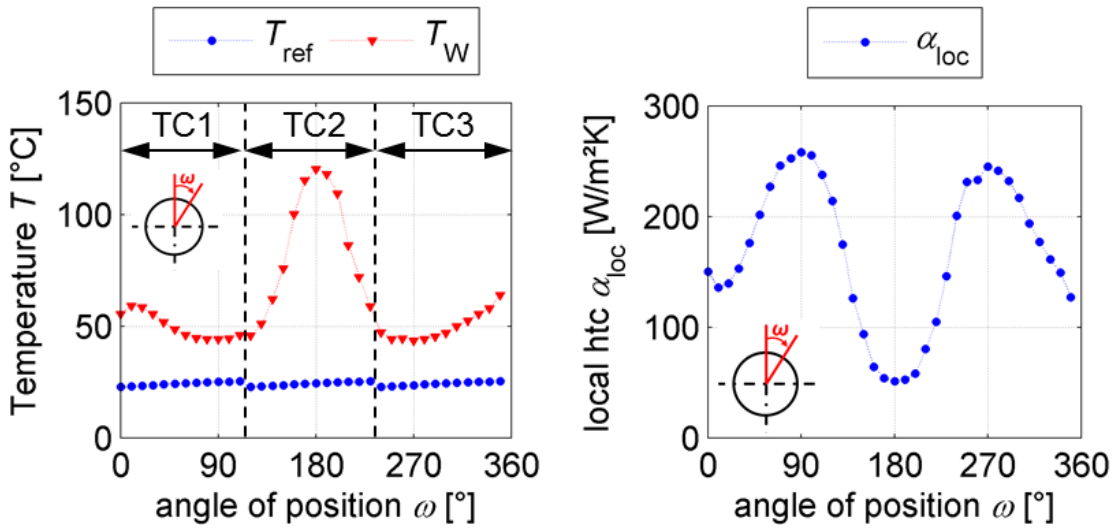

Figure 10. Exemplary measured temperature profiles (left). Corresponding profile of local heat transfer coefficient (right).

The accuracy of the measurement results according to equation (4) depends on the one hand on the accuracy of the heat flux $\dot{q}$ discussed above, on the other hand on the accuracy of the temperature difference ($\Delta T = T_W(\omega) - T_{ref}$) which is approximately 0.2 K. At the lateral sides of the tube with $(\Delta T)_{min} \approx 19$ K this corresponds to a relative uncertainty of approximately 2 % (see also appendix A.2).

Hence, the total uncertainty of the measured local heat transfer coefficient α_{loc} is estimated to approximately 7 %.

Three different tube arrangements and two different particle diameters were investigated. The examined configurations are given in Table 1. For each configuration four different mass flow rates/reference flow speeds were tested. The measurement results of the four different configurations are presented in section 5.2.3 together with the corresponding simulation results of the continuum model.

Table 1. Investigated configurations.

Tube arrangement	Horizontal tube spacing s_H	Vertical tube spacing s_V	Mean particle diameter d_p	Reference flow speed u_{ref}
	mm	mm	mm	mm/s
TA1	57	40	0.6	1.5 / 3.0 / 4.5 / 6.0
TA2	57	60	0.6	1.5 / 3.0 / 4.5 / 6.0
TA3	37	60	0.6	1.5 / 3.0 / 4.5 / 6.0
TA3	37	60	1.2	1.5 / 3.0 / 4.5 / 6.0

4 Modelling

In this work two different modelling approaches are used – a continuum model (CFD) and a discrete particle model (DEM) – to calculate the granular flow around the horizontally arranged tubes in a moving bed heat exchanger. The investigated geometry is depicted in Figure 11. It consists of a representative section of three rows of tubes arranged in a staggered manner (see framed area in Figure 5 (right), p.16). The granular material enters the geometry at the top, flows around the tubes and leaves at the bottom.

The continuum model simulations are in 2D, transient. The motion of the interstitial fluid (air) and the heat transport inside the bulk are included. The model equations are given in the following section. The geometry is split along the vertical center line (see Figure 11, left), and only one half is simulated using symmetry boundary conditions in *x*-direction.

The boundary conditions for the continuum model are as follows: At the inlet the pressure of the fluid phase is set, the volume fraction for both phases and the inlet temperature (same for both phases). The boundary conditions at the tube walls deserve further explanation and are discussed in detail in section 4.1.2. At the outlet the gradient of the volume fraction normal to the boundary and the temperature for both phases is set. Furthermore, a fixed outlet velocity is defined which is the same for both phases.

The mesh of the continuum model was refined until the simulation results converged. At the tube surface a local refinement was introduced to resolve the temperature gradient at the wall. This lead to a mesh size of about one particle diameter (0.6 mm) at the tube surface while in the rest of the geometry the mesh size was about three particle diameters in each spatial direction. The model equations of the continuum model follow in section 4.1.

In the discrete particle simulation are in 3D as quantities like the porosity and the coordination number[2] of the moving bed are three-dimensional phenomena. In z-direction the geometry is 13 to 20 particle diameters thick (depending on the studied case) and is confined by walls. The rear wall is friction-less in all cases. The friction coefficient at the front wall is non-zero for the comparison with the validation experiment in sec-

[2] The coordination number is the number of contacts of a particle with its neighbors. It is of major importance for the heat transport in a packed bed [44] [74].

tion 5.1. For all remaining simulations it is set to zero. Further explanation is given in section 4.3.2.

In *x*-direction periodic boundaries are used in the discrete particle model. At the tube walls a wall friction coefficient is assigned which will be discussed in section 4.3. Heat transport as well as the interstitial fluid is not considered in the discrete particle model.

After the simulation geometry was filled randomly with particles a fixed outlet velocity was specified by means of a moving horizontal plate. The model equations for the discrete particle model follow in section 4.2.

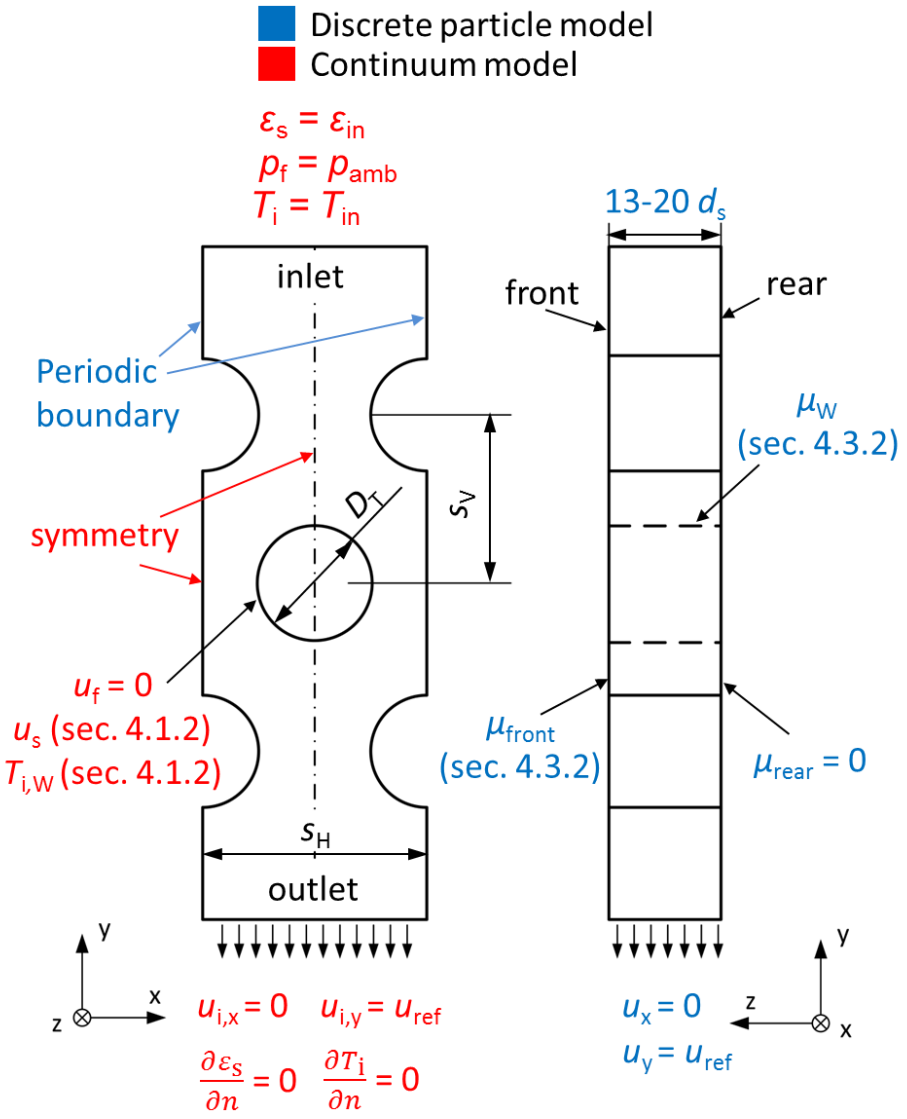

Figure 11. Simulation geometry with boundary conditions. Side view only for DEM model (3D). Subscripts: “s” = solid phase, “f” = fluid phase, “i” is substitute for both phases in the continuum model. Remaining subscripts and symbols are explained in the following sections.

The following Figure 12 shows exemplary simulation results (velocity magnitude of the particles/granular phase) of both models.

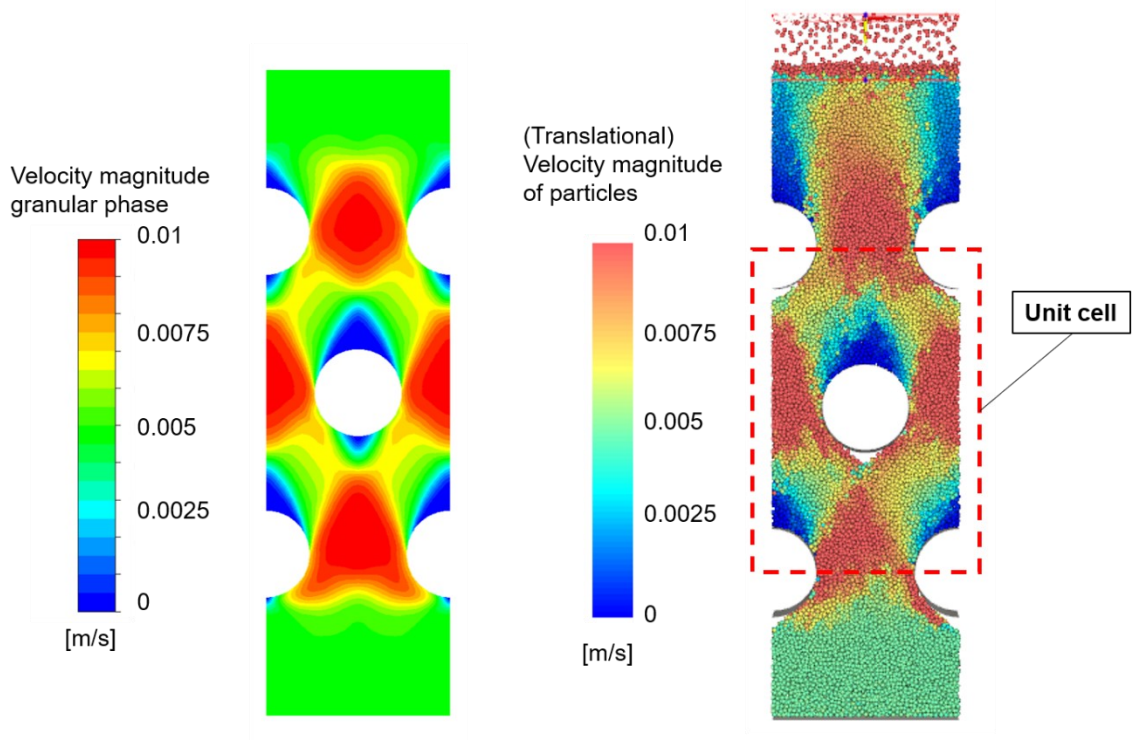

Figure 12. Exemplary simulation results of both models. Left: Velocity magnitude of granular phase (Continuum model). Right: Magnitude of translational velocity of particles (Discrete particle model).

In chapter 5 the two models are compared to each other and to experimental flow measurement results. The comparison is performed based on the unit cell in the center of the geometry (see Figure 12, right). The areas above and below the unit cell, which are dominated by boundary effects, are not considered in the comparison.

At this point, some differences regarding the boundary conditions between the two models and the experiment have to be mentioned. In the DEM model the particles are generated above the geometry (with a low packing fraction) and fall into the geometry. In contrast to that, in the continuum model the inlet packing fraction is high while the flow speed is low. This leads to deviations regarding the simulation results outside the unit cell.

However, simulations with more tube rows arranged in vertical direction show a recurring, constant flow pattern for multiple unit cells. Therefore, in this work the geometry in Figure 12 with only one representative unit cell is used to analyze the flow pattern.

Furthermore, the fact that the flow pattern recurs constantly after the first row of tubes justifies the comparison of the simulation results to experimental data from a unit cell in the center of the heat exchanger geometry (see Figure 5).

4.1 Continuum model equations

The continuum model mainly follows the works of Srivastava et al. [63] and Schneiderbauer et al. [94]. The moving bed is modelled as two interpenetrating continua (Euler-Euler approach), one representing the granular phase and the other one representing the gas phase. Following the approach of Ishii [95], for both phases averaged balance equations are solved as shown in equation (5)-(7).

$$\frac{\partial}{\partial t}\varepsilon_\mathrm{i}\rho_\mathrm{i} + \boldsymbol{\nabla}\cdot(\varepsilon_\mathrm{i}\rho_\mathrm{i}\boldsymbol{u}_\mathrm{i}) = 0 \tag{5}$$

$$\frac{\partial}{\partial t}(\varepsilon_\mathrm{f}\rho_\mathrm{f}\boldsymbol{u}_\mathrm{f}) + \boldsymbol{\nabla}\cdot(\varepsilon_\mathrm{f}\rho_\mathrm{f}\boldsymbol{u}_\mathrm{f}\boldsymbol{u}_\mathrm{f}) = -\varepsilon_\mathrm{f}\boldsymbol{\nabla}p + \boldsymbol{\nabla}\cdot\varepsilon_\mathrm{f}\boldsymbol{\tau}_\mathrm{f} - \beta(\boldsymbol{u}_\mathrm{f} - \boldsymbol{u}_\mathrm{s}) + \varepsilon_\mathrm{f}\rho_\mathrm{f}\boldsymbol{g} \tag{6}$$

$$\frac{\partial}{\partial t}(\varepsilon_\mathrm{s}\rho_\mathrm{s}\boldsymbol{u}_\mathrm{s}) + \boldsymbol{\nabla}\cdot(\varepsilon_\mathrm{s}\rho_\mathrm{s}\boldsymbol{u}_\mathrm{s}\boldsymbol{u}_\mathrm{s}) = -\varepsilon_\mathrm{s}\boldsymbol{\nabla}p - \boldsymbol{\nabla}\cdot\boldsymbol{\sigma}_\mathrm{s} + \beta(\boldsymbol{u}_\mathrm{f} - \boldsymbol{u}_\mathrm{s}) + \varepsilon_\mathrm{s}\rho_\mathrm{s}\boldsymbol{g} \tag{7}$$

$$\frac{\partial}{\partial t}(\varepsilon_\mathrm{i}\rho_\mathrm{i}h_\mathrm{i}) + \boldsymbol{\nabla}\cdot(\varepsilon_\mathrm{i}\rho_\mathrm{i}\boldsymbol{u}_\mathrm{i}h_\mathrm{i}) = -\varepsilon_\mathrm{i}\frac{\partial p}{\partial t} - \boldsymbol{\tau}_\mathrm{i}\colon\nabla\boldsymbol{u}_\mathrm{i} + \nabla\cdot\varepsilon_\mathrm{i}\lambda_\mathrm{i}\nabla T_\mathrm{i} \pm Q_\mathrm{ij} \tag{8}$$

Here, the indices “s” and “f” denote the solid phase and the fluid phase, respectively, and “i” and “j” are substitutes for both phases. ε is the volume fraction, $\boldsymbol{u}$ the velocity, ρ the density and h the enthalpy of the corresponding phase. For the interphase drag coefficient β a correlation of Gidaspow et al. [50] is used which applies the Ergun equation for high volume fractions:

$$\beta = \begin{cases} 150\dfrac{\varepsilon_\mathrm{s}^2\mu_\mathrm{f}}{(1-\varepsilon_\mathrm{s})d_\mathrm{p}^2} + 1{,}75\dfrac{\varepsilon_\mathrm{s}\rho_\mathrm{f}|\boldsymbol{u}_\mathrm{f} - \boldsymbol{u}_\mathrm{s}|}{d_\mathrm{p}} & \text{if } \varepsilon_\mathrm{s} > 0.2 \\ 0{,}75C_\mathrm{D}\dfrac{\varepsilon_\mathrm{s}(1-\varepsilon_\mathrm{s})\rho_\mathrm{f}|\boldsymbol{u}_\mathrm{f} - \boldsymbol{u}_\mathrm{s}|}{d_\mathrm{p}}(1-\varepsilon_\mathrm{s})^{-2.65} & \text{if } \varepsilon_\mathrm{s} \leq 0.2 \end{cases} \tag{9}$$

$$C_{\mathrm{D}} = \begin{cases} \dfrac{24}{Re_{\mathrm{f}}}\left(1 + 0.15Re_{\mathrm{f}}^{0.687}\right) & \text{if } (1-\varepsilon_{\mathrm{s}})Re_{\mathrm{f}} < 1000 \\ 0.44 & \text{if } (1-\varepsilon_{\mathrm{s}})Re_{\mathrm{f}} \geq 1000 \end{cases} \tag{10}$$

For the gas phase shear stress $\boldsymbol{\tau}_{\mathrm{g}}$ a Newtonian closure is used:

$$\boldsymbol{\tau}_{\mathrm{f}} = 2\mu_{\mathrm{f}}\boldsymbol{D}_{\mathrm{f}}\,, \tag{11}$$

where $\boldsymbol{D} = 1/2\,(\boldsymbol{\nabla u} + (\boldsymbol{\nabla u})^{\mathrm{T}})$ is the rate-of-deformation tensor.

In the energy conservation equation equation (8) two quantities remain to be defined: The thermal conductivity λ_{i} of each phase and the interphase heat-exchange term Q_{ij}.

The heat exchange term depends on the temperature difference between the two phases and the interfacial area A_{fs}:

$$Q_{\mathrm{ij}} = \alpha_{\mathrm{fs}} A_{\mathrm{fs}} (T_{\mathrm{i}} - T_{\mathrm{j}}) \tag{12}$$

The interphase heat transfer coefficient α_{ij} is calculated using a correlation proposed by Gunn [96] which is valid for a wide range of packing fractions and Reynolds numbers (see appendix B.4).

The thermal conductivities of the two phases, λ_{s} and λ_{f}, are effective transport properties and are not to be confused with the microscopic properties of the pure substances. They are defined based on the effective thermal conductivity λ_{S0} of the bed which is calculated according to a correlation of Zehner and Schlünder [3]. Subsequently, λ_{S0} is split up into the two phase conductivities following the approach of Kuipers et al. [78] (see appendix B.3).

It is important to note that this approach assumes an isotropic thermal conductivity. In the direct vicinity of a wall, however, the packing structure becomes anisotropic, and due to the increased voidage in the near wall region the thermal conductivity decreases. In particular, the gas gap between the wall and the first layer of particles constitutes a significant thermal resistance. This thermal contact resistance is incorporated into the thermal boundary condition at the wall as will be described in section 4.1.2.1.

4.1.1 Frictional stress model

What remains to be defined is the stress tensor of the solid phase $\boldsymbol{\sigma}_s$ in equation (7). As shown in section 2.1.2, the constitutive relations for granular flow models depend on the investigated flow regime. As the packing fraction in a moving bed is close to the maximum packing fraction a plasticity model is applied to account for the frictional interaction between particles. It is assumed that the granular flow is completely governed by friction so that kinetic and collisional influences can be neglected. The applied frictional closure follows the works of Jackson [97] and Tardos et al. [56] and has been used to model the discharging process of granular material from bins [63] [94] and hoppers [56]. The frictional stress is written in a compressible Newtonian form:

$$\boldsymbol{\sigma}_s = \boldsymbol{\sigma}_{fr} = p_{fr}\boldsymbol{I} + \boldsymbol{\tau}_{fr} = p_{fr}\boldsymbol{I} + 2\mu_{fr}\boldsymbol{S}_s \tag{13}$$

Here, $\boldsymbol{S}_s = \boldsymbol{D}_s - tr(\boldsymbol{D}_s)$ is the deviator of the strain rate tensor. The two parameters p_{fr} and μ_{fr} are called frictional pressure and frictional viscosity, respectively, and are explained in more detail in the following paragraphs.

The frictional pressure accounts for the repulsive forces between grains and prevents the particle assembly from being compressed beyond a maximum packing fraction ε_{max}. In soil mechanics p_{fr} is often combined with a yield function to describe the effect that a particle assembly may dilate or compact under shear movement. The theoretical framework in this context is called the critical state theory. A simplifying assumption of this theory is that the dilation and compaction effects are small and that the state of the material is close to the so-called critical state where it deforms without any volume change ("Critical state approximation" [48]). This assumption has been proven to be justified for the flow in discharging bins [63] and hoppers [56].

Compared to this, the flow around a horizontal tube as it is being investigated in this work is more complex. Therefore, the critical-state-assumption has been tested beforehand and it was found that the influence on the simulation results is small. For example, the heat transfer rate changes by less than two percent. Hence, the cirtical-state-assumption is considered to be justified in the case at hand. The extended model (without critical-state approximation) is given in the appendix B.5. As a consequence p_{fr} is a function only of the packing fraction ε_s. Several formulations for the critical state pressure have been proposed [98]. In this work the form of Johnson and Jackson [99] is used:

$$p_{fr} = 0.1\varepsilon_s \frac{(\varepsilon_s - \varepsilon_{min})^r}{(\varepsilon_{max} - \varepsilon_s)^s} \tag{14}$$

The parameter ε_{min} is the minimum packing fraction above which frictional interaction between particles occurs ("loosest random packing"). If the packing fraction ε_s undercuts the minimum packing fraction ε_{min}, the frictional pressure p_{fr} is set to zero. The quantities in equation (14) are set the same as in the work of Srivastava et al. [63] and are listed in Table 2.

The second parameter in equation (13), the frictional viscosity μ_{fr}, accounts for the shear stresses inside the granular material. One of the major challenges regarding the viscosity is that it should model the transition of a granular material from a "solid" (static) to a "flowing" state. This behavior manifests in granular flows by the formation of static areas where the particle aggregation behaves like one rigid body. The transition from a static to a flowing state takes place when the shear stress reaches a certain threshold. The simplest assumption for the threshold at which yielding occurs is a coulomb friction correlation ($\tau_{fr} = \mu_i \cdot p_{fr}$), where μ_i is an inner friction coefficient of the material. Based on this assumption Schaeffer [100] proposed a formulation for the granular viscosity:

$$\mu_{fr} = \frac{p_{fr}\mu_i}{2|\boldsymbol{S}_s|} \tag{15}$$

The denominator of equation (15) contains the Euclidian norm of the deviatoric part of the strain-rate tensor $|\boldsymbol{S}_s| = \sqrt{S_{ij}S_{ij}}$. If the strain-rate (shear) approaches zero the viscosity diverges, which ensures the existence of a yield stress: the stress does not vanish when the flow stops [17].

The internal friction coefficient μ_i of the granular material is related to the angle of internal friction ϕ_i:

$$\mu_i = \sqrt{2}\sin(\phi_i) \tag{16}$$

Jop et al. [70] suggested an empirical correlation for a dynamic friction coefficient $\mu_i(I_s)$ depending on the dimensionless number I_s. I_s is called the inertial number and is a measure of whether the material exhibits a more solid-like or fluidized behavior. One could say, it is an indicator of the flow regime where the process takes place. The model of Jop et al. was primarily developed to describe granular flows with a free surface

down an inclined plane where a wide range of inertial numbers occur. In contrast to that, the present study investigates a confined flow. Furthermore, the inertial number of the investigated flow is very low ($I_s \lesssim 0.01$), which indicates that the process takes place in the quasi static flow regime where μ_i can be regarded as constant [17]. Therefore, the formulation of Schaeffer et al. using a constant value of μ_i according to equation (16) is applied.

4.1.2 Boundary conditions at the tube walls

At the tube surfaces the boundary conditions for the energy equation (8) and the momentum equations (6) and (7) have to be defined.

4.1.2.1 Temperature boundary condition

As mentioned in section 2.2, heat transfer between a surface and a contacting bulk involves a thermal contact resistance due to the gas gap between the surface and the first layer of particles. This contact resistance leads to a temperature drop $\Delta T = T_W - T_0$, directly at the surface as illustrated in Figure 13.

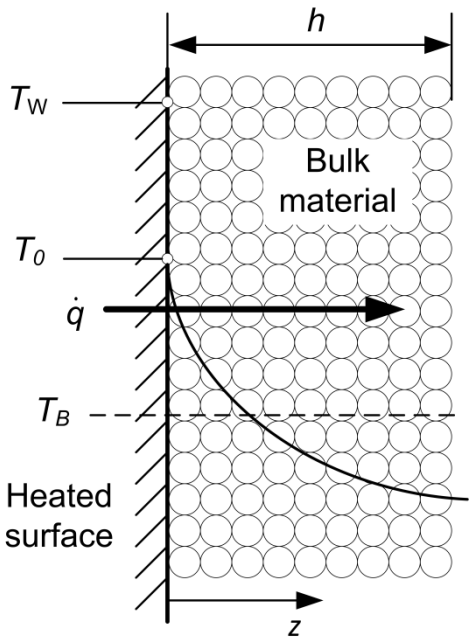

Figure 13. Schematic of the heat transfer between a bulk material and an immersed surface.

To avoid resolving this temperature drop, which would require a spatial resolution far below the particle size, it is directly incorporated into the boundary condition. In other

words, the temperature at the boundary is not the temperature T_W of the wall itself but a temperature T_0 which is reduced in accordance with the contact resistance $(\alpha_c)^{-1}$ and the heat transfer rate $\dot{q}$:

$$T_0 = T_W - \frac{\dot{q}}{\alpha_c} \tag{17}$$

The contact heat transfer coefficient, α_c, is calculated according to a formulation of Schlünder [3] which has been developed for resting bulks but has also been applied to moving beds [86]:

$$\alpha_c = \varphi\alpha_{WP} - (1-\varphi)\alpha_{con} + \alpha_{rad} \tag{18}$$

The contact resistance consists of three parts:

- Heat transfer to contacting particles ($\varphi \cdot \alpha_{WP}$).
- Heat transfer by conduction through the gas phase to the second layer of particles $(1\text{-}\varphi)\cdot\alpha_{con}$.
- Heat transfer by radiation α_{rad}.

α_{WP} denotes the heat transfer coefficient from the wall to a contacting particle which is being weighted by the factor φ denoting the fraction of the wall covered by contacting particles.

$$\varphi = \frac{N_p \frac{\pi d_p^2}{4}}{A_W} = \frac{N_p A_p}{A_W} \tag{19}$$

Here, N_p is the number of contacting particles, A_p is the projected area of a particle and A_W is the total surface area of the wall. Schlünder states an empirical value of $\varphi \approx 0.8$ for random pebble beds.

The second addend in equation (18), α_{con}, denoting the heat transfer coefficient to the second layer of particles, is accordingly weighted by the complement of the surface fraction $(1 - \varphi)$.

The magnitude of the contact heat transfer coefficient α_c is usually dominated by the heat transfer coefficient to a contacting particle α_{WP}. Schlünder evaluates α_{WP} based on the thermal conduction through the gas gap between the wall and the contacting particle and gives the following equation:

$$\alpha_{\mathrm{WP}} = \frac{4\lambda_{\mathrm{f}}}{d_{\mathrm{p}}}\left\{\left[1+\frac{2(l+h_{\mathrm{R}})}{d_{\mathrm{p}}}\right]\ln\left[1+\frac{d_{\mathrm{p}}}{2(l+h_{\mathrm{R}})}\right]-1\right\} \tag{20}$$

Equation (20) on the one hand includes two properties of the fluid, namely the mean free path way l and the thermal conductivity λ_{f}, on the other hand, two properties of the particle and the wall, namely the particle diameter d_{p} and the total surface roughness of particles and wall h_{R}.

Maximum values of α_{WP} are achieved at high conductivities λ_{f}, small particle diameters d_{p}, small surface roughness h_{R}, and small mean free path ways l. Of the last two quantities the larger one dominates the process. So, at ambient pressure ($l < 100$ nm) the surface roughness ($h_{\mathrm{R}} \approx 1\ldots10$ µm) is usually the dominating quantity.

The equations to calculate the remaining two heat transfer coefficients in equation (18), α_{con} and α_{rad} as well as the mean free path of the gas can be found in the appendix B.2.

The thermal boundary condition according to equation (17) defines the temperature at the boundary while the heat flux adjusts accordingly. In contrast to this, in the experimental setup described in section 3.2, the heat flux at the tube surface is defined and the corresponding temperature profile is measured. To compare the experiment with the simulation results (section 5.2.3), the wall temperature is set according to the measured temperature profile (see Figure 10, left).

4.1.2.2 Velocity boundary condition

The velocity boundary condition for the granular phase must take into account that the granular material may either slip along the wall or stick to the wall. This is of particular interest with regard to the transition from a static to a flowing regime in the upper part of the tube. At the top of the tube the particles are at rest but start to slide along the circumference when a certain angle of inclination is reached.

In order to model this process the Coulomb friction law is used to define the granular velocity at a solid wall. The wall shear stress in slip case is

$$\tau_{\mathrm{sl}} = \mu_{\mathrm{W}} p_{\mathrm{fr}}\,, \tag{21}$$

where μ_{w} is a wall friction coefficient, τ_{sl} is the (scalar) shear stress at the wall and p_{fr} is the normal stress. The wall shear stress is then compared to the viscose stress in tangential direction $\tau_{\mathrm{fr,t}}$ inside the particle assembly close to the wall [94] [99]:

$$\tau_{\mathrm{fr,t}} = \mu_{\mathrm{fr}} \left[\frac{d\boldsymbol{u}_{\mathrm{t}}}{d\boldsymbol{n}}\right]_W \tag{22}$$

The term $\left[\frac{d\boldsymbol{u}_t}{d\boldsymbol{n}}\right]_W$ is the gradient of the tangential part of the velocity $\boldsymbol{u}_{\mathrm{t}}$ in the direction of the unit normal vector $\boldsymbol{n}$ of the wall. By comparing equation (21) and equation (22) the (vectorial) shear stress at the wall is determined:

$$\boldsymbol{\tau}_{\mathrm{W}} = -\frac{\boldsymbol{u}_{\mathrm{s}}}{|\boldsymbol{u}_{\mathrm{s}}|} \begin{cases} \tau_{\mathrm{fr,t}} \text{ if } \tau_{\mathrm{sl}} > \tau_{\mathrm{fr,t}} \\ \tau_{\mathrm{sl}} \text{ if } \tau_{\mathrm{sl}} < \tau_{\mathrm{fr,t}} \end{cases} \tag{23}$$

If the viscose stress $\tau_{\mathrm{fr,t}}$ falls below the shear stress in slip case τ_{sl} ($\tau_{\mathrm{sl}} > \tau_{\mathrm{fr,t}}$) no sliding occurs at the wall. In case of $\tau_{\mathrm{sl}} < \tau_{\mathrm{fr,tan}}$ sliding occurs and the velocity at the boundary is calculated from $\boldsymbol{\tau}_{\mathrm{W}}$.

For the gas phase a no-slip boundary condition is used at the tube wall.

4.2 Discrete particle model

The modelling approach used in this work was first introduced by Cundall and Strack [20] and is known in literature as Discrete Element Method (DEM). In contrast to continuous model approaches, DEM tracks the motion of every single particle of the bulk. The method has become very popular in the last decades due to the rapid increase of available computational power and has been applied in various fields.

The method is based on solving the Newtonian equations of motion for each particle for translational and rotational motion.

$$\sum_{\mathrm{k}} \boldsymbol{F}_{\mathrm{i,k}} = m_{\mathrm{i}} \ddot{\boldsymbol{x}}_{\mathrm{i}} \tag{24}$$

$$\sum_{\mathrm{k}} \boldsymbol{M}_{\mathrm{i,k}} = J_{\mathrm{i}} \dot{\boldsymbol{\omega}}_{\mathrm{i}} \,. \tag{25}$$

The acting forces and moments include body forces such as the gravitational force as well as external forces and moments which, for example, may originate from contacts with other particles and walls.

When solving the equations of motion, two grains may turn out to overlap at the end of the time step. This overlap is interpreted as the elastic deformation which occurs for particles under stress [23]. The overlap is subsequently translated into tangential and normal interaction forces using certain contact models.

4.2.1 Contact models

Several contact models have been developed for the normal interaction force between particles [101]. Here, a linear hysteresis model is used which first has been introduced by Walton and Braun [25]. The instantaneous normal interaction force is calculated as follows:

$$F_{\mathrm{n}}^{\mathrm{t}} = \begin{cases} \min(F_{\mathrm{n}}^{\mathrm{t}-\Delta\mathrm{t}} + k_{\mathrm{ul}}\Delta s_{\mathrm{n}}, k_{\mathrm{l}} s_{\mathrm{n}}^{\mathrm{t}}), & \Delta s_{\mathrm{n}} \geq 0 \\ \max(F_{\mathrm{n}}^{\mathrm{t}-\Delta\mathrm{t}} + k_{\mathrm{ul}}\Delta s_{\mathrm{n}}, 0.001 k_{\mathrm{l}} s_{\mathrm{n}}^{\mathrm{t}}), & \Delta s_{\mathrm{n}} < 0 \end{cases} \tag{26}$$

The model distinguishes between loading case ($\Delta s_{\mathrm{n}} \geq 0$) and unloading case ($\Delta s_{\mathrm{n}} < 0$) where $\Delta s_{\mathrm{n}} = (s_{\mathrm{n}}^{\mathrm{t}} - s_{\mathrm{n}}^{\mathrm{t}-\Delta\mathrm{t}})$ is the change in normal overlap between two time steps. In the unloading case the normal force is limited to the value of $0.001 k_{\mathrm{l}} s_{\mathrm{n}}^{\mathrm{t}}$ to ensure that no negative (attractive) normal force occurs.

The inelastic nature of particle contacts is modelled by two different contact stiffnesses k_{l} and k_{ul} for the loading and the unloading case, respectively. k_{l} and k_{ul} are related to each other by the coefficient of restitution e:

$$e = -\sqrt{k_{\mathrm{l}}/k_{\mathrm{ul}}} \tag{27}$$

The contact stiffness for the loading case k_{l} is calculated by material parameters:

$$k_{\mathrm{l}} = \frac{E_1 d_{\mathrm{p},1} E_2 d_{\mathrm{p},2}}{E_1 d_{\mathrm{p},1} + E_2 d_{\mathrm{p},2}} \tag{28}$$

Here, indices "$_{1,2}$" denote the two elements forming the considered contact, which might either be a particle-particle contact or a particle-wall contact. d_{p} is the particle diameter, and E is the Young´s Modulus of the contacting elements [102].

The tangential interaction forces are calculated according to the following elastic-frictional force model:

$$F_{\mathrm{t}}^{\mathrm{t}} = \begin{cases} \min\left(F_{\mathrm{t}}^{\mathrm{t}-\Delta\mathrm{t}} + k_{\mathrm{l}}\Delta s_{\mathrm{t}}, \mu_{\mathrm{s}} F_{\mathrm{n}}^{\mathrm{t}}\right), & \text{if no sliding occurs} \\ \min\left(F_{\mathrm{t}}^{\mathrm{t}-\Delta\mathrm{t}} + k_{\mathrm{l}}\Delta s_{\mathrm{t}}, \mu_{\mathrm{d}} F_{\mathrm{n}}^{\mathrm{t}}\right), & \text{if sliding occurs} \end{cases} \tag{29}$$

As one can see from equation (29) the tangential contact force $F_{\mathrm{t}}^{\mathrm{t}}$ between two contacting elements evolves with the relative tangential displacement at the current time Δs_{t}. Sliding occurs, if $F_{\mathrm{t}}^{\mathrm{t}}$ exceeds the limit of $(\mu_{\mathrm{s}} \cdot F_{\mathrm{n}}^{\mathrm{t}})$, with μ_{s} being the static friction coef-

ficient. Once $F_{\mathrm{t}}^{\mathrm{t}}$ falls below the value of $(\mu_{\mathrm{d}} \cdot F_{\mathrm{n}}^{\mathrm{t}})$, with μ_{d} being the dynamic friction coefficient, the contact is considered non-sliding again.

For a reduced computational expense spherical particles are used in the simulations. Unfortunately, with this simplification the model loses its ability to predict the high resistance of non-spherical particles against a rolling motion. A common way to remedy this deficit is to introduce a resistive torque applied to contacting particles. The concept is known as "rolling friction" [103], and different classes of rolling friction models have been introduced. In this work an elastic-plastic spring dashpot model is used, commonly referred to as "Model C" [103], using a "rolling friction coefficient" μ_{roll} as an input parameter.

The resistive torque $\boldsymbol{M}_{\mathrm{roll}}^{\mathrm{t}}$ (at time t) is defined as follows [102]:

$$\boldsymbol{M}_{\mathrm{roll}}^{\mathrm{t}} = \min\left(\left|\boldsymbol{M}_{\mathrm{roll,e}}^{\mathrm{t}}\right|, M_{\mathrm{roll,lim}}\right) \frac{\boldsymbol{M}_{\mathrm{roll,e}}^{\mathrm{t}}}{\left|\boldsymbol{M}_{\mathrm{roll,e}}^{\mathrm{t}}\right|} \tag{30}$$

$M_{\mathrm{roll,lim}}$ is a limiting value of the torque, depending on the normal force F_{n}, the rolling resistance (rolling friction) coefficient μ_{roll}, and the rolling radius R_{roll}:

$$M_{\mathrm{roll,lim}} = \mu_{\mathrm{roll}} R_{\mathrm{roll}} F_{\mathrm{n}} \tag{31}$$

In case of mono-sized, spherical particles the rolling radius is $R_{\mathrm{roll}} = d_{\mathrm{p}}/2$. The rolling friction parameter μ_{roll} can be interpreted as the tangent of the maximum angle of a slope on which the rolling resistance moment counterbalances the moment produced by gravity in the particle. μ_{roll} is usually calibrated from experimental data as shown in the following section.

Below the limiting value $M_{\mathrm{roll,lim}}$, the resistive torque is allowed to vary continuously according to a linear elastic model:

$$\boldsymbol{M}_{\mathrm{roll,e}}^{\mathrm{t}} = \boldsymbol{M}_{\mathrm{roll}}^{\mathrm{t}-\Delta\mathrm{t}} - k_{\mathrm{roll}} \boldsymbol{\omega}_{\mathrm{rel}} \Delta t \tag{32}$$

$\boldsymbol{M}_{\mathrm{roll}}^{\mathrm{t}-\Delta\mathrm{t}}$ is the resistive torque at the previous time step, $\boldsymbol{\omega}_{\mathrm{rel}}$ is the relative angular velocity between the two contacting particles (wall and particle) and k_{roll} is the 'rolling stiffness':

$$k_{\mathrm{roll}} = R_{\mathrm{roll}}^2 k_{\mathrm{l}} \tag{33}$$

Due to the elastic part $\boldsymbol{M}^{\mathrm{t}}_{\mathrm{roll,e}}$ of the resistive torque, discontinuities as they occur in other rolling friction models are avoided [103].

4.2.2 Local averaging

The DEM basically yields location and velocity of every single particle at a given time. To compare the DEM-simulation results to those of the continuum-model and of the PIV measurements, they have to be averaged in space and time. For this purpose locally fixed control volumes (CVs) have to be defined wherein the averaging is carried out.

Lätzel [23] investigated two different averaging methods to compare his DEM simulations to experimental data of an annular shear cell. His basic averaging formalism for obtaining an averaged quantity Q inside a control volume V is

$$Q = \frac{1}{V} \sum_{i \,\epsilon\, V} w_{\mathrm{i}}^{\mathrm{V}} V_{\mathrm{i}} Q_{\mathrm{i}} \,, \tag{34}$$

with V_{i} being the particle volume and Q_{i} being the considered quantity attributed to particle i. In case of the averaged velocity ($Q = u_{\mathrm{x}}$, $Q = u_{\mathrm{y}}$) the quantity is averaged based on the number of particles N_{i} inside the control volume:

$$Q = \frac{1}{N_{\mathrm{i}}} \sum_{i \,\epsilon\, V} w_{\mathrm{i}}^{\mathrm{V}} Q_{\mathrm{i}} \,, \tag{35}$$

The parameter $w_{\mathrm{i}}^{\mathrm{V}}$ is the weight of the particles contribution to the average. In this work the simplest choice of $w_{\mathrm{i}}^{\mathrm{V}}$ is used which is

$$w_{\mathrm{i}}^{\mathrm{V}} = \begin{cases} 1, \text{if the center of the particle lies inside the CV} \\ 0, \text{otherwise} \end{cases} . \tag{36}$$

Lätzel showed that the method is sufficiently precise as long as the diameter of the CV is greater than the particle diameter. Consequently, the size of the CVs is set in such a way that this requirement is met. After averaging in space, time averaging is straightforward by taking the mean over multiple time steps. Depending on the quantities to be analyzed, the CVs may either by of rectangular shape, similar to the 2D-CVs in the PIV analysis (see section 3.1), or they may be arranged in circular layers, especially when analyzing quantities along a tube surface.

4.3 Model parameters

The reference parameters for both models are listed in Table 2. The material properties of the particles (the solid phase) are chosen to match those of quartz sand[3].

The surface friction coefficient, μ_W, of the tubes takes different values depending on the experimental set-up with which the simulation results are to be compared. In the experimental setup for measuring the heat transfer coefficient between tube and bulk, the tube surface is covered by a stainless steel foil (see section 3.2). For the surface friction coefficient of the foil a value of $\mu_{W,1} = 0.25$ is used. This value is based on the data of Baumann et al. [1] who measured the surface friction for various granular materials and obtained values of $\mu_W = 0.2 – 0.5$. For quartz sand on polished stainless steel he gives a value of $\mu_W = 0.25$.

The surface friction coefficient of the bare steel tubes (without the foil) used in the PIV measurement could not be measured directly. It is expected to be higher than that of polished stainless steel but to be within the bounds given by Baumann et al., i.e. $0.25 < \mu_W \lesssim 0.5$. An intermediate value of $\mu_{W,2} = 0.4$ is set for the surface friction coefficient of the bare steel tubes. In section 6.1 the influence of the wall friction coefficient on the simulation results is investigated revealing a moderate influence on the extent of the stagnant area whereas the rest of the flow field remains approximately unaffected.

Table 2. Reference parameters for the simulations.

Parameter	Symbol	Value	Unit
Particle diameter[4]	d_p	0.6	mm
Outlet/reference velocity	u_{ref}	5.0	mm/s
Density particles/solid phase	ρ_s	2600	kg/m³
Tube diameter	D_T	27	mm
Vertical tube spacing	s_V	variable	mm
Horizontal tube spacing	s_H	variable	mm
Tube wall friction coefficient (section 5.2.3)	$\mu_{W,1}$	0.25	-

[3] Except for the Young´s modulus (see section 4.3.2).

[4] For the geometry variations using the DEM simulations in section 6.1 a particle diameter of $d_p = 1.0$ mm is used to reduce the computational cost.

Tube wall friction coefficient (section 5.1 and 5.2.1)	$\mu_{W,2}$	0.4	-
Continuum model			
Density gas phase (air)	ρ_f	$f(T)$	kg/m³
Specific heat gas phase (air)	$c_{p,f}$	$f(T)$	J/kgK
Dynamic viscosity gas phase (air)	μ_f	33	10^{-6} Pa s
Total surface roughness (equation (20))	h_R	1.0	µm
Inner friction angle	ϕ_i	34	°
Share of tube surface covered by particles (equation (20))	φ	0.8	-
Loosest random packing (equation (14))	ε_{min}	0.5	-
Closest random packing (equation (14))	ε_{max}	0.65	-
Exponent in equation for $p_{fr}(\varepsilon_s)$ (equation (14))	r	2	-
Exponent in equation for $p_{fr}(\varepsilon_s)$ (equation (14))	s	5	-
Discrete particle model			
Youngs modulus of particles	E_p	10^6	N/m²
Friction coefficient between particles	μ_{pp}	0.2	-
Rolling friction coefficient	μ_{roll}	0.3	-
Coefficient of restitution	e	0.1	-
Surface friction coefficient at front wall (1)	$\mu_{front,1}$	0.0	-
Surface friction coefficient at front wall (2)	$\mu_{front,2}$	0.5	-
Surface friction coefficient at rear wall	μ_{rear}	0.0	-

4.3.1 Parameters specific to the continuum model

The material properties of the gas phase (air) in the continuum model are calculated according to tabular values in [104].

The surface roughness h_R and the parameter φ[5] are needed for the evaluation of the thermal contact resistance between bulk and tube surface (equation (18) and (20)). The

[5] φ denotes the fraction of the surface covered by contacting particles (see section 4.1.2.1, equation (18) and (20)).

value of $\varphi = 0.8$ is chosen according to Schlünder et al. [3]. The total surface roughness h_R is the sum of the roughness of the particles and the surface. Senetakis measured $h_{R,Sand} \approx 0.5$ µm in experiments with Leighton Buzzard sand. The surface roughness of cold-rolled stainless steel as it is used in the validation experiment in section 5.2.3 is typically $h_{R,surface} \approx 0.3…0.5$ µm [105]. Therefore set the total surface roughness is set to $h_R = h_{R,Sand} + h_{R,surface} \approx 1.0$ µm.

The values of the loosest and the closest random packing, ε_{min} and ε_{max}, as well as the two exponents, r and s, which are needed for the calculation of the granular pressure (equation (14)) between particles are set the same as in the work of Srivastava and Sunderesan [63].

4.3.2 Parameters specific to the discrete particle model

The input parameters of the DEM-model include material parameters such as the Young´s modulus as well as material interaction parameters like friction coefficients. A general review on the calibration of DEM models is given by Coetzee [106].

The Young´s modulus of the particles is set to $E_p = 10^6$ N/m² which is about three orders of magnitude lower than values of typical materials such as for example sand stone [107].

Using a reduced Young's modulus (reduced contact stiffness) is motivated by increasing the time step of the simulation which scales with the inverse square root of the contact stiffness ($\Delta t \sim 1/\sqrt{k_l}$) [108], leading to a substantial saving of computation time. This measure is very common in DEM models [106] and is justified as long as the normal overlap between particles is less than 1 % of the particle radius [30]. In the current case the maximum normal forces between particles are $F_{N,max} \approx 0.001$ N which corresponds to a normal overlap of 0.6 % of the particle radius (see equation (26)). Furthermore, to ensure independence of the simulation results on the contact stiffness, a variation of the Young's modulus was conducted (up to $E_p = 10^8$ N/m²) and virtually no impact was found (see appendix D.1).

In contrast to the contact stiffness, the friction parameters are expected to be determining for the simulation results. These are, on the one hand the static and dynamic friction coefficient according to which the tangential forces between particles are calculated (see equation (29), p. 36). On the other hand, there is the "rolling-friction" coefficient which is to account for the non-spherical shape of the real grains (see section 4.2.1).

Senetakis et al. [109] investigated the inter-particle coefficient of friction of Leighton Buzzard sand. They found that the coefficient of dynamic friction (μ_d) and the coefficient of static friction (μ_s) are of very similar magnitude and they measured values of $\mu_s \approx \mu_d = \mu_{pp} = 0.1 \ldots 0.23$.

Given the inter-particle coefficient of friction $\mu_{pp} = 0.2$, the rolling friction coefficient μ_{roll} was obtained from a dedicated laboratory experiment. In the experiment the static angle of repose $\phi_r \approx 34°$ of the bulk was determined. Subsequently, the rolling friction coefficient was adjusted such that the measured value was attained in the simulation, which leads to $\mu_{roll} = 0.3$. In appendix D.3 a brief sensitivity study is given of the influence of the friction parameters on the simulation results.

At the front and rear boundary of the geometry (see side view in Figure 11, p. 26) the surface friction coefficient is set to zero ($\mu_{front,1}$, μ_{rear}). This reflects an idealized flow section inside the bulk. However, the validation experiment (see section 3.1) captures the flow field visible at the acrylic glass front wall. Therefore, surface friction of the front wall needs to be considered.

To this end, an annular shear cell is used to measure the wall friction coefficient between quartz sand and an acrylic glass surface. The friction coefficient turns out to be not constant but to depend on the normal stress between surface and bulk. Hence, to determine the friction coefficient applicable to the PIV-measurement setup, the normal (horizontal) stress on the acrylic glass front wall of the mockup needs to be estimated. This is done by applying the well-known model developed by Janssen (e.g. in [17]), which yields a horizontal stress $\sigma_H \lesssim 2000$ Pa. The measured friction coefficient for this normal stress is $\mu_{front,2} \approx 0.5$. Further details on the measurement of the surface friction coefficient are given in appendix A.4.

5 Validation

A two-pronged strategy is adopted to validate the discrete particle model and the continuum model. In a first step the granular flow field obtained from the discrete particle model is validated using PIV analysis. The flow field of the continuum model is subsequently validated using the discrete particle model.

In a second step the heat transfer model, which is only part of the continuum model, is validated based on the measurement data of the local heat transfer coefficient.

5.1 Discrete particle model

For the validation of the discrete particle model the PIV measurement setup is used as described in section 3.1. The tube arrangement was TA3 (see Table 1) and an intermediate flow speed was adjusted (u_{ref} = 4.0 mm/s). The specific focus is on the simulation of the flow field close to the acrylic glass front wall as this is the area which is captured by the experiment. Therefore, the surface friction between bulk and acrylic glass at the front wall is considered in the model ($\mu_{front,2}$ = 0.5, see section 4.3.2).

Figure 14 shows contour plots of the granular flow field around a single tube obtained from the PIV measurement (left) and DEM simulation (right). The tube in the experimental plot is located in the center of the mockup (see framed area in Figure 5 (right), (p. 16)).

Essentially, Figure 14 shows good agreement between simulation and experiment. However, while the simulated velocity profile is symmetric to the vertical center line of the tube, the experimental profile is slightly asymmetric. Higher velocities are observed on the left half of the plot. This asymmetry of the measured profile is due to disturbing effects in the experimental setup originating from the upstream row of tubes, from the side walls and from the tube chain conveyor (see also Appendix A.3).

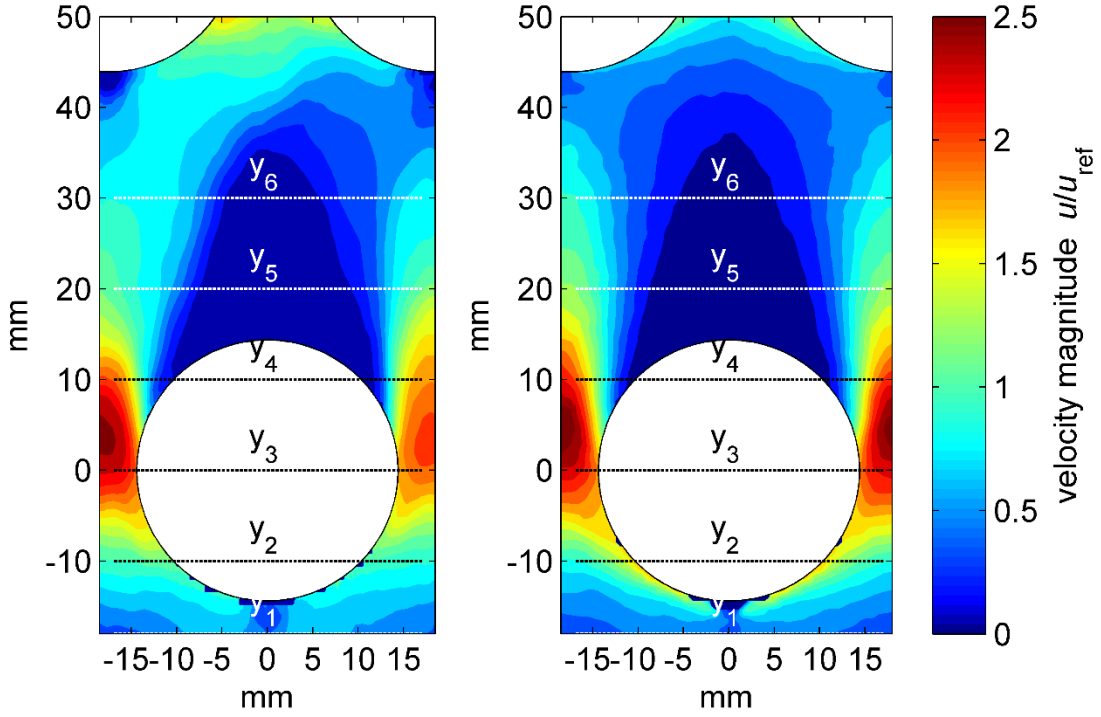

Figure 14. Contour plots of granular flow speed. Left: PIV-measurement. Right: DEM-simulation

A cone-shaped stagnant area forms above the tube wherein the flow speed is approximately zero. This stagnant zone is framed by areas of increased particle motion. A continuous transition from the static to the flowing regime is observed. Size and shape of the stagnant area are similar in simulation and experiment. Such stagnant zones have been reported in earlier studies [89] [2] [91]. They are of major importance for the design of moving bed heat exchangers as they hamper the heat transfer from the tube surface to the bulk material due to decreased convective transport.

At the lateral sides of the tube, the flow velocity increases due to the constriction of the flow cross section. Both plots coherently show the maximum flow speed to occur at $y \approx 5$ mm which is slightly above the center point of the tube ($y_3 = 0$). A velocity gradient is observed in radial direction at the tube surface.

In the simulation, for the lower half of the tube a thin layer of elevated velocity is observed directly at the tube surface. In the experiment this layer is not observed and the velocity at the tube surface is much lower. This deviation is attributed to the formation of a void area below the tube and will be addressed in more detail in the following section.

For a more detailed comparison between simulation and experiment, Figure 15 (a) and (b) show the velocity magnitude of the flow along the horizontal lines y_1 to y_6 as displayed in Figure 14.

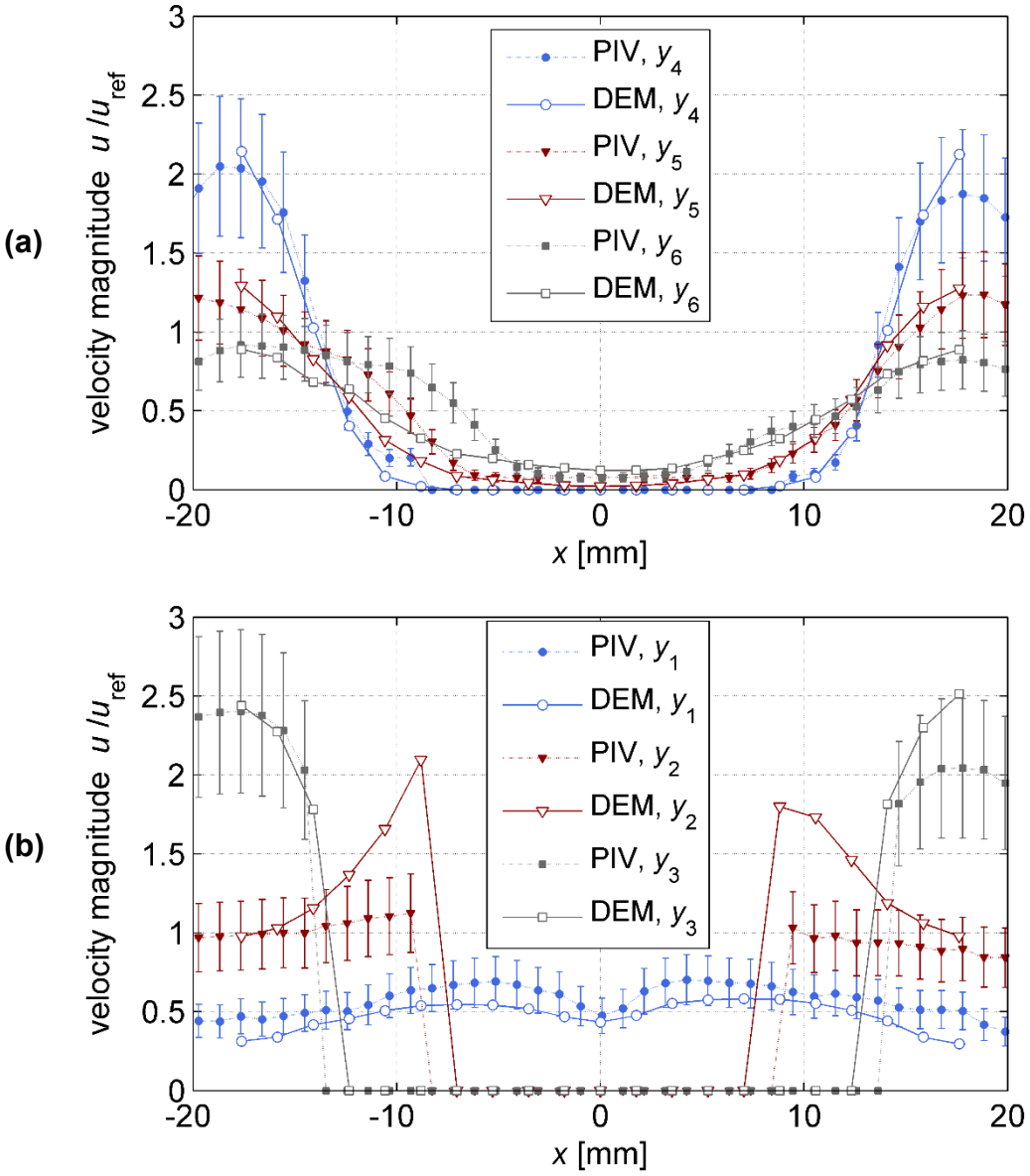

Figure 15. Horizontal velocity profiles at different heights (see Figure 14). (a) Upper half and above the tube. (b) Lower half and below the tube. Solid lines: PIV-Measurement. Dotted lines: DEM-simulation.

Figure 15 (a) shows the horizontal velocity profiles of simulation and experiment in the upper half and above of the tube (y_4, y_5 and y_6). Velocities close to zero are observed in the center of the plot ($x \approx 0$ mm) where the horizontal profiles intersect the tube (y_4) and the stagnant area above the tube (y_5, y_6). At the sides of the plot the velocity increases as the horizontal planes reach into the area of increased particle motion.

On the right hand side and in the center of Figure 15 (a), simulation and experiment agree well. On the left hand side of the plot (left hand side of the tube) deviations on planes y_6 and y_5 are observed in the range of -14 mm $\lesssim x \lesssim$ -7 mm. This x-range is associated with the transition from the stagnant to the flowing regime. Due to the horizontal asymmetry in the experimental data, this transition is more distinct on the left hand side than on the right.

Figure 15 (b) shows the horizontal velocity profiles of simulation and experiment in the lower half and below the tube (y_1, y_2 and y_3). Planes y_3 and y_2 intersect the tube and show a jump of the flow speed at the tube surface. Plane y_1 is located below the tube.

Plane y_3 again displays the asymmetry of the experimental profile already mentioned. The simulation agrees better on the left than on the right hand side of the plot.

Plane y_2 intersects the tube surface at $x \approx \pm 9$ mm which is obvious by the jump in flow speed in both plots. At a greater (horizontal) distance from the tube surface ($|x| > 16$ mm) simulation and experiment yield similar velocity magnitudes. Directly at the surface, however, the flow speed in the simulation is about twice as high as in the experiment. These deviations occur on both sides of the tube and cannot be attributed to the asymmetry of the experimental flow profile. They have already been noticed in the contour plots in Figure 14 where a thin layer of elevated flow speed is observed in the lower half of the tube in the simulation but not in the experiment. The reason for the deviation deserves further discussion and will be addressed in detail in the following section.

Plane y_1 shows a relatively even profile. Both, simulation and experiment, show a small dip in the profile in the center of the plot where the flows from both sides merge below the tube.

The results presented in this section can be summarized as follows:

Deviations between simulation and experiment are primarily attributed to the asymmetry of the measured flow field. As a consequence, maximum deviations of up to 50 % of the reference velocity ($|\Delta u|/u_{\mathrm{ref}} < 0.5$) are observed, but only in specific areas (especially y_5 (left) and y_6 (left)).

Furthermore, major deviations between simulation and experiment are observed in a very narrow region below the tube where the simulation yields much higher velocity

magnitudes than the experiment due to the formation of a void area. These deviations are addressed in the following section.

In the rest of the flow field simulation and experiment agree well, and the absolute deviations are less than 15 % of the reference velocity ($|\Delta u|/u_{ref} < 0.15$)

5.1.1 Velocity profile at the tube surface

The flow pattern close to the tube surface is of major importance for the heat transfer from the tube surface to the bulk. Therefore, in this section simulation and experiment are compared based on the velocity profile along the tube surface.

Figure 16 (left) shows the velocity profiles of PIV measurement and DEM simulation along the entire circumference of the tube. The plots denoted by "$PIV_{1.5}$" and "$DEM_{1.5}$" are profiles at a distance of 1.5 particle diameters (≈ 0.9 mm) from the tube surface. In addition a third plot is given ("DEM_4") which shows the calculated velocity profile along the tube surface at a distance of four particle diameters (≈ 2.4 mm) from the tube wall.

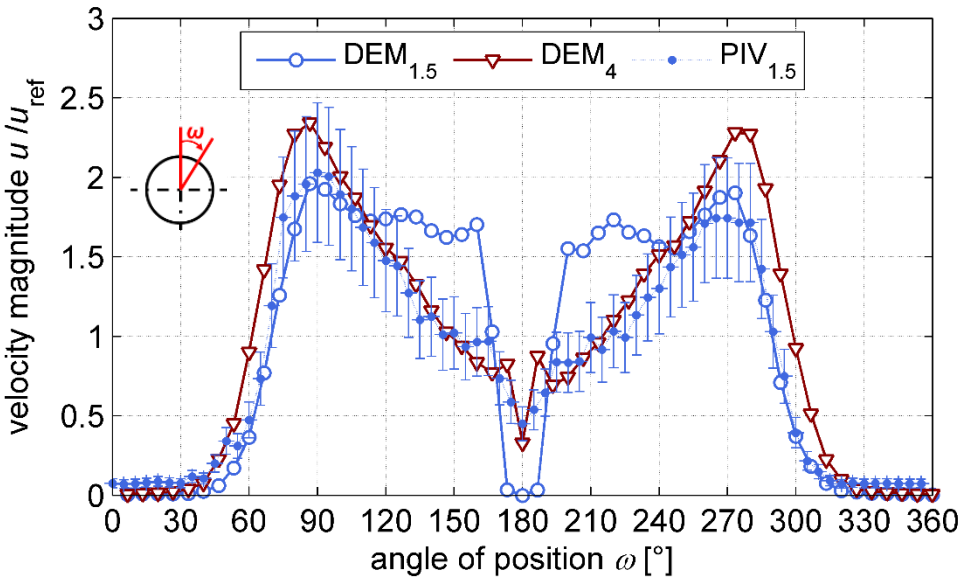

Figure 16. Flow speed along the tube surface. $DEM_{1.5}$ and DEM_4: velocity profiles from simulation at a distance of 1.5 and 4 particle diameters from the tube surface. $PIV_{1.5}$: velocity profile from measurements at a distance of 1.5 particle diameters from the tube surface.

The stagnant area is located around the tube vertex, and the flow speed is found to be close to zero in the range of $\omega \lesssim 50°$ and $310° \lesssim \omega$ in all three plots. However, the measurement shows slight motion also in the stagnant area ($u/u_{ref} \approx 0.07$) whereas in the simulation the flow is virtually at rest ($u/u_{ref} \approx 0.005$). At $\omega \approx \pm 50°$ from the tube vertex the velocity rises and reaches a maximum at $\omega \approx 90°$ ($\omega \approx 270°$). To this point, simulation and experiment ($DEM_{1.5}$ and $PIV_{1.5}$) deviate by less than 10 % of the reference velocity ($|\Delta u|/u_{ref} < 0.1$)

Around the lower half of the tube ($90° < \omega < 180°$), the plot of $DEM_{1.5}$ differs significantly from the measured profile $PIV_{1.5}$. The simulated profile remains at a high level until it drops to zero at $\omega \approx 160°$. In contrast to that, the experimental profile displays a continuous decrease of flow speed until a minimum of $u/u_{ref} = 0.5$ is reached directly below the tube. This resembles very much the simulated profile DEM_4 at a greater distance from the wall.

These deviations around the lower part of the tube have already been observed in the previous section (see y_2 in Figure 15 (b)) and are explained as follows: Below the tube a void zone forms as illustrated in Figure 17.

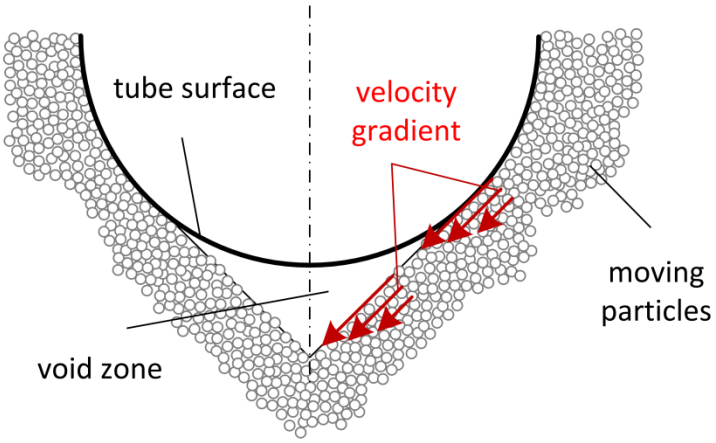

Figure 17. Flow pattern in the lower part of the tube. Elevated velocities and high velocity gradients occur at the flanks of the void area below the tube.

In the range of $160° < \omega < 200°$ no particles are found at the tube surface and hence the velocity is zero. In the range of $120° < \omega < 160°$ ($200° < \omega < 240°$) the particles gradually lose touch with the tube surface before the actual void area is formed. As a consequence the decelerating impact of the wall friction decreases and the particles start to

accelerate along the slope. As can be seen in Figure 16, the effect is confined to a narrow region directly at the tube surface. At a distance of four particle diameters from the surface no elevated velocities are observed anymore (see "DEM_4" in Figure 16).

The void area as well is visible in the experimental setup. In the raw measurement data (raw images) particles are observed moving down the slope very fast. However, the subsequent PIV analysis does not capture the effects, most likely as the corresponding region is too narrow and the velocity gradient is too large.

The comparison of the simulated and the measured velocity profiles at the tube surface leads to the following conclusion:

In the angular range of $0° < \omega < 120°$ ($240° < \omega < 360°$) the absolute deviations of simulation and experiment are $|\Delta u|/u_{ref} < 0.1$. They both coherently yield a stagnant area ($u \approx 0$) in the range of $\omega < 50°$ ($\omega > 210°$) and a maximum flow velocity at $\omega \approx 90°$.

In the range of $120° < \omega < 240°$ the numerical model yields significantly higher flow speeds directly at the tube surface due to the formation of a void area. The area where this effect occurs is too small to be captured by the measurement. Hence, the model cannot be accurately validated in this area. The deviations diminish with increasing distance from the tube surface, and at a distance of four particle diameters the absolute deviations are $|\Delta u|/u_{ref} < 0.1$.

5.1.2 Influence of the front wall friction on the measured flow field

Many researchers have found granular materials to move as a "plug-flow" in different experimental setups in the past (e.g. [76] [56] [87]). In case of a plug-flow the velocity of the flow is assumed to be constant across the flow cross-section. Applying this assumption in the direction of the tubes axes, i.e. z-direction, suggests that the flow profile inside the bulk – virtually inaccessible for measurements – should be the same as the one perceived at the acrylic glass front.

To check whether this assumption holds true for the case at hand the validated DEM model is used to predict the inner flow field. Figure 18 shows two contour plots: The plot on the left corresponds to the simulation data presented in the preceding sections and displays the flow directly at the front wall with $\mu_{front,2} = 0.5$. The plot on the right displays the flow inside the bulk excluding the effect of confining walls ($\mu_{front,2} = 0.0$)

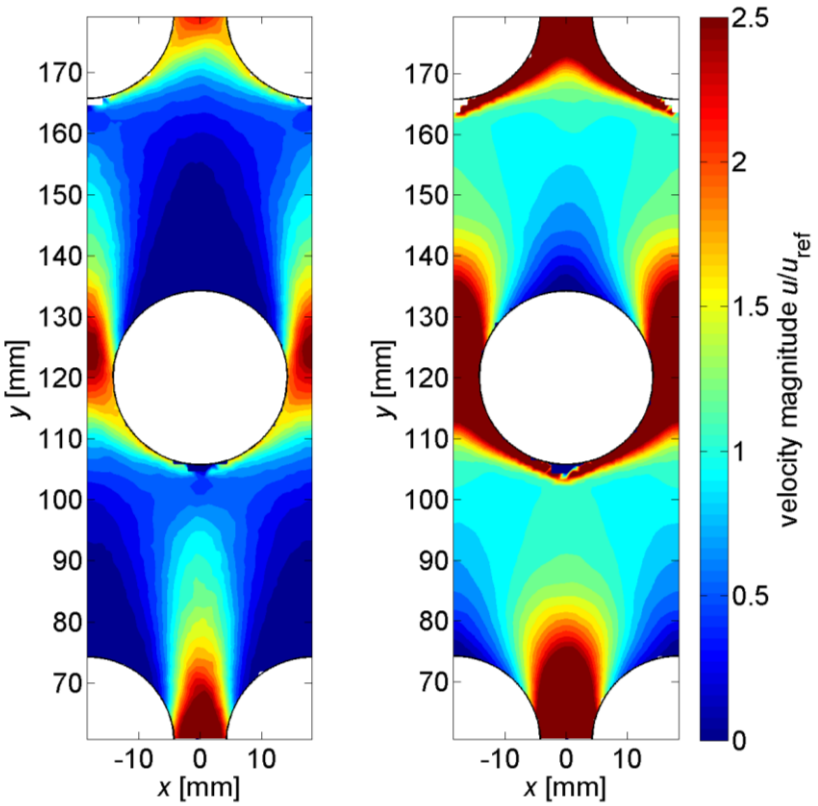

Figure 18. Contour plots of granular flow speed obtained from DEM simulations. Left: Flow directly at the front wall taking wall friction into account (μ_{front} = 0.5). Right: Flow inside the bulk and μ_{front} = 0.0.

Obviously, at the front wall (Figure 18, left) the flow is considerably slower and the stagnant area above the tube is significantly larger than inside the bulk (Figure 18, right). The influence of the void area, leading to elevated flow speeds below the tube, increases inside the bulk. Thus, in *z*-direction the plug-flow assumption is not valid in the considered case.

It is concluded that the validation experiments depend on a careful consideration of the surface friction of the front wall. Furthermore, the results of the preceding sections show that this influence is well captured by including the measured friction coefficient in the model.

5.2 Continuum model

As discussed in the previous section, the experimental validation of the flow field of the 2D-CFD model is not possible due to the boundary effects occurring in the PIV-

measurements. Instead, the validated DEM model is used for the validation of the flow field.

Subsequently, the CFD is used model to calculate the local heat transfer coefficient at the tube surface. The simulation results are compared to the measurement data obtained from the experimental setup described in section 3.2.

5.2.1 Flow field and packing fraction

The comparison of the flow fields obtained from the DEM- and CFD model is conducted based on the three tube arrangements TA1, TA2 and TA3 as defined in Table 1. The remaining simulation parameters are given in Table 2.

Figure 19 shows the contours of the flow speed obtained from the two models for the three tube arrangements. The results of the CFD model represent the velocity magnitude of the granular phase. The DEM results represent the particle velocities, averaged in space and time per control volume.

Both models coherently predict a stagnant area on top of the tubes. Furthermore, both models agree well regarding the size and the shape of the stagnant zone which changes according to the tube arrangement. Minor differences regarding the shape of the stagnant zone are visible for TA1 where the DEM results show a more curved shape, whereas the continuum model yields a more tapered shape.

In a former work Niegsch [86] assumed that the stagnant area is confined by slip planes as they occur in triaxial tests with over-consolidated clays [110], separating resting from moving particles. If such a distinct transition from “static” to “flowing” were the case, it could only be captured by the DEM model as the CFD model is continuous per definition. However, both models coherently show a continuous transition in contradiction to the assumption of distinct slip planes.

At the lateral sides of the tubes, a maximum of the velocity magnitude occurs due to the constriction of the flow cross section. The velocity magnitude decreases towards the tube surface due to wall friction but is not zero directly at the surface. The shear motion takes place in a narrow area near the wall, which is typical for dense granular flows [23]. The maximum flow speed at the lateral sides of the tubes is slightly higher in the DEM simulation.

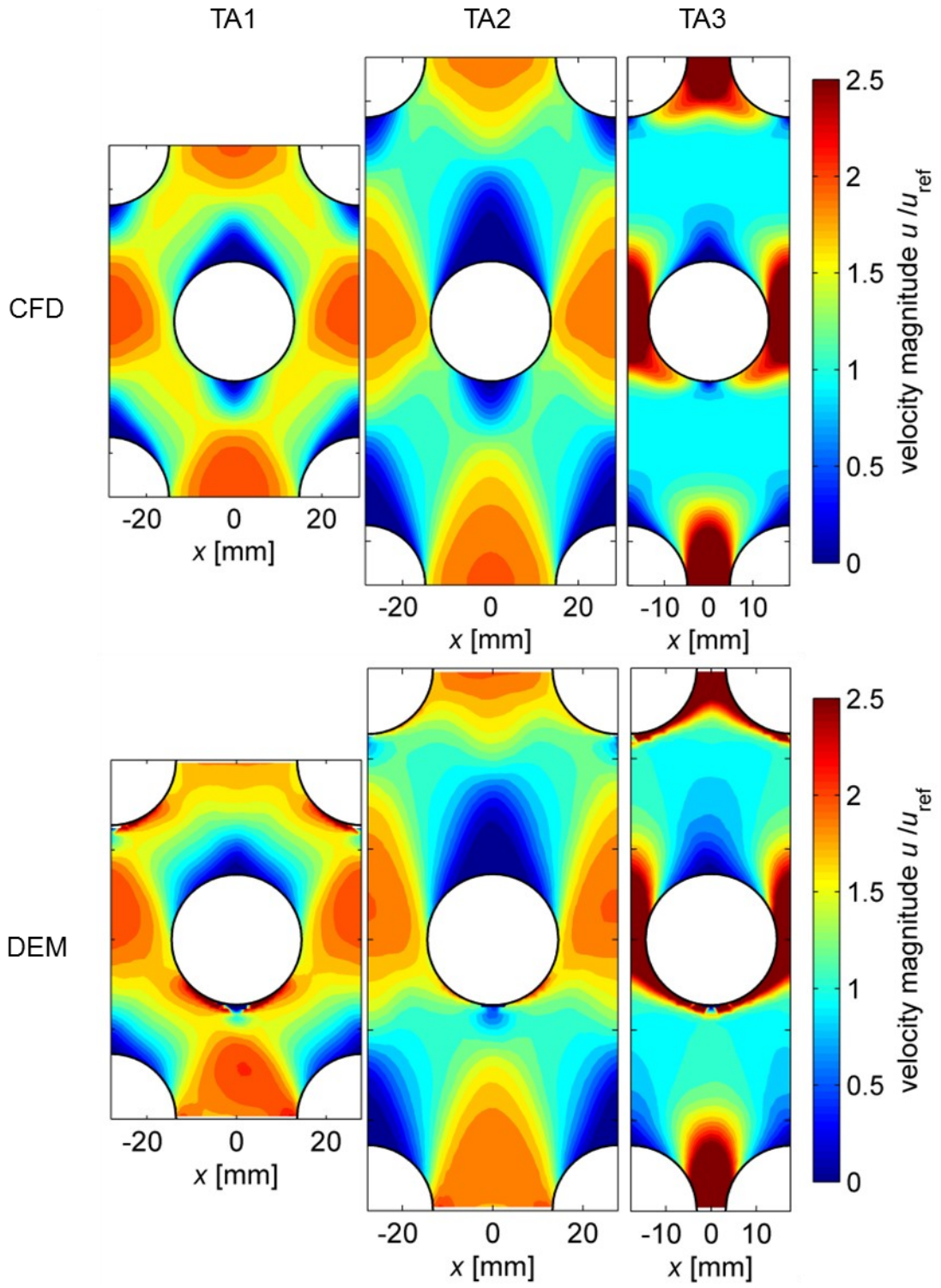

Figure 19. Contour plots of velocity magnitude at different tube arrangements. Comparison of continuum model (top) and DEM-model (bottom).

Around the lower half and underneath the tubes, increased deviations are observed between the predicted flow fields. The DEM model yields a void zone where the packing fraction ε_s is zero (see Figure 20 (left)). The inclination of the flanks of this void zone is approximately the angle of repose of the material ($\phi_r = 34°$). In contrast to that, the con-

tinuum model yields only a slight decrease of the packing fraction below the tube (see Figure 20 (right)).

Similar observations have been made by other researchers in the past. For example, Nikolopoulos et al. [111] applied a similar continuum model to simulate a heap of granular material and compared the resulting repose angle to experimental data. They observed that the model cannot produce a static angle of repose. Instead the material "deliquesces" at the free surface of the bulk. They found the reason for this behavior in the fact that the model does not include any viscous normal stresses.

To account for the decrease in heat transfer resulting from the formation of the void area, the CFD model needs to be modified. These modifications will be addressed in section 5.2.2.

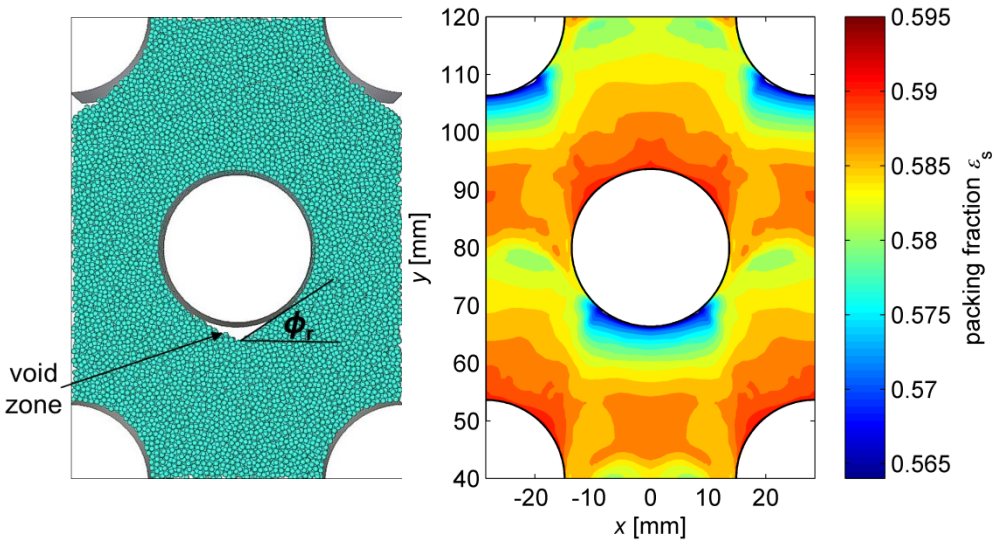

Figure 20. Particle assembly from DEM simulation (TA1) with void area below the tube (left). Contour plot of packing (TA1) fraction from CFD model (right).

5.2.1.1 Velocity profile and packing fraction at the tube surface

The velocity profile in the direct vicinity of the tube surface has major impact on the heat transfer from the tube surface to the moving bulk. Therefore, accurate modelling in this region is of particular importance.

Figure 21 shows the velocity profiles at the tube surface obtained from the DEM and CFD model. In the upper part of the tube where the stagnant area is found the deviations between the two models differ for each of the three geometries:

For TA1 the DEM yields significant particle motion already at the top of the tube ($\omega < 30°$) while the CFD model yields velocities close to zero. In the range $40° \lesssim \omega \lesssim 90°$ the CFD model yields larger velocity magnitudes than the DEM model. The maximum deviations are up to 35 % of the inlet velocity ($\Delta u/u_{ref} < 0.35$)

For TA2 both models agree well, especially for $\omega < 50°$. Maximum deviations ($\Delta u/u_{ref} < 0.2$) occur in the range of $50° \lesssim \omega \lesssim 90°$.

For TA3 the CFD model yields considerably higher flow speeds in the range of $20° \lesssim \omega \lesssim 60°$ ($\Delta u/u_{ref} < 0.4$). Apart from that, the two models agree well in the upper part of the tube.

The angular coverage of the stagnant area is estimated from the results of the DEM model by inserting a tangent to the plots (see dot-dashed lines in Figure 21). It is assumed that the transition from the static to the flowing regime is marked by a distinct acceleration of the particles, and hence the tangents are inserted at the point of largest slope of the plots. This yields $\omega_{SZ} \approx 50°$ for TA2 and TA3 and $\omega_{SZ} \approx 40°$ for TA1.

At the lateral sides of the tube around $\omega = 90°$ the two models yield similar magnitudes of flow speed. In this range, the DEM model shows a plateau of flow speed while the CFD model for TA2 and TA3 produces local maxima of flow speed. The absolute deviations in this area are less than 20 % of the reference velocity ($\Delta u/u_{ref} < 0.2$).

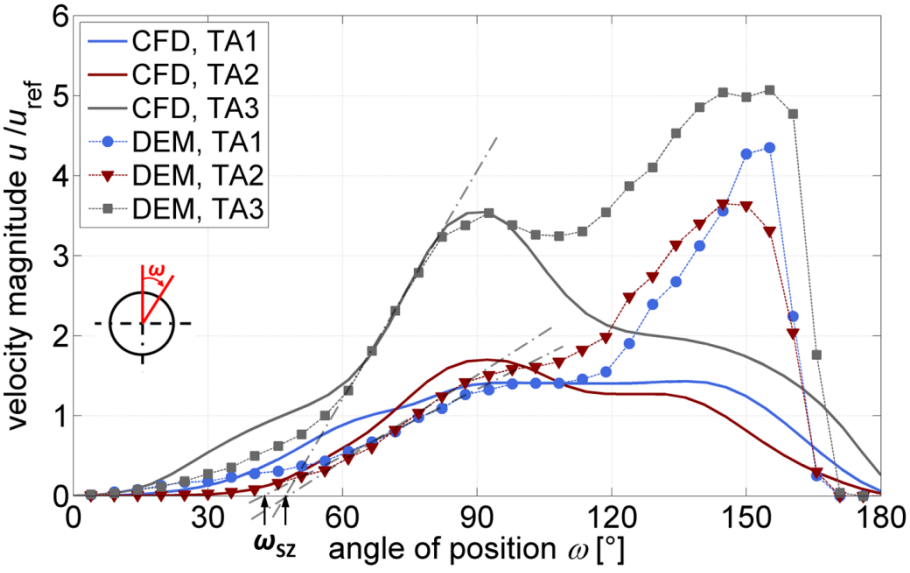

Figure 21. Velocity magnitude along the tube surface for three different tube arrangements. Solid lines: CFD model. Dashed lines with symbols: DEM model.

At the lower part of the tube ($120° \lesssim \omega \lesssim 160°$) all three DEM plots show a pronounced maximum of flow speed. This effect is associated with the formation of the void area and has already been discussed in section 5.1. As the CFD model doesn´t capture the void area it also does not predict these maxima of flow speed.

However, it is important to note that the maxima of flow speed around the lower part of the tube obtained from the DEM simulations is accompanied by a reduction of the packing fraction. This means that in spite of an increased velocity level, the mass flow rate at the tube surface remains almost unaffected. This is illustrated in Figure 22 and Figure 23.

Figure 22 shows the packing fraction along the tube surface for both models by the example of TA2. The CFD model yields a more or less constant packing fraction of $\varepsilon_s \approx 0.6$ around the tube. This agrees well with the DEM model at a distance of three particle diameters from the tube surface (DEM, $3d_p$).

Directly at the tube surface (DEM, $1d_p$), the DEM shows a reduced packing fraction of $\varepsilon_s \approx 0.5$ for $\omega \lesssim 120°$ due to the anisotropic packing structure and increased voidage near the wall. This effect is taken into account in the continuum model by the thermal contact resistance $(\alpha_c)^{-1}$ described in section 4.1.2. In the range of $120° \lesssim \omega \lesssim 160°$ of the DEM results the packing fraction decreases from $\varepsilon_s = 0.5$ to $\varepsilon_s = 0$, which is exactly the range where the DEM model yields elevated flow speeds (see Figure 21).

Figure 23 shows the (specific) mass flow rate of the solid phase at the tube surface:

$$\dot{m} = u_s \varepsilon_s \rho_s \tag{37}$$

The DEM results show that the reduction of the packing fraction ε_s approximately compensates for the increase in the flow speed u_s in the lower part of the tube. Therefore, the mass flow rate shows only a minor increase in the range of ($120° \lesssim \omega \lesssim 160°$).

This has important implications regarding the heat transfer in this area: The acceleration of the flow in the lower part of the tube does not enhance the convective heat transfer at the tube surface. Instead, the heat transfer rate is expected to decrease in this area as the effective density of the bulk decreases and less particles are in touch with the tube wall.

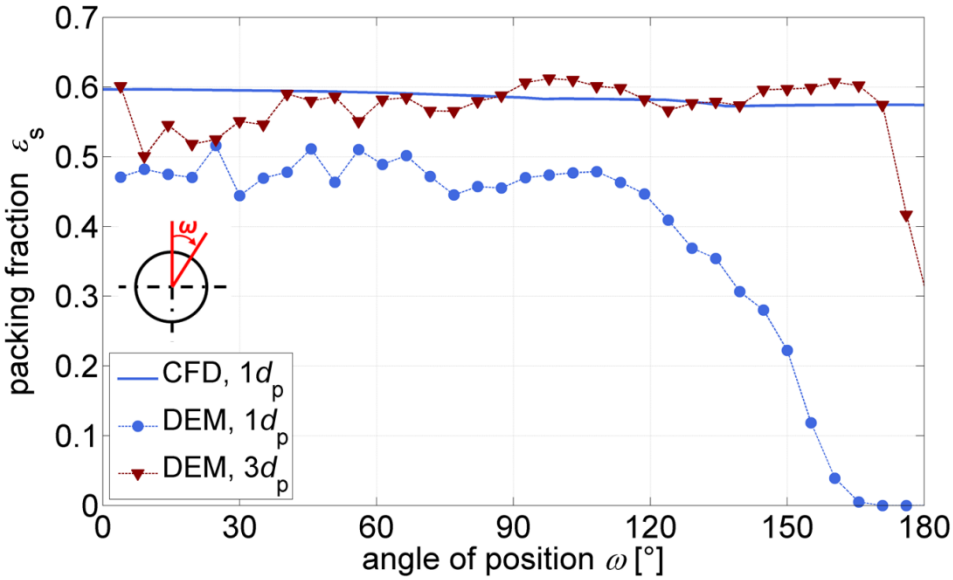

Figure 22. Packing fraction along the tube surface (only TA2) at a distance of one ($1d_p$) and three ($3d_p$) particle diameters from the tube surface. Solid line: CFD model. Dashed lines with symbols: DEM model.

The CFD results in Figure 23 exhibit the same shape as the velocity profiles in Figure 21 as the packing fraction doesn't change along the tube surface. Due to the decreasing packing fraction in the DEM simulations, the deviations between CFD and DEM in the lower part of the tube are less pronounced than for the velocity profiles.

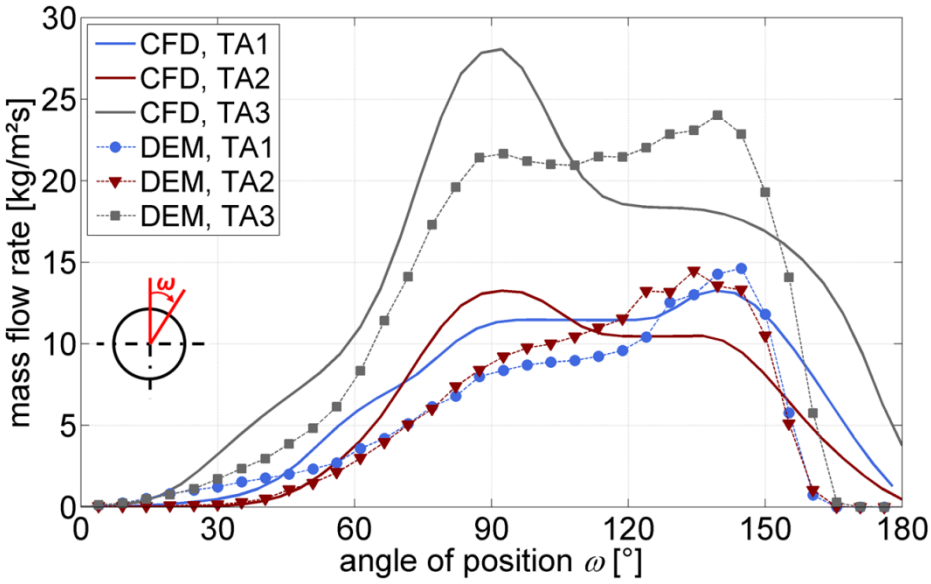

Figure 23. Mass flow rate along the tube surface for three different tube arrangements. Solid lines: CFD model. Dashed lines with symbols: DEM model.

Figure 24 displays the velocity magnitude along the vertical center line above the tube vertex for all three investigated geometries.

The largest deviations occur for TA3 ($\Delta u/u_{ref} < 0.25$) whereas better agreement is found for TA1 and TA3 ($\Delta u/u_{ref} < 0.18$). The height of the static zone, H_{SZ}, is estimated by inserting a tangent to the plots and taking the intersection with the x-axis (see dot-dashed lines in Figure 24). For TA2, $H_{SZ} \approx 15$ mm ($0.56 \cdot D_T$) is found and for TA1 and TA3 $H_{SZ} \approx 4$ mm ($0.15 \cdot D_T$).

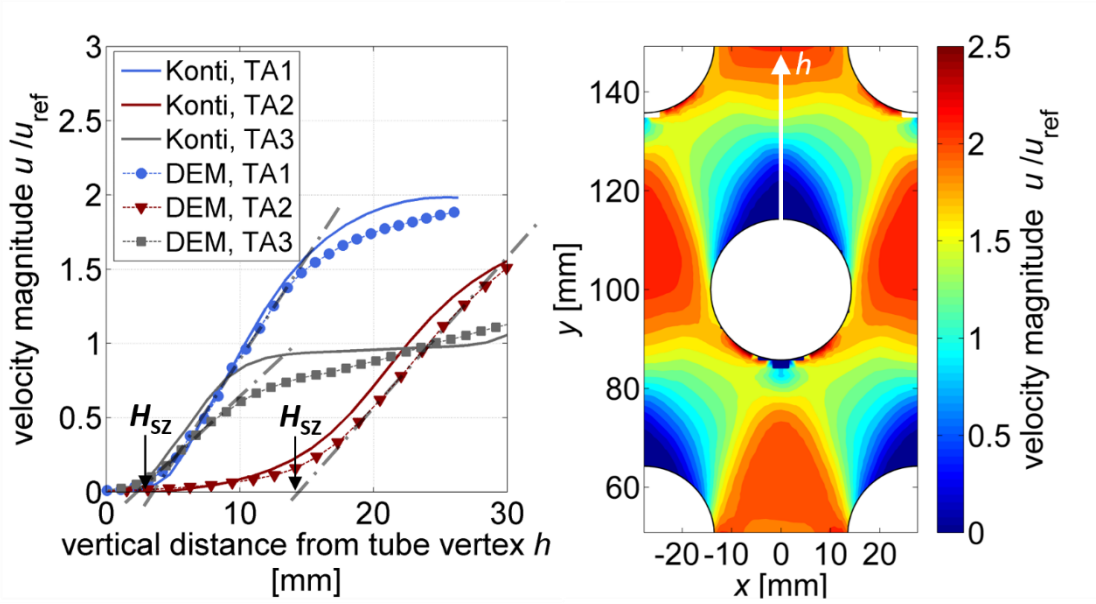

Figure 24. Flow speed along vertical section plane above tube vertex (see Figure 11). Solid lines: CFD model. Dashed lines with symbols: DEM model.

5.2.1.2 Shear Stresses

Figure 25 shows a comparison between continuum model and discrete particle model regarding the shear stresses in the flowing bulk material. The shear stresses are represented by the Euclidian norm of the deviatoric part of the stress tensor:

$$||\boldsymbol{\tau}|| = \left(\sum_{ij} \tau_{ij}^2 \right)^{1/2} \tag{38}$$

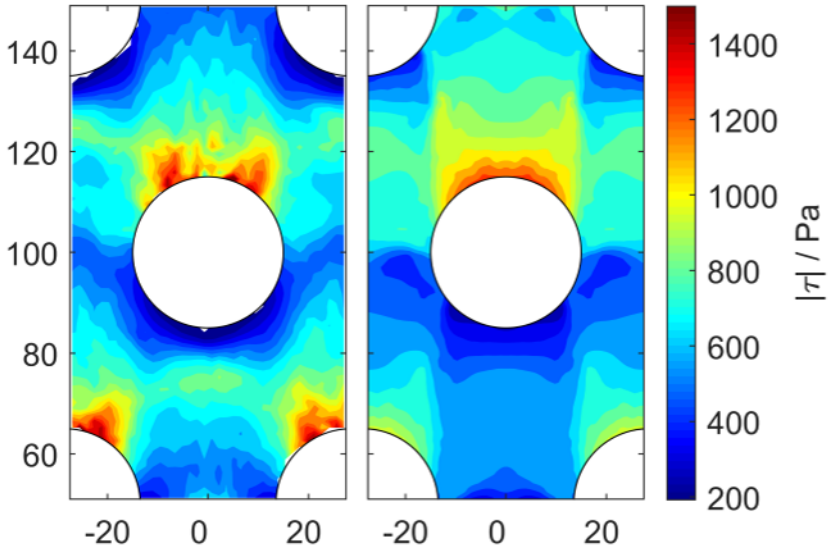

Figure 25. Shear stress (Euclidian norm of deviatoric part of the stress tensor) inside the granular flow. Left: DEM-model. Right: Continuum model.

Both models agree regarding the qualitative stress profile and the order of magnitude of the stresses. At the top of the tubes, increased shear stresses are observed while the shear stress decreases significantly in the lower half of the tubes.

Especially at the top of the tubes, the DEM model shows a more uneven stress profile which is attributed to the very small particle motion and therefore long time constants of the flow pattern in these areas.

5.2.2 Modification of the continuum model

The comparison of the DEM-model with the CFD-model regarding the granular flow field leads to the following conclusion: For the upper half of the tube ($0° < \omega \lesssim 110°$) the two models yield similar velocity profiles along the tube surface, and the absolute deviations are $|\Delta u/u_{\mathrm{ref}}| < 0.4$. Both models coherently yield a packing fraction of $\varepsilon_s \approx 0.6$ inside the bulk. Furthermore, the models agree well regarding the shape and size of the stagnant zone and its dependence on the tube arrangement.

Therefore, the continuum model is considered trustworthy for the upper half of the tube. However, major deviations regarding the flow speed at the tube surface occur for the lower part of the tube ($110° \lesssim \omega \leq 180°$) associated with the formation of the void area. These deviations call for a modification of the continuum model.

One possible option would be the modification of the hydrodynamic description of the granular flow, e.g. by involving an elaborate yield function and a bulk viscosity to include normal viscous stresses as done by Nikolopoulos et al. [111].

Such an alternate model has been compared to the one at hand for the considered case. However, while the convergence of the simulation changes for the worse and the simulation time increases significantly, the improvement of the simulation results is small. This is mostly due to the fact that the continuum model can only approximate the distinct jump of the packing fraction at the flanks of the void zones by a finite gradient.

In addition, the measurement data – which will be presented in section 5.2.3.1 – show that the heat transfer coefficient in the realm of the void area is small and that its contribution to the overall heat transfer rate is only about 5 %.

Due to these considerations it is decided to retain the current hydrodynamic description and to modify the continuum model with respect to the heat transfer in the corresponding areas. This is done by including specific “a priori”- information about the void area which are gained gain from the DEM simulations. The modifications are to account for the influence of the void zone itself in the range of $\omega_{VZ} < \omega < 180°$ (with ω_{VZ} being the angle at which the void zone begins) as well as the gradual separation of the particles from the tube surface in the range of $\omega_{sep} < \omega < \omega_{VZ}$ (with ω_{sep} being the angle at which the particles start to separate from the tube surface).

Regarding the latter, a convenient way is to modify the thermal contact resistance between the bulk and the tube surface $(\alpha_c)^{-1}$. As shown in section 4.1.2.1 (equation (18), p. 33), this resistance depends on the fraction, φ, of the tube surface which is covered by particles (see equation (19), p. 33). So far a (constant) empirical value of φ for random packed beds has been assumed which can now be substituted by a value $\varphi(\omega)$ which is to be determined from DEM simulations. For the calculation of $\varphi(\omega)$, the tube surface is subdivided in control areas. For each control area, $\varphi(\omega)$ is calculated according to equation (19) with A_W being the magnitude of the control area and N_p being the number of contacting particles in the control area. The results as shown in Figure 26.

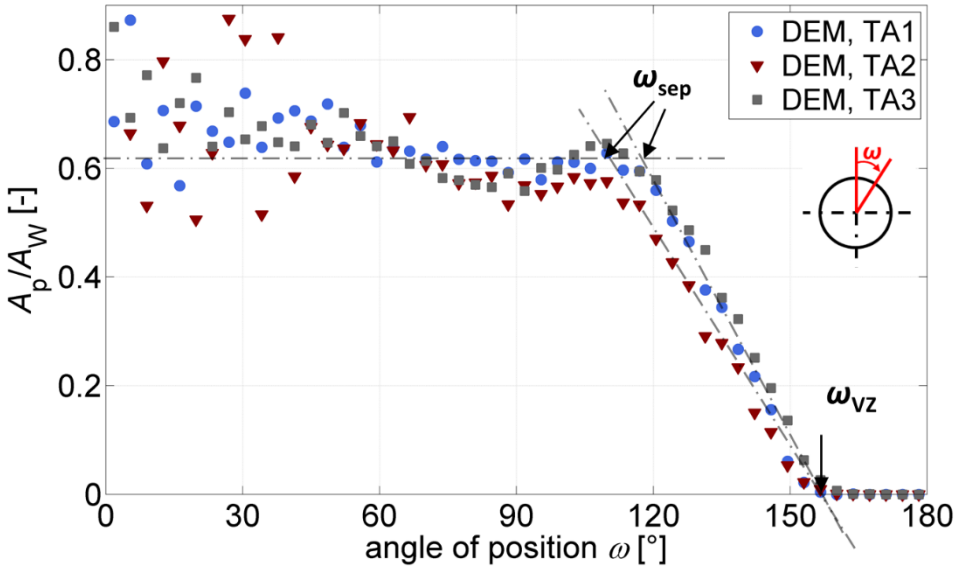

Figure 26. Local fraction of the tube surface covered by particles ($\varphi(\omega) = Ap/A_W$, see section 4.1.2.1) at different tube arrangements.

The scattering of the data at the top of the tube originates from very large time constants in this region. As the particles are moving very slowly in the static zone, if at all, averaging over very long time periods or larger control volumes would be necessary to reduce the scattering. As the main objective of the diagram is to provide information about the formation of the void area in the lower part of the tube, the left part of the diagram is of minor importance.

Based on the $\varphi(\omega)$-profile in Figure 26 a local contact resistance $(\alpha_c(\omega))^{-1}$ is calculated according to equation (18) which is then included in the temperature boundary condition at the tube wall (see section 4.1.2). The $\varphi(\omega)$-profile is approximated by a *tanh*-function as illustrated in Figure 27. The dependence of ω_{sep} and ω_{VZ} on the operating conditions, material parameters and the tube arrangement is investigated in section 6.1.2.

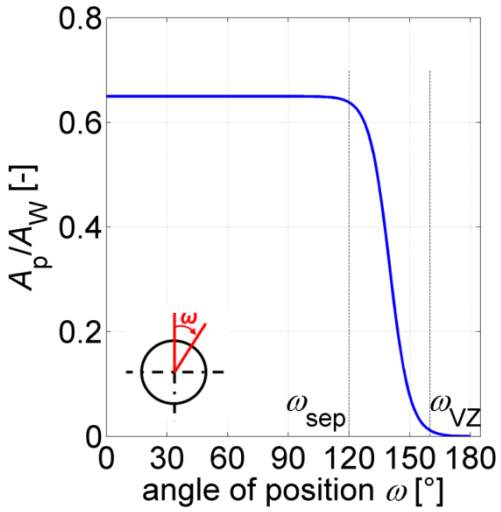

Figure 27. *tanh*-function approximating the profile of $\varphi(\omega)$ (see Figure 26).

To take into account the influence of the void zone itself, a wedge-shaped area of the size of the void zone is introduced below the tube which is confined by frictionless walls. The inclination of the flanks of this artificial void area is the angle of repose ϕ_r of the granular material (see Figure 28 (right)). The surface temperature at these flanks is defined by a Nusselt correlation which accounts for the heat transport through the cavity.

To this end a Nusselt correlation according to Churchill and Chu [112] is adopted which has already been used for the same purpose by Niegsch et al. [2] (see appendix B.1). According to this correlation the convective heat transport through the cavity, α_{conv}, is calculated at $\omega = 180°$ using the 'height', H_{VZ}, of the void zone:

$$\alpha_{conv} = \frac{\lambda_f}{H_{VZ}} \cdot Nu \tag{39}$$

In the range $\omega_{VZ} < \omega < 180°$ it is interpolated linearly between $\alpha_c(\omega = \omega_{VZ})$ and α_{conv} (see appendix B.1).

Figure 28 (left) shows the velocity profile from CFD simulations along the surface of the modified simulation geometry (solid lines). In the range of $150° < \omega < 180°$ the profile runs along the surface of the wedge-shaped zone in the lower part of the tubes (see red arrow in Figure 28 (right)). The dashed lines with symbols are the DEM simulation results along the tube surface which have already been shown in Figure 21.

The velocity profiles of the CFD model change only slightly compared to those of the unmodified geometry (see Figure 21). Slightly higher flow speeds occur in the lower part of the tube.

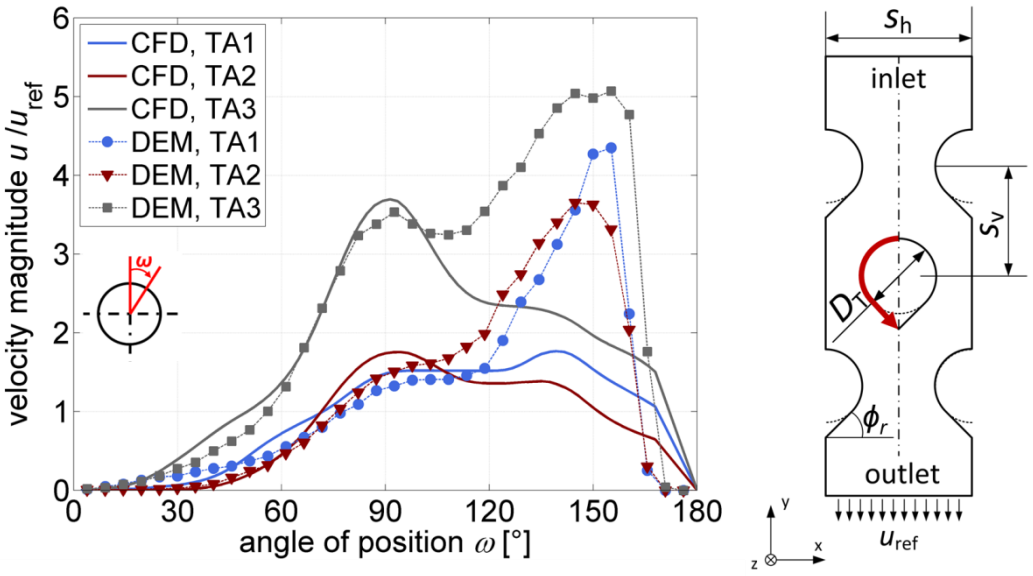

Figure 28. Right: Modified Simulation geometry. Left: Velocity magnitude along the tube surface for three different tube arrangements. Solid lines: CFD model (modified geometry). Dashed lines with symbols: DEM model (unmodified geometry).

5.2.3 Heat transfer

In this section the modified continuum model is validated based on the heat transfer coefficient between tube and bulk. The simulation results are compared to the data obtained from the experimental setup described in section 3.2, varying the tube arrangement and the grain size according to the configurations in Table 1.

The stainless steel foil, which is used in the experiment to heat the test tube exhibits a different surface friction coefficient than the bare tube. This has to be accounted for in the simulations. According to Baumann [1], who measured the surface friction coefficient of quartz sand on polished stainless steel, a value of $\mu_W = 0.25$ is set.

5.2.3.1 Local heat transfer coefficient

Figure 29 and Figure 30 (p. 64 f.) show profiles of the local heat transfer coefficient $\alpha_{loc}(\omega)$ deduced from simulation and experiment at different mass flow rates (flow speeds). Each diagram stands for one of the four configurations given in Table 1. As the

α_{loc}-profiles are symmetric around the tube, only the range of $0° < \omega \leq 180°$ is displayed. At first, only the experimental plots are discussed in the following paragraphs before the attention is turned to the juxtaposition with the simulation results.

At the tube vertex ($\omega \lesssim \omega_{SZ}$) the shape of the α_{loc}-profile is determined by the shape and size of the stagnant zone. Small values of $\alpha_{loc}(\omega \approx 0°)$ indicate a large stagnant zone hampering the heat transfer. Furthermore, in case of a large stagnant zone the dependence of $\alpha_{loc}(\omega \approx 0°)$ on the mass flow rate is expected to be small as heat transfer is dominated by conductive transport through the stagnating medium. According to these considerations, the experimental α_{loc}-profiles of TA2 indicate a large stagnating area which is in accordance with the simulation results (see contour plots on the right of Figure 29 and Figure 30). The profiles of TA1 and TA3 indicate smaller stagnant areas of similar orders of magnitude. This again is in accordance with the simulation results.

The grain size shows minor influence on $\alpha_{loc}(\omega \approx 0°)$ as is visible from the comparison of TA3 ($d_p = 0.6$ mm) and TA3 ($d_p = 1.2$ mm). This is to be expected as the grain size has minor impact on the thermal conductivity of the bulk which governs the conductive transport through the stagnant area.

At the lateral sides of the tubes all of the experimental plots show a maximum $\alpha_{loc,max}$ around $\omega = 90°$. The magnitude of $\alpha_{loc,max}$ significantly depends on the mass flow rate; higher values are reached at increased mass flow rates (flow speeds). However, the influence of the mass flow rate diminishes at higher flow speeds. Furthermore, significantly lower magnitudes of $\alpha_{loc,max}$ are reached in the case of a larger grain size**.**

These two effects, the influence of the mass flow rate and the grain size, are both linked to the thermal contact resistance $(\alpha_c)^{-1}$ at the tube surface (see section 4.1.2). The contact resistance constitutes an upper limit to the heat transfer coefficient. This limiting effect is most noticeable at the point where α_{loc} reaches its maximum, which is at the lateral sides of the tubes and at high mass flow rates. Furthermore, larger particles exhibit higher contact resistances (see section 4.1.2.1) which leads to lower values of $\alpha_{loc,max}$ at larger grain sizes.

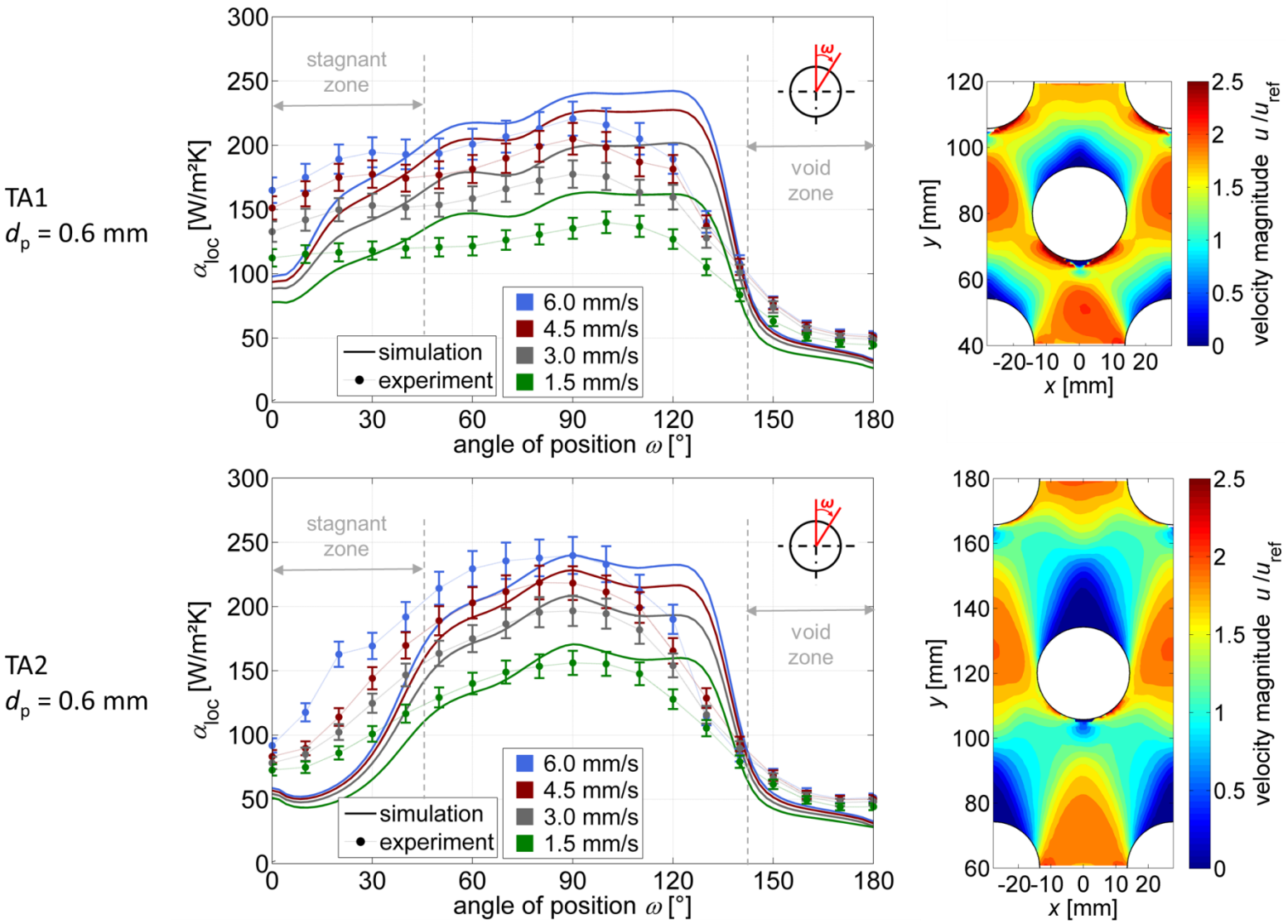

Figure 29. Local heat transfer coefficient along the tube surface at different tube arrangements and grain sizes (Diagrams (a)-(d)). In each diagram: Solid lines with symbol: Experimental data. Dashed lines: Simulation data. Different colors denote different mass flow rates.

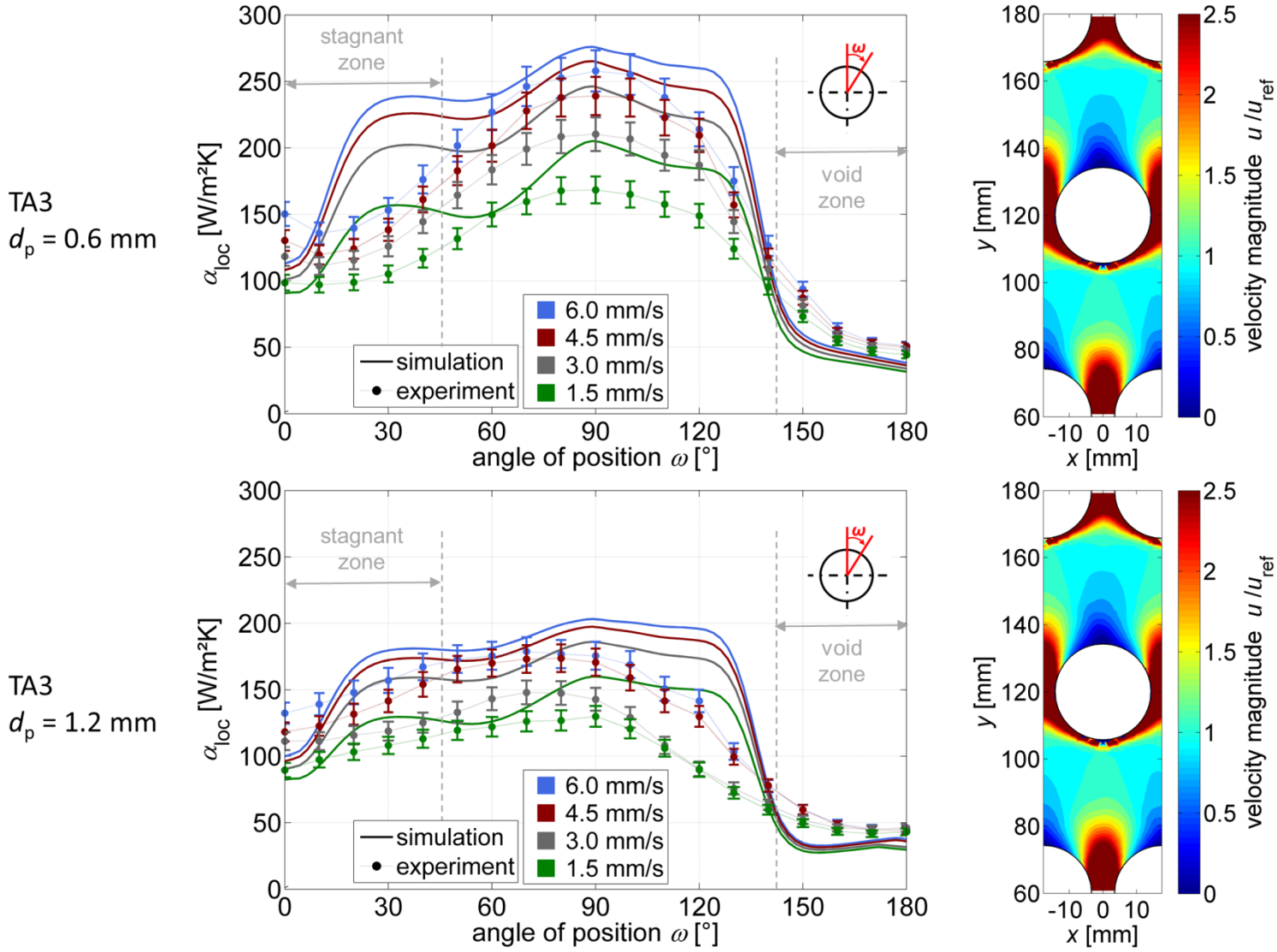

Figure 30. Local heat transfer coefficient along the tube surface at different tube arrangements and grain sizes (Diagrams (a)-(d)). In each diagram: Solid lines with symbol: Experimental data. Dashed lines: Simulation data. Different colors denote different mass flow rates.

The tube arrangement shows a moderate influence on the magnitude of $\alpha_{loc,max}$ which is based on its influence on the residence time of the bulk at the tube surface. A narrow arrangement, especially a small horizontal tube spacing s_H, leads to high flow speeds (see Figure 21) and a low residence time which results in a higher heat transfer coefficient (see section 2.2).

Furthermore, the tube arrangement influences the size of the stagnant area (see section 6.1.1 for more details). The size of the stagnant area in turn influences the amount of heat transferred in the upper part of the tube. As the heat transfer process along the tube surface is a transient process, the magnitude of the heat transfer rate at the top of the tube affects α_{loc} downstream at the lateral sides of the tube.

This is best illustrated comparing TA1 and TA2 which exhibit the same horizontal spacing s_H (approximately the same residence time) but different sizes of the stagnant zone. TA1 (small stagnant zone) shows significantly higher values of α_{loc} at the top of the tube than TA2 (large stagnant zone). At the lateral sides, however, TA1 shows smaller values of $\alpha_{loc,max}$ than TA2. This is due to the fact that at the lateral sides the driving temperature gradient inside the bulk is smaller in case of TA1 as more heat has already been transferred upstream in the stagnant zone.

This means that a gain of heat transfer rate at the top of the tube – by reducing the size of the stagnant area – is partly equalized by a reduction of the heat transfer rate at the side of the tube.

Below the tube where the void area is found, α_{loc} takes a minimum value of $\alpha_{loc,min} \approx 50$ W/m²K, which is approximately independent of the geometry and the grain size. This indicates that the size and extend of the void area remains constant in the investigated cases which is in accordance with the DEM simulation results (see Figure 26).

So far, only the experimental α_{loc}-profiles have been discussed. In the following paragraphs they are now juxtaposed to the simulation results and interpret the deviations between simulation and experiment.

In the void area ($\omega \gtrsim 160°$), the model yields a uniform α_{loc} below the tube of $\alpha_{loc,min} \approx 40$ W/m²K which is slightly smaller than the experimental value. So, the Nusselt-correlation used to account for the heat transfer through the void space seems to slightly underestimate the heat transfer rate. In accordance with the experiment, the heat

transfer rate in the void area is approximately independent of the tube arrangement and the grain size.

In the range of $130° \lesssim \omega \lesssim 160°$ the calculated α_{loc} profiles decline. This is the range where the model has been modified by adapting the thermal contact resistance at the tube surface (see section 5.2.2). The measured profiles in contrast, decrease more continuously in the range of $100° \lesssim \omega \lesssim 160°$. The deviations originate from the fact that the packing fraction near the wall changes significantly in this range (see section 5.1.1), which is not explicitly taken into account in the continuum-model.

At the lateral sides of the tube the model yields maximum values of α_{loc} at $\omega \approx 90°$ except for TA1 where a plateau of $\alpha_{loc,max}$ occurs in the range of $90° < \omega < 120°$. Generally, the magnitude of α_{loc} is of the same order as in the experiment.

In agreement with the measurement, $\alpha_{loc,max}$ increases regressively with the mass flow rate. Furthermore, in agreement with the measurement, the model yields much smaller heat transfer rates for the larger grain size (see Figure 30). The reasons for this behavior have already been discussed above.

In the stagnating zone deviations between simulation and experiment occur which do not follow a common pattern. While in TA1 and TA2 the model underestimates the heat transfer coefficient, in TA3 it overestimates it, especially for $d_p = 0.6$ mm.

Generally, it can be said that small deviations regarding the very small flow speed in the stagnant area entail significant deviations regarding the local heat transfer rate. For example, if there is slight particle movement inside the stagnant area instead of an actually resting bulk, the heat transfer rate increases significantly.

This behavior is illustrated in the following paragraphs where the deviations in the realm of the stagnant zone are discussed for each tube arrangement based on the velocity profiles of the CFD- and DEM model at the tube surface (Figure 21 (p. 54) in section 5.2.1).

In case of TA1, particle motion is already observed at the top of the tube ($\omega < 30°$) in the DEM simulation, whereas the CFD model yields a resting bulk. Due to this small but noticeable movement inside the stagnant area, heat transfer is not governed by conduction alone but also by a convective component which is not captured by the CFD model. This explains why the CFD model underestimates the heat transfer in the stag-

nant zone and why the experimental data shows a pronounced dependence on the mass flow rate.

In case of TA2, CFD and DEM yield very similar velocity profiles along the tube surface. Still, the simulated α_{loc} profile yields a "dent" in the range of $\omega \lesssim 30°$, which is not visible in the experiment. This effect results from a circulating motion of the gas-phase inside the stagnant zone (see Figure 31). The effect occurs only in TA2, but not in TA1 and TA3. The reason for this is that TA2 exhibits a much larger stagnant zone wherein the gas phase may circulate. Outside the stagnant area the flow direction of the gas phase is imposed by the motion of the solid phase.

Although the measurement data doesn´t support the occurrence of natural convection effects of the fluid phase in the considered case, the simulation results indicate that such effects should not be neglected with respect to the heat transfer process.

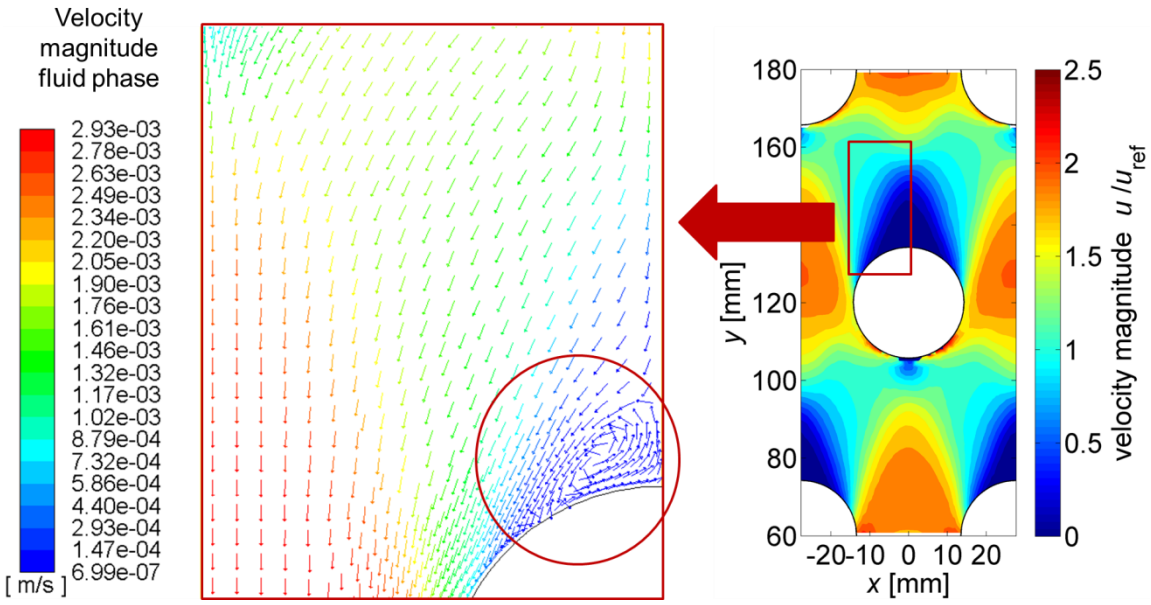

Figure 31. Left: Vector plot of *gas phase* above the tube colored by velocity magnitude (uniform vector size). Right: Contour of velocity magnitude of granular phase.

In case of TA3, the velocity profile at the tube surface obtained from CFD clearly exceeds that of the DEM in the range of $20° \lesssim \omega \lesssim 40°$. In the same range the simulated α_{loc} profile rises strongly and exceeds the measured profile.

The analysis of the local heat transfer can be summarized as follows: The model well captures the dependence of $\alpha_{loc}(\omega)$ on the mass flow rate and on the particle size.

In the stagnant zone ($0° \leq \omega < 60°$), maximum deviations between simulation and experiment of 60 % occur ($|\Delta\alpha_{loc}|/\alpha_{loc,exp} \approx 0.6$). They can be traced back to deviations of the granular flow field in this area, as is visible from a comparison with the DEM results. It is shown that small variations of the particle motion in the stagnant zone show significant impact on the $\alpha_{loc}(\omega)$ profile.

At the lateral sides of the tube ($60° \leq \omega < 120°$), maximum deviations of 30 % occur ($|\Delta\alpha_{loc}|/\alpha_{loc,exp} \approx 0.3$).

Around the lower part of the tube where the particles gradually separate from the tube surface ($120° \leq \omega < 160°$), the model tends to overestimate the heat transfer and locally maximum deviations of 60 to 100 % occur (especially at $\omega = 130°$). These deviations are attributed to the fact that the continuum model does not capture the decrease of the packing fraction near the tube surface in this area (see section 5.1.1).

In the void zone below the tube ($160° \leq \omega < 180°$), the deviations between simulation and experiment are about 20 to 40 % for all investigated geometries.

5.2.3.2 Averaged heat transfer coefficient per tube

Simplified design calculations are based on an averaged heat transfer coefficient per tube. It is obtained by integrating the local heat transfer coefficient, $\alpha_{loc}(\omega)$, over the whole circumference of the tube:

$$\alpha_{av} = \frac{1}{180°} \int_0^{180°} \alpha_{loc} d\omega \tag{40}$$

For every case investigated in the previous section, Figure 32 shows α_{av} as a function of the inlet velocity.

The averaged heat transfer coefficient increases regressively with the inlet velocity both in the simulation and in the experiment. In case of TA1 and TA2 the simulation results deviate by less than 6 % from the experimental data. In case of TA3 the model overestimates the experimental data both for fine and coarse particles with a maximum deviation of 20 %. The relative deviations between simulation and experiment for each configuration are given in Table 3.

The particle size in contrast shows great impact on α_{av} (Table 3). Due to the larger particle size, the value of α_{av} decreases by approximately 20 % in TA3. The reason for this is

found in the increased thermal contact resistance and has been discussed in the preceding section.

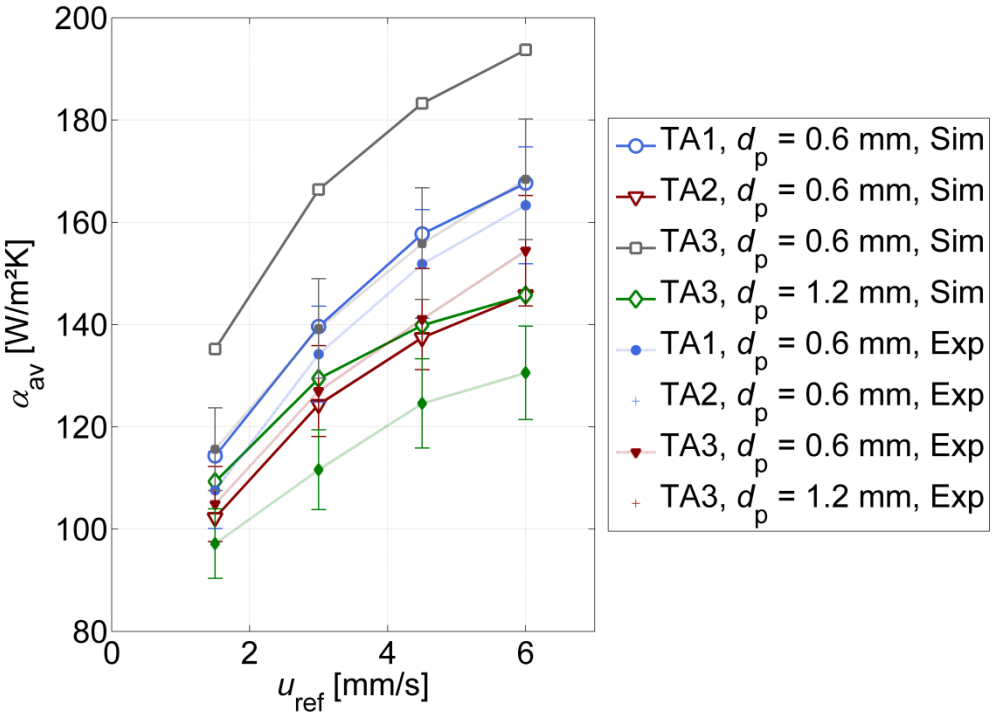

Figure 32. Averaged heat transfer coefficient α_{av} as a function of the inlet velocity.

Table 3. Relative deviations between simulation and experiment regarding the averaged heat transfer coefficient (right column). Influence of the tube arrangement on the averaged heat transfer coefficient (only experimental data, left column).

Configuration	$\frac{\Delta\alpha_{Exp,TAi}}{\alpha_{Exp,TA2}}$	$\frac{\alpha_{Sim}-\alpha_{Exp}}{\alpha_{Exp}}$
TA2, d_p = 0.6 mm	0 %	- 6 %
TA1, d_p = 0.6 mm	+ 6 %	+ 6 %
TA3, d_p = 0.6 mm	+ 10 %	+ 20 %
TA3, d_p = 1.2 mm	- 10 %	+ 16 %

5.2.4 Summarizing conclusions on the model quality

Summarizing, the CFD model has been validated on the basis of three different tube arrangements. The calculated, isothermal flow field in these three geometries has been compared to the results of the DEM model. Special focus has been given to the velocity profile at the tube surface

In the upper half and at the side of the tube ($0° < \omega \lesssim 110°$) both models agree well regarding the packing fraction and the size and shape of the stagnant area. The velocity profile at the tube surface agrees within a deviation of $|\Delta u/u_{ref}| < 0.4$. Thus, the CFD model is considered reliable within this accuracy limit.

In the lower part of the tube, the CFD model yields only a slight decrease in packing fraction whereas the DEM model captures the formation of the void area. Thus, the volume under the tube is treated through inserting a solid cone-shaped area. The heat transfer rate in this area is calculated according to a Nusselt correlation which is translated to the corresponding surface temperature of the cone-shaped area. Size and extent of the void zone is obtained from the DEM results. Additionally, the thermal contact resistance at the tube wall is modified to account for the fact that the number of particles in touch with the wall gradually decreases below the tube.

The modified CFD model is subsequently used to calculate the local heat transfer coefficient, $\alpha_{loc}(\omega)$, at the tube surface for the three investigated tube arrangements at different mass flow rates. Additionally, for one tube arrangement the effects of a larger grain size are investigated. The results are compared to experimental data.

The model well captures the dependence of $\alpha_{loc}(\omega)$ on the mass flow rate and on the particle size. Deviations primarily occur in the stagnant zone which can be traced back to deviations of the granular flow field in this area, as is visible from a comparison with the DEM results. It is shown that small variations of the particle motion in the stagnant zone show significant impact on the $\alpha_{loc}(\omega)$ profile.

From the $\alpha_{loc}(\omega)$ profiles the average heat transfer coefficient per tube, $\alpha_{av}(u_{ref})$, is calculated as a function of the mass flow rate, the tube arrangement and the particle size. The model deviates by less than 20 % from the experiment and well captures the dependence on the mass flow rate and the particle size.

6 Simplified model of heat transfer at a single tube

As seen in section 5.2.3, the heat transfer rate between tube and bulk is governed by the granular flow field around the tube. The relevant flow field can be divided into three characteristic sections: a stagnant area at the top of the tube, a sliding area at the lateral sides of the tube and a void area below the tube.

In the following section the local extents of these sections are quantified depending on the relevant influencing parameters. The aim is to establish the basis for a simplified description of the heat transfer between tube and bulk. Such a simplified model is discussed in the sections 6.2 to 6.4.

6.1 Local extent of the characteristic flow sections

To identify the determinants of dimensions of the flow field, several parameter variations are performed using the DEM model. For every simulation the flow sections are quantified by estimating the following quantities (see Figure 42, p. 90):

- The height H_{SZ} and the angular extent ω_{SZ} of the stagnant area.
- The angular extent of the void area (ω_{sep}, ω_{VZ}).

These four quantities are determined from the following three types of diagrams:

Firstly, the velocity profile along the tube surface (see Figure 21, p. 54), from which the extent of the stagnant area (ω_{SZ}) is estimated; secondly, the velocity profile along the vertical center line above the tube (see Figure 24, p. 57) from which the height of the stagnant zone H_{SZ} is estimated; and thirdly, the local share of the tube surface covered by particles $\varphi(\omega)$ (see Figure 26, p. 60) from which the quantities ω_{sep} and ω_{VZ} are estimated.

The varied parameters are given in Table 4 with the reference value of each parameter in bold print. The remaining model parameters are given in Table 2 (p. 39).

Table 4. Simulation parameters subject to variation. Bold figures are reference values.

Parameter	Symbol	Unit	Range
Horizontal spacing of the tubes	s_H	mm	{37, 47, **57**, 67, 77}
Vertical spacing of the tubes	s_V	mm	{32, 40, 45, **50**, 55, 60, 75}
Wall friction coefficient	μ_W	-	{0.2, 0.3, **0.4**, 0.5}
Angle of internal friction	ϕ_i	°	{29, **34,** 41}

The range of the friction parameters ϕ_i and μ_W in Table 4 are chosen according to the measurement results given by Baumann [1] who examined a wide range of practically relevant materials.

The three values of the inner friction angle[6], ϕ_i, in Table 4 correspond to three materials which are potential candidates for the application as a heat transfer medium in solar thermal power plants: bauxite proppants ($\phi_i \approx 29°$), quartz sand ($\phi_i \approx 34°$) and basalt ($\phi_i \approx 41°$).

The inner friction angle is not a parameter of the DEM model by itself. Instead it is determined by the internal friction coefficients μ_{pp} and μ_{roll} which have to be calibrated. For quartz sand the calibration procedure is described in section 4.3.2 which is based on literature data of the friction coefficient μ_{pp}. However, for bauxite and basalt no literature data of μ_{pp} could be found. Therefore, for bauxite the value of μ_{pp} is assumed to be in the same range like for quartz sand ($\mu_{pp} = 0.2$) which leads to $\mu_{roll} = 0.2$.

For basalt a higher value of μ_{pp} has to be set to attain the desired friction angle $\phi_i = 41°$. The smallest possible value of μ_{pp} is $\mu_{pp} = 0.3$ which leads to $\mu_{roll} = 0.4$. This of course is only a very rough estimate of the values of μ_{pp} and μ_{roll}. A more precise calibration requires a much more complex experimental procedure (see [106]). However, as shown in appendix C.3, the magnitude of the quantities H_{SZ}, ω_{SZ}, ω_{sep} and ω_{VZ} is relatively insen-

[6] The inner friction angle is approximately equal to the angle of repose $\phi_i \approx \phi_r$

sitive to the choice of μ_{pp} and μ_{roll} as long as the correct inner friction angle (angle of repose) is retained.

Regarding the tube arrangement, both horizontal and vertical spacing (s_H, s_V) is varied simultaneously (not only at the reference value of the fixed parameter). The minimum values of s_H and s_V are chosen such that the minimum distance between the tubes is ten particle diameters in the simulation.

6.1.1 Stagnant area

In this section the dependence of the magnitude of the stagnant zone, characterized by ω_{SZ} and H_{SZ}, on the parameters in Table 4 is considered. For every set of parameters the two quantities are determined by inserting a tangent to the profiles of the flow velocity along the tube surface and along the vertical section above the tube (see Figure 21 (p. 54) and Figure 24 (p. 57)).

However, as evident from Figure 21 and Figure 24, no distinct boundary of the stagnant zone is observed but rather a continuous transition from the static to the flowing regime. Hence, ω_{SZ} and H_{SZ} are only virtual quantities for an approximate description of the magnitude of the stagnant zone.

The shape of the stagnant zone can be well approximated by a parabola (with the coordinate origin in the center of the tube):

$$y = ax^2 + y_{max}\,, \tag{41}$$

with the parameters y_{max} and a:

$$y_{max} = H_{SZ} + \frac{D_T}{2} \tag{42}$$

$$a = \frac{\frac{D_T}{2}\cos(\omega_{SZ}) - y_{max}}{\frac{D_T}{2}\sin^2(\omega_{SZ})} \tag{43}$$

Figure 33 shows a contour plot of the velocity magnitude of the granular flow obtained from the DEM model (s_H = 57 mm, s_V = 50 mm). The parabola calculated according to equation (41) to (43) is marked as a white curve above the tube.

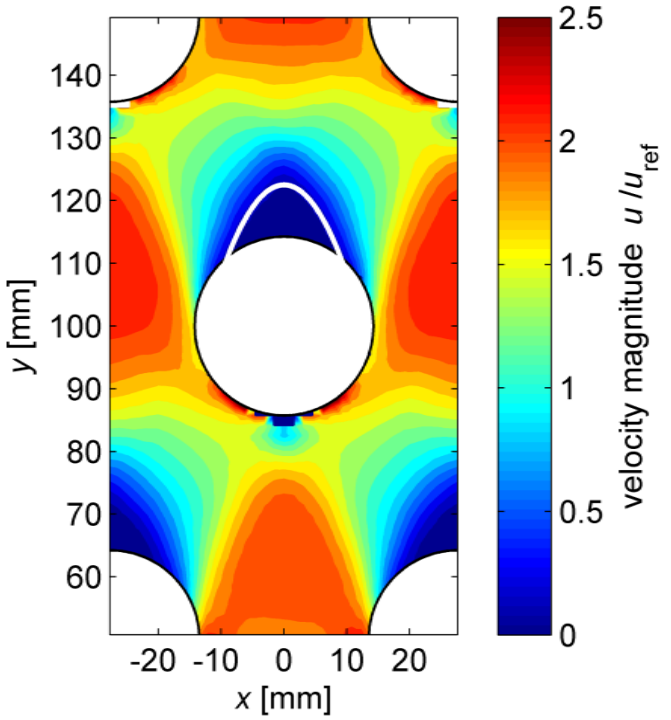

Figure 33. Contour plot of velocity magnitude from DEM simulation (reference geometry). The white parabolic curve at the tube vertex approximates the stagnant zone.

Impact of the friction parameters:

The variation of the friction parameters ϕ_i and μ_W yields the following results: Within the investigated boundaries the inner friction angle ϕ_i shows no significant influence both on ω_{SZ} and H_{SZ}.

The impact of the wall friction coefficient, μ_W, on the size of the stagnant area is illustrated in Figure 34. μ_W primarily influences the extent of the stagnant area ω_{SZ} which shows an approximately linear dependence and takes values in the range of $30° < \omega_{SZ} < 50°$. The impact of μ_W on H_{SZ} is small and $H_{SZ} \approx 9$ mm ($0.33 \cdot D_T$) is found for all investigated cases.

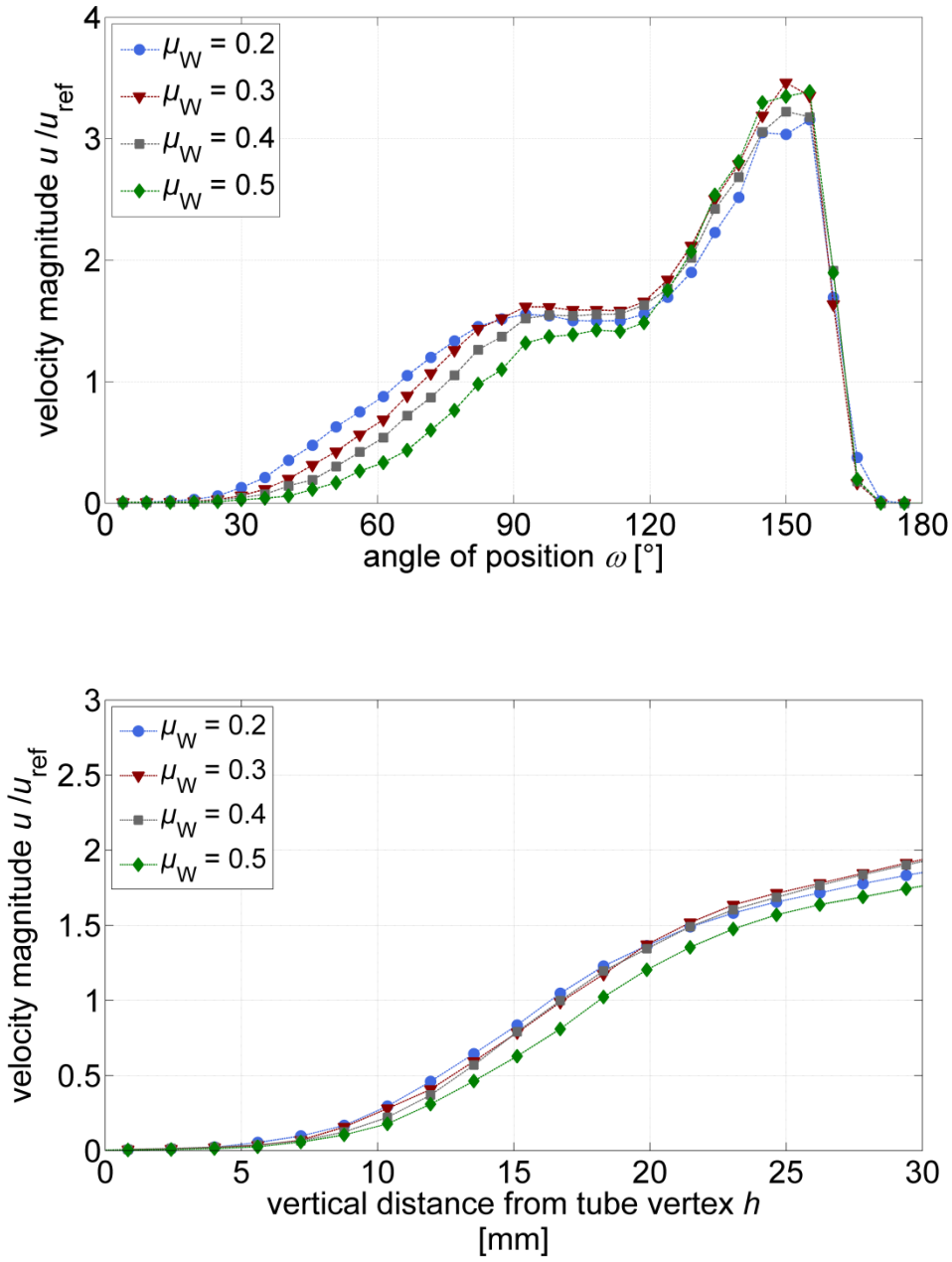

Figure 34. Influence of the wall friction coefficient μ_W of the tubes on the size of the stagnant zone.

Impact of the tube arrangement:

The variation of the tube arrangement (s_H, s_V) yields a more complex influence on the magnitude of the stagnant area. Figure 35 shows contours of $H_{SZ}(s_H, s_V)$.

At given horizontal pitch s_H, the height H_{SZ} increases with the vertical pitch s_V until a maximum height $H_{SZ,max}(s_H)$ is reached (see the dashed line in Figure 35). If s_V is increased even further, H_{SZ} decreases rapidly until it reaches a constant value of

$H_{SZ}/D_T \approx 0.1$ (see top left corner of Figure 35). The flow field then resembles that of an undisturbed single tube.

The horizontal spacing of the tubes, s_H, shows minor influence on the height of the stagnant zone, especially at small and intermediate vertical spacings (area below the dashed line in Figure 35). At large vertical spacings (area above the dashed line in Figure 35), the stagnant area increases with the horizontal spacing. The maximum obtainable height, $H_{SZ,max}$, shows an increasing tendency with the horizontal spacing.

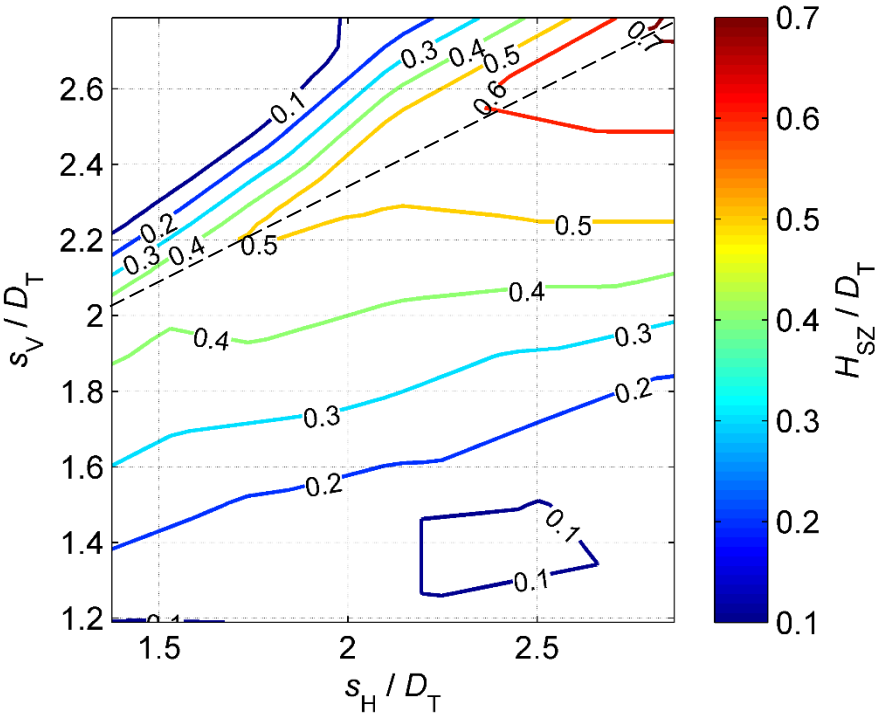

Figure 35. Contour of the height of the stagnant zone H_{SZ} as a function of vertical and horizontal spacing of tubes (s_V and s_H).

The fact that the vertical size (height) of the static area can be influenced by the tube arrangement is one of the important outcomes of this work. In contrast to that, Niegsch [2] assumed the stagnant zone to be dependent only on the internal friction properties of the granular material. The simulation results, however, show that the stagnant zone is primarily defined by the flow geometry. The geometry determines the general flow path and also implies areas of increased shear movement (see Figure 36). The stagnant areas establish themselves along these shear zones.

The continuum model includes this behavior by the granular viscosity μ_{fr} which is proportional to the inverse of the Euclidian norm of the strain rate ($\mu_{fr} \sim 1/|\boldsymbol{S}_s|$ in equation (15), p. 31). Hence, in areas of increased strain-rate (increased shear rate) – which depend on the flow geometry – the granular viscosity decreases, which in turn leads to an intensification of the shear movement. This results in a dependence of the size of the stagnant area on the tube arrangement (the flow geometry), especially on the vertical tube spacing s_V, as illustrated in Figure 36.

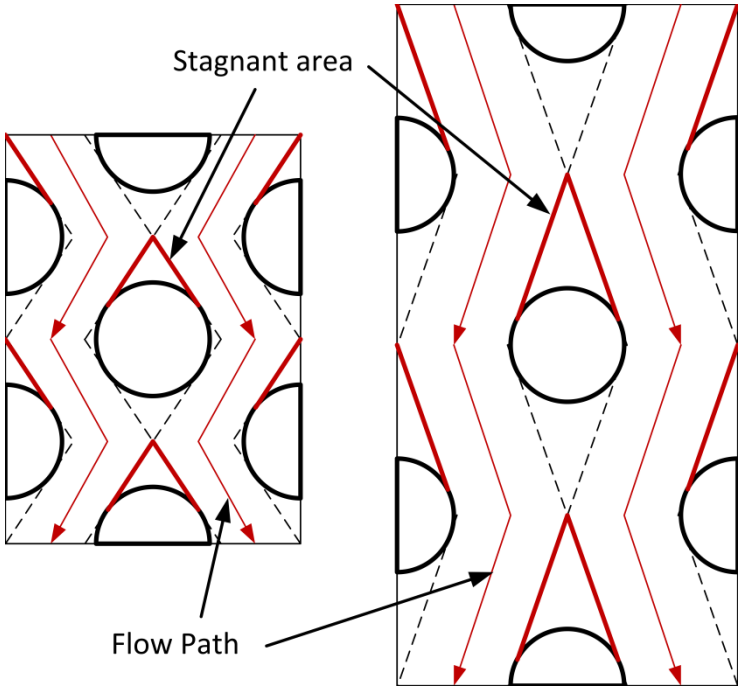

Figure 36. Schematic of flow path around horizontal tubes. The size of the stagnant areas changes with the vertical spacing between the tubes.

The angular extent of the stagnant area ω_{SZ} remains virtually unaffected in most of the investigated tube arrangements. For vertical pitches, s_V, greater than $1.5 \cdot D_T$, a value of $\omega_{SZ} \approx 45°$ is obtained. However, for very small vertical spacings ($s_V/D_T < 1.5$) a significant reduction of ω_{SZ} is observed (see Figure 37). At the smallest investigated vertical pitch ($s_V/D_T = 1.19$) the extent of the stagnant area is $\omega_{SZ} \approx 12°$. According to these results the following simple correlation for the extent of the stagnant zone ω_{SZ} can be given:

$$\omega_{SZ} = \begin{cases} \omega_{SZ,max} & \text{for } \dfrac{s_V}{D_T} > 1.5 \\ \dfrac{\omega_{SZ,max} - 12°}{0.3} \dfrac{s_V}{D_T} + 60° - 4\omega_{SZ,max} & \text{for } \dfrac{s_V}{D_T} < 1.5 \end{cases} \tag{44}$$

with $\omega_{SZ,max}$ depending linearly on μ_W (see Figure 34):

$$\omega_{max}(\mu_W) = 67° \cdot \mu_W + 17° \tag{45}$$

The correlations (44) and (45) are valid only inside the tested parameter ranges ($1.2 \leq s_V/D_T \leq 2.8$ and $1.4 \leq s_H/D_T \leq 2.9$).

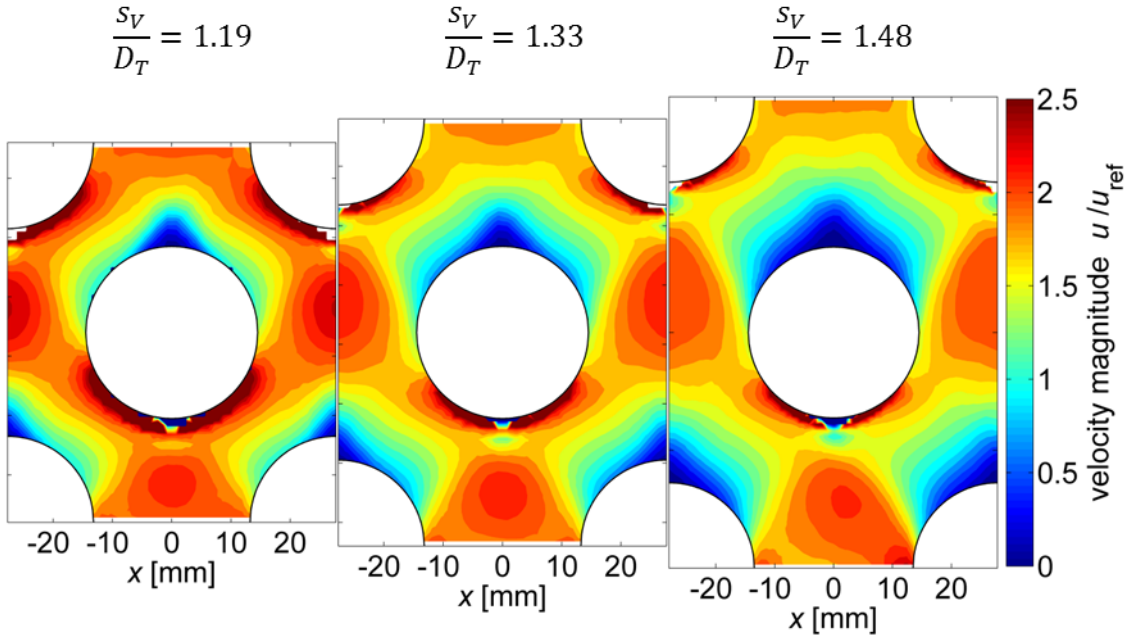

Figure 37. Contours of velocity magnitude at small vertical tube spacing $s_V/D_T < 1.5$. The size and especially the extent of the stagnant zone reduce significantly with the vertical spacing.

6.1.2 Void area

As shown in section 5.2.2, the void area below the tubes is characterized by the two angles ω_{sep} and ω_{VZ}. At ω_{sep} the particles start to separate from the tube surface and at ω_{VZ} the actual void zone starts. The two angles are estimated from the profile of the parameter $\varphi(\omega)$, the local fraction of the tube surface covered by particles (see Figure 26, p. 60).

In section 5.2.1 it has been shown that the void area is of triangular shape (Figure 20, p. 53) with the slops inclined by the angle of repose, ϕ_r, to the horizontal. Furthermore, if the slopes of the void zone are tangential to the tube surface, the height and the extent of the (actual) void zone are defined and consequently should be insensitive to the re-

maining parameters. This assumption is to be verified by the results shown in this section.

Impact of the friction parameters:

Figure 38 shows the profiles of $\varphi(\omega)$[7] at varying friction parameters μ_W and ϕ_i.

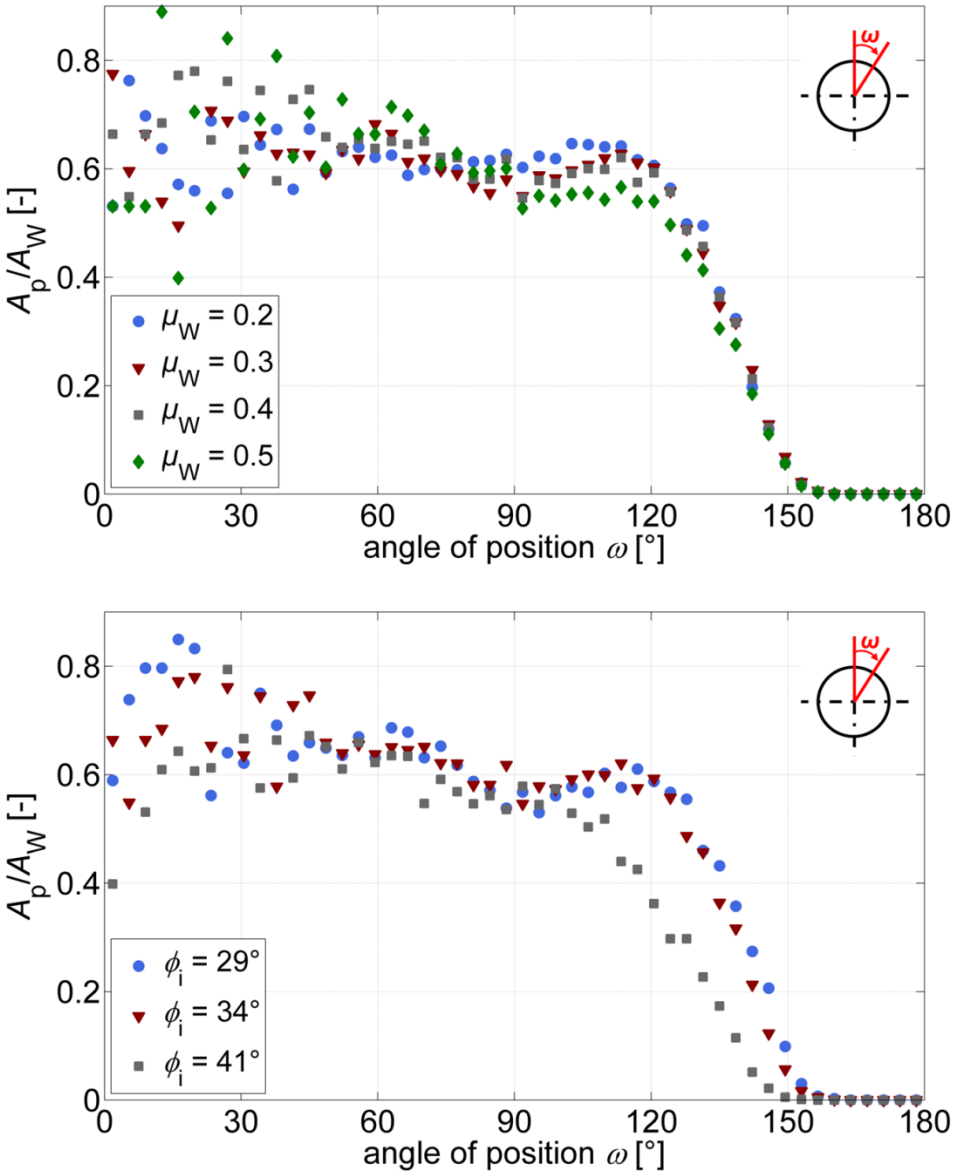

Figure 38. Share of tube surface covered by contacting particles $\varphi(\omega) = A_p/A_w$ at different wall friction coefficients μ_W (top) and inner friction angles of the bulk ϕ_i (bottom).

The wall friction coefficient, μ_W, shows little influence on the formation of the void area (Figure 38 (top)), yielding uniform values of $\omega_{VZ} \approx 150°$ and $\omega_{sep} \approx 120°$. This is in ac-

[7] $\varphi(\omega) = A_p/A_w$ is the fraction of the wall surface covered by contacting particles (see equation (19), p.32)

cordance with the assumption regarding the shape and size of the void zone stated above, which implies $\omega_{VZ} = 180° - \phi_r = 146°$ for quartz sand ($\phi_r = 34°$).

Figure 38 (bottom) shows the profiles of $\varphi(\omega)$ at different angles of internal friction ϕ_i. Here, a slight dependence of ω_{VZ} on ϕ_i ($\approx \phi_r$) is found. For increased internal friction ($\phi_i = 41°$), the angular coverage of the void zone increases ($\omega_{VZ} \approx 140°$) which again is in agreement with $\omega_{VZ} = 180° - \phi_r = 139°$.

Likewise, ω_{sep} also tends to take lower values when ϕ_i is increased. Therefore, the conclusion is drawn that materials with a small angle of internal friction are preferable as they are expected to separate later from the tube surface and thus are expected to yield higher heat transfer rates in the lower part of the tube.

Impact of the tube arrangement:

The influence of the tube arrangement (horizontal and vertical pitch, s_H and s_V) on the extent of the void zone is very small and $\omega_{VZ} \approx 150°$ is found for nearly all cases. Only for very small horizontal spacings ω_{VZ} increases slightly and approaches $\omega_{VZ} = 160°$ (see appendix D.2). In contrast to that, ω_{sep} shows a more pronounced dependence on the tube arrangement. Figure 39 shows contours of $\omega_{sep}(s_H, s_V)$.

ω_{sep} takes values between 100° and 130° where smaller values are found at larger tube spacings. A single tube exhibits $\omega_{sep} \approx 90°$. So, in narrow tube arrangements, the particles tend to separate later (at larger values of ω_{sep}) from the tube surface than in wide arrangements. An explanation for this behavior is that in a narrow arrangement the particles in the lower part of the tube are forced towards the tube surface by the subsequent row of tubes.

However, a reversed tendency is found at very small vertical tube spacings ($s_V/D_T < 1.5$) where ω_{sep} decreases with reducing s_v. This is exactly the regime where a significant reduction of the extent of the stagnant area ω_{SZ} is observed (see section 6.1.1 and Figure 37, the three cases shown in Figure 37 are marked in Figure 39 by three black dots). This reduction of the size and the extent of the stagnant area leads to a smaller impact on the preceding row of tubes. As a consequence, the particles tend to detach earlier from the tube wall (at smaller values of ω_{sep}).

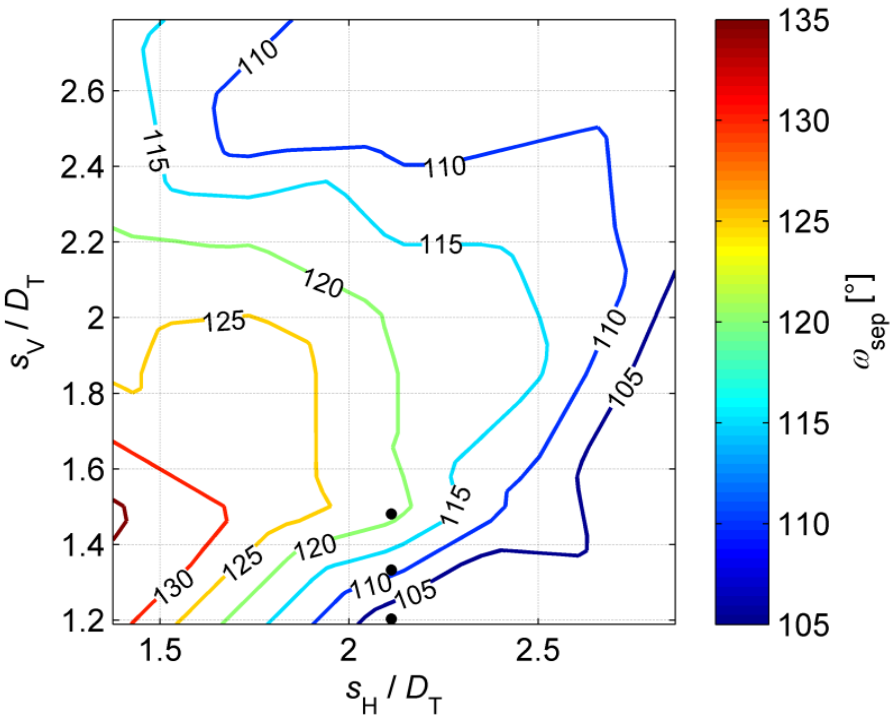

Figure 39. Impact of the tube arrangement (s_V, s_H) on ω_{sep} (angle at which the particles start to separate from the tube surface).

6.1.3 Summarizing conclusions about the extent of the characteristic flow sections

The sensitivity diagrams in Figure 40 give an overview on the results of the parameter variations which can be concluded as follows:

The tube arrangement shows major impact on the stagnant zone. The height of the stagnant zone (H_{SZ}) primarily depends on the vertical spacing of the tubes (Figure 40, left). Furthermore, at very small vertical spacings also the extent of the stagnant area (ω_{SZ}) decreases significantly (Figure 40, middle). Compared to that, the surface friction coefficient (μ_W) between tube wall and granular material shows moderate influence on the angular coverage of the stagnant zone (ω_{SZ}) while the height of the stagnant zone (H_{SZ}) remains unaffected. The variation of the inner friction angle (ϕ_i) of the granular material neither influences the vertical size nor the extent of the stagnant area.

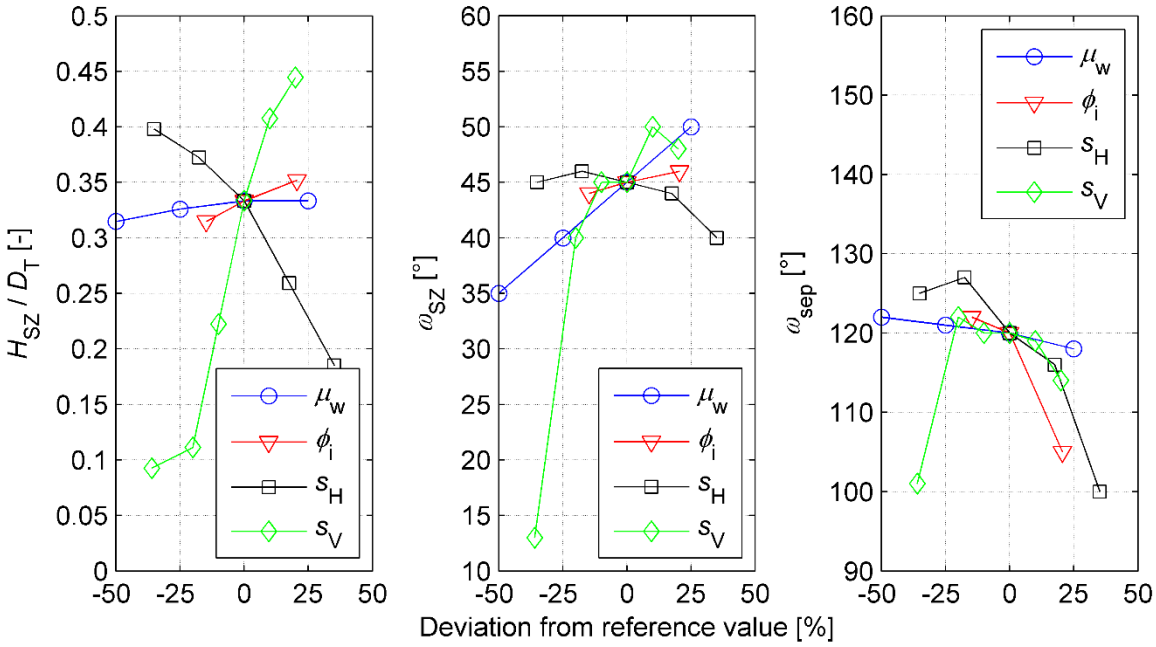

Figure 40. Sensitivity of the size of the stagnant zone (H_{SZ}, ω_{SZ}) and the position of ω_{sep} (onset of particles separating from the tube surface) with respect to the surface friction coefficient (μ_W), the angle of internal friction of the bulk material (ϕ_i) and the vertical and horizontal spacing of the tubes (s_V and s_H). The reference values of μ_W, ϕ_i, s_V and s_H are given in Table 4 (p.73).

The angular coverage of the void area (ω_{VZ}, not in Figure 40) below the tube turns out to be independent both on the tube arrangement and on the friction parameters, except to a slight influence of the inner friction angle (ϕ_i). What can be influenced, is the angle at which the particles start to separate from the tube surface (ω_{sep}). Here, again the tube arrangement is of importance. At narrow arrangements, the particles tend to separate later from the tube surface (at increased values of ω_{sep}). At very small vertical spacings a reversed trend is observed (see Figure 40, right) which diminishes at reduced horizontal spacings (see Figure 39 and comments in section 6.1.2). Materials with small inner friction angles tend to separate later from the tube surface (at increased values of ω_{sep}) while the surface friction coefficient shows no impact on ω_{sep}.

The dependencies of the stagnant and the void area have been quantified in the form of contour plots (Figure 35 and Figure 39) and in the form of simple correlations (equation (44) and (45)). They will be used as input for a simplified model of the heat transfer process in the subsequent sections.

6.2 The model of Niegsch

In this section an existing simplified model from literature is introduced which has been developed by Niegsch [86] [2]. It accounts for the heat transfer process between a horizontal tube and a flowing granular material. Subsequently, enhanced version of the model is proposed which includes the findings from section 6.1.

The model of Niegsch is based on a sectional description of the heat transfer at the tube. According to the flow pattern he defines three sections: section I (stagnant area), section II (slide area) and section III (void area). For each section the heat transfer coefficient is modeled by a series connection of thermal resistances.

To evaluate the thermal resistances Niegsch makes several assumptions about the granular flow field:

The size and the extent of the stagnant area are estimated based on the inner friction angle of the bulk as well as the surface friction coefficient between bulk material and tube surface. According to these considerations Niegsch estimates $\omega_{SZ} \approx 60°$ and $H_{SZ}/D_T \approx 0.55$ for typical friction parameters. Furthermore, it is assumed that the stagnant area is of triangular shape with distinct internal slip planes separating resting from moving particles.

The extent of the void area is estimated according to the angle of repose of the bulk. According to this, the void zone typically starts at $\omega_{VZ} \approx 150°$.

Furthermore, Niegsch assumes that the particles which participate in the heat transfer between tube and bulk move along the following flow path: From the top of the stagnating zone, along its flanks, along the tube surface and along the flanks of the void zone (see Figure 41). The local velocity $u(s)$ along this flow path is calculated using a model which has originally been developed to calculate the velocity profile in discharging hoppers. Based on the local velocity along the flow path $u(s)$, Niegsch calculates the local residence time

$$t(s) = \int_0^s \frac{1}{u(s)} ds, \tag{46}$$

which is required to evaluate the local thermal resistance between tube and bulk (see further below).

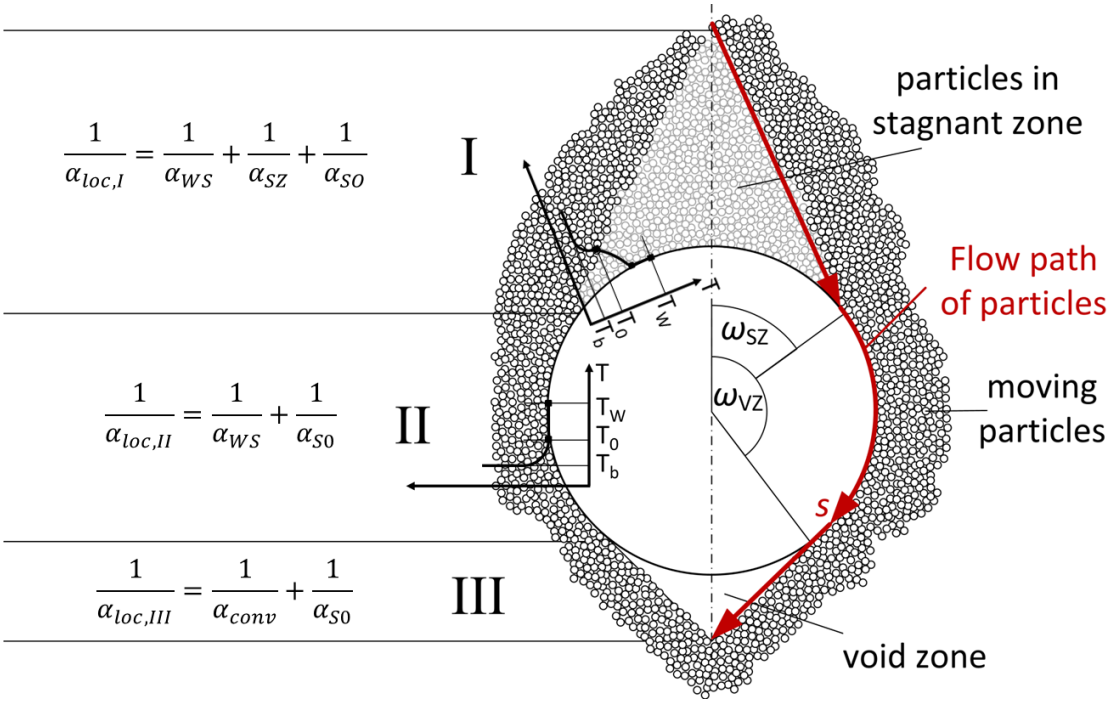

Figure 41. Heat transfer resistances and residence time according to the model concept of Niegsch (based on [86]).

The thermal resistances for each of the three sections are calculated as follows:

In section I the local heat transfer $\alpha_{loc,I}$ coefficient is made up of three thermal resistances:

$$\frac{1}{\alpha_{loc,I}} = \frac{1}{\alpha_c} + \frac{1}{\alpha_{S0}} + \frac{1}{\alpha_{SZ}} \tag{47}$$

The three heat transfer coefficients are interpreted as follows:

$(\alpha_c)^{-1}$ accounts for the thermal contact resistance between the tube surface and the first layer of particles which is calculated according to equation (18) (p. 33) in section 4.1.2.1.

The penetration resistance $(\alpha_{S0})^{-1}$ is to account for the heat transport inside the moving bulk material. Assuming a quasi-homogenous, resting medium the process is described by Fourier's law of heat conduction. An analytical solution to the corresponding bound-

ary value problem with a constant boundary temperature T_0 (see Figure 13 and Figure 41) is given by:

$$\alpha_{S0}(t) = \frac{1}{\sqrt{\pi}} \frac{\sqrt{(\lambda \rho c_p)_{S0}}}{\sqrt{t}} \tag{48}$$

Equation (48) has first been used by Mickley and Fairbanks [80] in the context of granular materials. Equation (48) assumes a semi-infinite domain and a jump of the boundary temperature T_0 at $t = 0$. The term $(\lambda \rho c_p)_{S0}$ denotes the effective quantities of the bulk (thermal conductivity, density and heat capacity).

$\alpha_{S0}(t)$ is an instantaneous quantity which depends on the temporal evolution of the temperature field and is proportional to the inverse square root of the residence time t. It is important to note that equation (48) has been derived for a quasi-homogeneous, resting medium and a constant boundary temperature T_0. In practice it has also been applied to moving bulk materials evaluating the residence time from the flow speed and the length of the flow path (see equation (46)) [76] [84] [86].

After sufficiently long residence times, i.e. at a fully developed temperature profile, the penetration resistance is no longer a function of t, but is determined by the thickness, H, of the bulk material [113]:

$$\alpha_{S0} = \frac{\pi^2}{2} \frac{\lambda_{S0}}{H} \tag{49}$$

Equation (49) is applied to evaluate the conduction resistance $(\alpha_{SZ})^{-1}$ in equation (47). It accounts for the heat transport through the resting particles on top of the tube using the radial height $H_{SZ,rad}(\omega)$ of the stagnant zone, i.e. the radial distance between tube surface and the 'surface' of the stagnant zone (see Figure 42, p. 90).

In section II, the local heat transfer coefficient $\alpha_{loc,II}$ is the same as in section I with the only difference that the conduction resistance $(\alpha_{SZ})^{-1}$ is zero:

$$\frac{1}{\alpha_{loc,II}} = \frac{1}{\alpha_c} + \frac{1}{\alpha_{S0}} \tag{50}$$

In section III, the local heat transfer coefficient $\alpha_{loc,III}$ is governed by the heat transfer through the gas phase in the void area, $(\alpha_{conv})^{-1}$, and the penetration resistance α_{S0}.

$$\frac{1}{\alpha_{\mathrm{loc,III}}} = \frac{1}{\alpha_{\mathrm{conv}}} + \frac{1}{\alpha_{\mathrm{S0}}} \tag{51}$$

α_{conv} is calculated according to equation (39) (p. 61).

Finally, Niegsch calculates the time-average of the local heat transfer coefficient for every section:

$$\alpha_{\mathrm{av,i}} = \frac{1}{t}\int_0^t \alpha_{\mathrm{loc,i}} d\tau \tag{52}$$

By taking the arithmetic mean of the averaged heat transfer coefficients $\alpha_{\mathrm{av,i}}$ around the tube circumference, Niegsch obtains an average heat transfer coefficient α_{av} for the first tube (first row of tubes) of a bundle.

To calculate also the heat transfer coefficient at subsequent rows of tubes he uses the concept of an "extended residence time". This means that the residence time of the bulk increases monotonically with every row of tubes. Given the total residence time of the bulk at a single tube, t_{tot}, the residence time at the beginning of the n-th row of tubes is:

$$t_{\mathrm{n}} = (n-1)t_{\mathrm{tot}} \tag{53}$$

The penetration resistance α_{S0} at the n-th row of tubes is then calculated using the cumulated residence time ($t_{\mathrm{n}}+\Delta t$).

6.3 Modifications to Niegsch' model

The model of Niegsch is a first step towards a simplified description of the heat transfer between a horizontal tube and a moving granular material. However, considering the findings presented in section 6.1, some modifications are proposed.

The first modification concerns the size, shape and extent of the stagnant area. Niegsch assumes the size and the extent to solely depend on the friction parameters of the system and he assumes a triangular shape. However, as seen in section 6.1.1, the size of the stagnant area primarily depends on the arrangement of the tubes, especially on the vertical pitch s_{V}. In contrast to that it is virtually independent on the inner friction angle of the bulk material. The shape of the stagnant zone is parabolic rather than triangular. Furthermore, the simulations suggest a smaller extent than estimated by Niegsch.

Modifying the size, shape and extent of the stagnant area accordingly is expected to have significant influence on the calculated heat transfer rate in section I.

The second modification concerns the extent of the void area. In accordance with the simulation results, Niegsch estimated the actual void area to start at $\omega_{VZ} \approx 150°$. However, as shown in section 6.1.2, the particles start to separate from the tube surface already at a much smaller angle $\omega_{sep} = 90°…130°$ mainly depending on the tube arrangement. As a consequence, the number of particles in touch with the tube surface gradually decreases between ω_{sep} and ω_{VZ}.

This fact influences the contact resistance $(\alpha_{WS})^{-1}$ between the tube surface and the bulk material which thus has to be adapted. A straight forward way to do this has already been shown in section 5.2.2 by introducing an angle-dependent coefficient $\varphi(\omega)$ (with $\varphi(\omega)$ being the local share of the tube surface covered by particles).

A third modification concerns the evaluation of the local residence time. Niegsch calculates the local residence time according to the velocity profile along the flow path shown in Figure 41. The local residence time is used to calculate the local penetration resistance $(\alpha_{S0})^{-1}$ according to equation (48) ($\alpha_{S0} \sim 1/\sqrt{t}$).

A major premise for the validity of equation (48) is a constant surface temperature T_0. This is approximately true within each of the three sections (section I - section III). However, the temperature T_0 in section II (at the tube surface) is much higher than T_0 in section I and section III at the flanks of the stagnant zone and the void zone (see Figure 41). This is due to the additional thermal resistances $(\alpha_{SZ})^{-1}$ (section I) and $(\alpha_{conv})^{-1}$ (section III).

Consequently, at the end of section I, the residence time cannot simply be extended to calculate the penetration resistance in the subsequent section II. In other words, if the residence time at the end of section I is $t_{I,out}$, then $t_{I,out} = t_{II,in}$ cannot be used to calculate the penetration resistance at the beginning of section II. Doing so, leads to an overestimation of the residence time at the beginning of section II and hence to an underestimation of the heat transfer in section II.

Due to these considerations it is suggested to simply keep the residence time constant within the sections I and III. This is justified as the heat transfer rate in these sections is expected to be comparably small and to be dominated by the thermal resistances of the stagnant zone $(\alpha_{SZ})^{-1}$ and of the void zone $(\alpha_{conv})^{-1}$, respectively.

Some further comments regarding the residence time: Niegsch calculates the residence time from the velocity profile directly at the heat transferring surface, i.e. from the velocity of the first layer of particles. However, the penetration resistance (equation (48)) accounts for the heat transport into the entire bulk. Evaluating the residence time from the first layer of particles therefore is only justified when the change in flow speed (the velocity gradient) in normal direction of the wall is small. In this case, however, it is equally justified to use the average velocity of the entire cross-section (plug-flow condition), which is easier to evaluate than the velocity at the surface. Using an average velocity is the approach that has been used in most of the studies in the past (e.g. [76] [87])

Alternatively, one might define an averaged velocity profile over a certain distance from the tube surface to evaluate the residence time. This length scale most reasonably should represent the local penetration depth of the temperature gradient. Ozkaynak et al. [114], for example, used such an approach to determine the void fraction in the effective region. In this case, however, several questions arise such as what kind of averaging procedure to choose, as the velocity profile close to the surface surely has greater influence than that at a certain distance from the wall. Furthermore, a generic description of the local velocity gradient at the tube surface is needed.

For simplicity, it is therefore decided to evaluate the residence time from the mean flow speed in the entire cross section between the tubes.

6.4 Enhanced model

Based on the three modifications discussed in the preceding section, an enhanced version of the Niegsch model is proposed. Just like in the model of Niegsch, the circumference of the tube is divided into three sections to calculate an effective heat transfer coefficient for each section. Equations (47) to (51) are adopted to evaluate the effective heat transfer coefficients but use modified formulations for the single thermal resistances in each section.

6.4.1 Evaluation of the effective thermal resistances

In section I the conduction resistance, $(\alpha_{SZ})^{-1}$, through the stagnant zone, is modified. The shape of the stagnant zone is approximated by a parabola which is defined by the parabola's vertex at $y = D_T/2+H_{SZ}$ and its intersection point with the tube at ω_{SZ} (see

equation (41) to (43), p. 74). The values of H_{SZ} and ω_{SZ} are determined from the findings in section 6.1.1 (Figure 35 and equation (44), p. 77 et sequation). α_{SZ} then is calculated according to equation (49) (p. 86), with H being the radial height, $H_{SZ,rad}(\omega)$ (see Figure 42), between the tube surface and the parable.

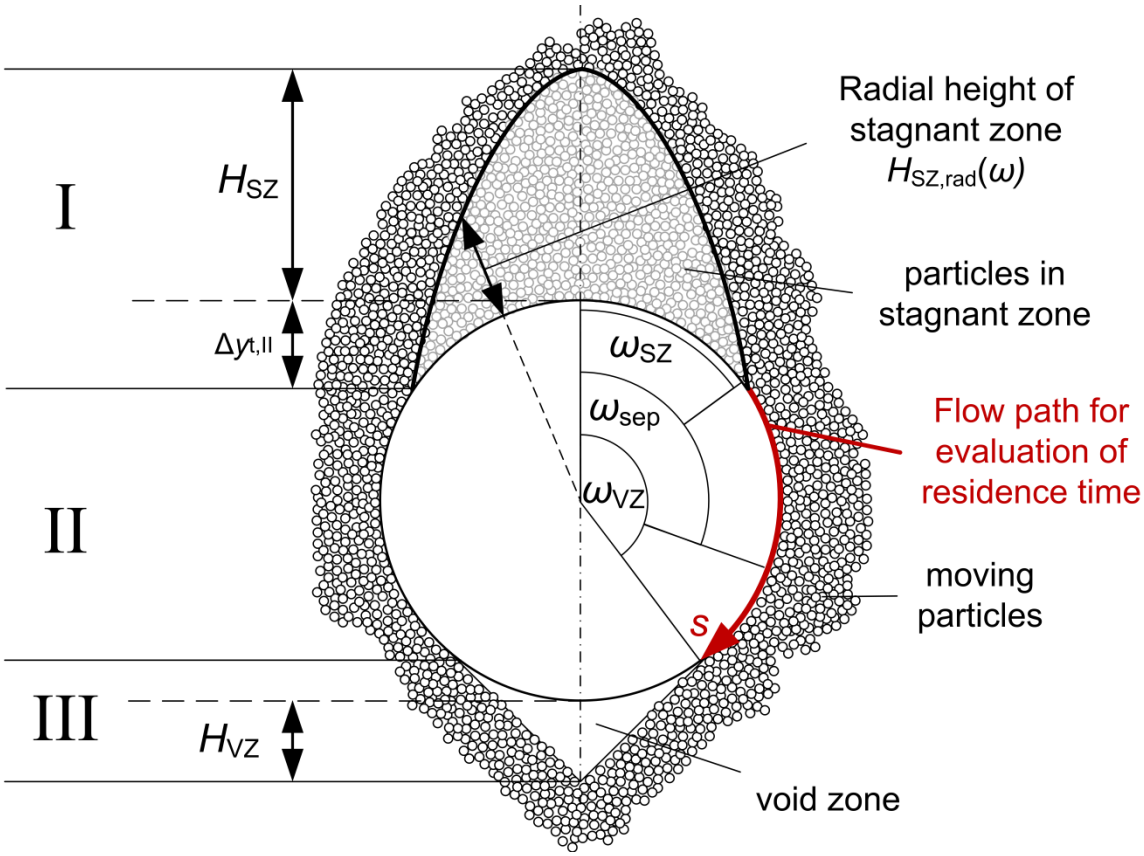

Figure 42. Schematic of flow field for enhanced model.

Furthermore, the residence time is kept constant in section I. For the first row of tubes this implies that the residence time is $t = 0$ and hence the penetration resistance $(\alpha_{S0})^{-1} = 0$. At the tube vertex ($\omega \approx 0°$) this of no significance as the overall heat transfer is dominated by the conduction resistance, $(\alpha_{SZ})^{-1}$. However, at the transition from section I to section II the radial height of the stagnant zone approaches zero and hence the conduction resistance vanishes. With $(\alpha_{S0})^{-1} = 0$, this leads to a considerable overestimation of the overall heat transfer in this area. Therefore, to avoid a zero-penetration resistance, the residence time at the beginning of section II, t_{II}, is estimated as:

$$t_{II} \approx \frac{D_T}{2} \frac{(1 - \cos(\omega_{SZ}))}{u_{ref}} \tag{54}$$

The distance $D_T/2\cdot(1-\cos(\omega_{SZ}))$ is marked in Figure 42 ("$\Delta y_{t,II}$") and denotes the vertical distance from the tube vertex to the beginning of section II. It is assumed, that in this range the penetration resistance becomes relevant for the overall heat transfer.

The effective thermal resistance in section I, $(\alpha_{loc,I})^{-1}$, is subsequently calculated according to equation (47) (p. 85), with the penetration resistance, $(\alpha_{S0}(t_{II}))^{-1}$.

In section II the effective thermal resistance is calculated the same way as in the model of Niegsch using equation (51) (p. 87). In the range of $\omega_{SZ} < \omega < \omega_{sep}$ the local residence time $t(\omega)$ is calculated using the average velocity, $\bar{u}(\omega)$, in the cross section between the tubes.

$$\bar{u}(\omega) = u_{\mathrm{ref}}\left(\frac{s_H}{s_H - D_T \sin(\omega)}\right) \tag{55}$$

In the range of $\omega_{sep} < \omega < \omega_{VZ}$ the thermal contact resistance is modified to account for the fact that the number of particles in touch with the tube surface gradually decreases. Therefore, as described in the previous section, the contact resistance $(\alpha_c)^{-1}$ is calculated using an angle-dependent coefficient $\varphi(\omega)$. $\varphi(\omega)$ is approximated by a *tanh*-function as shown in Figure 27 (p. 61).

Section III is treated the same way as in the model of Niegsch. A triangular shape of the void zone is assumed through which heat is transported by convection of the gas phase. The convection heat transfer coefficient, α_{conv} (equation (39), p. 61), is evaluated using the same Nusselt-Correlation as in section 5.2.2 (equation (67), p. 104), where it has been used to modify the continuum model.

Having defined the different (local) thermal resistances for each section I – III, the local heat transfer coefficient around the tube surface can be evaluated using equation (47), (50) and (51) (p. 85-87). To obtain the averaged heat transfer coefficient for each section I - III, the local heat transfer coefficient has to be integrated over the corresponding angle ragne $\Delta\omega$:

$$\alpha_{\mathrm{i,av}} = \frac{1}{\Delta\omega}\int_{\omega_0}^{\omega_0+\Delta\omega} \frac{1}{\sum_{\mathrm{j}} 1/\alpha_{\mathrm{j}}}\, d\omega \tag{56}$$

In equation (56) the subscript 'i' denotes the considered section (section I - III) and 'j' the different thermal resistances in the given section. ω_0 is the angle at the beginning of

the considered section and $\Delta\omega$ is the angle-range of the considered section. An analytical integration of equation (56) leads to very complex expressions if it is at all possible.

An approximation of equation (56) is obtained by integrating and averaging each of the different thermal resistances, $(\alpha_j)^{-1}$, individually:

$$\left(\frac{1}{\alpha_j}\right)_{i,av} = \frac{1}{\Delta\omega}\int_{\omega_0}^{\omega_0+\Delta\omega}\frac{1}{\alpha_j}d\omega \tag{57}$$

Subsequently, the total heat transfer coefficient is calculated from the average values of the individual resistances:

$$\alpha_{i,av} \approx \frac{1}{\sum_j\left(\frac{1}{\alpha_j}\right)_{i,av}} \tag{58}$$

For the investigated cases in this work (see Table 1, p. 24), the results of equation (58) deviate by up to 11 % from the solution of equation (56) which is obtained from numerical integration. The analytical solutions for the averaged thermal resistances $(\alpha_j)_{i,av}^{-1}$ are given in appendix C.

By weighting the effective heat transfer coefficients, $\alpha_{i,av}$, for each section according to the angle range of the corresponding section, the averaged heat transfer coefficient for the entire tube is determined.

6.4.2 Comparison with measurement data

In this section the enhanced model is used to calculate the average heat transfer coefficient at a single tube using numerical integration of equation (56). The model is applied to the four cases shown in Table 1, which have been investigated experimentally. The results are shown in Figure 43 together with the results of the model of Niegsch.

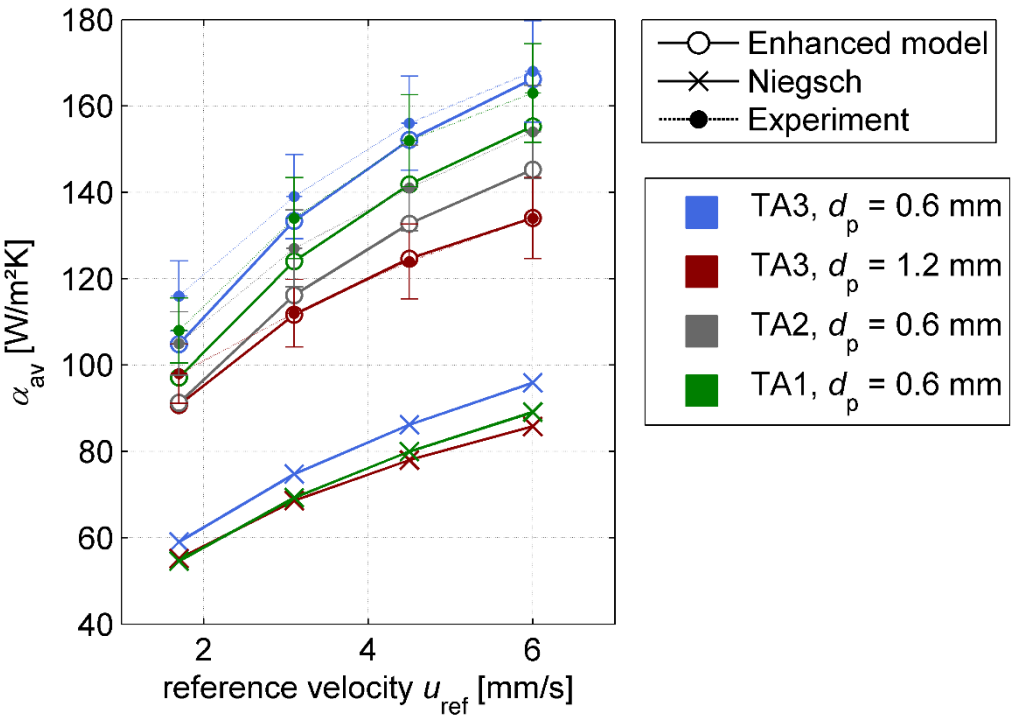

Figure 43. Averaged heat transfer coefficient, α_{av}, at different flow speeds. Comparison of experiment, model of Niegsch and enhanced model.

Both, the model of Niegsch and the enhanced model well capture the trend of the experimental curves. However, the model of Niegsch underestimates the experimental results by 35 – 50 %. This is mainly due to the evaluation of the residence time in the Niegsch model. As the residence time is extended from section I to section II, the residence time at the beginning of section II is too large which results in a low α_{S0} in section II.

Furthermore, the model of Niegsch yields exactly the same results for the cases TA2 and TA1. This is due to the fact that the model does not include the influence of the vertical tube spacing on the size of the stagnant zone.

In contrast to that, the enhanced model takes into account the variable size of the stagnant area. In accordance with the experiment, tube arrangement TA1 shows higher values of α_{av} than TA2 due to its smaller vertical pitch and the resulting smaller stagnant zone.

The enhanced model deviates by up to 14 % from the experimental data. The increased particle size leads to a reduction of α_{av} of 18 – 25 % in the experiment while in the enhanced model it is 13 – 19 %. The grain size influences the results by means of the

thermal contact resistance which decreases with increasing grain size (see equation (20), p. 34).

The enhanced model tends to underestimate the heat transfer, though less severely than the model of Niegsch. A primary reason for this underestimation is found in section II where the heat transfer is dominated by the penetration resistance, $(\alpha_{S0}(t))^{-1}$. The penetration resistance increases monotonically with the residence time and hence the maximum heat transfer coefficient occurs at the beginning of section II.

This, though, is contrary to the measurement results where the maximum of α_{av} is always found at the lateral side of the tube at $\omega \approx 90°$. This behavior originates from the constriction of the flow cross-section between the tubes. As the flow approaches the constriction it accelerates and the temperature gradient driving the heat transport into the bulk increases. This leads to an increasing heat transfer coefficient despite the continuously increasing residence time.

This effect is not considered in the calculation of the penetration resistance in the simplified model. Instead it is assumed that the temperature profile is solely determined by the residence time.

7 Conclusions and outlook

The work at hand aims at modelling dense granular flow in moving bed heat exchangers with horizontally arranged tubes. It wants to constitute the basis for future design tools by providing a precise and efficient prediction of the thermal performance of such devices.

The granular flow is modeled on three different length scales which provide different degrees of accuracy at different computational cost:

- A discrete particle model (DEM, micro scale)
- A continuum model (CFD, meso scale)
- A model for the effective heat transfer coefficient per tube (macro scale)

The 3D DEM model provides detailed insight into the relevant flow phenomena. However, due to the high computational effort it is only applied to isothermal flows and comparably short time scales.

The discrete particle model provided the following insights into the granular flow pattern around the tubes:

The size of the stagnant zone at the tube vertex, which constitutes an insulating layer between the tube and the moving bulk, can be influenced by the tube arrangement. Small stagnant zones occur in particular at small vertical tube spacings. The extent of the stagnant zone, i.e. the angle range at which the particles rest on top of the tube, depends on different parameters. One important parameter is the surface friction coefficient between tube surface and the bulk material. At low friction coefficients the particles start to slide down the tube circumference earlier. Another important parameter is the extent of the stagnant zone, which decreases significantly at very small vertical tube spacings.

In the lower part of the tube the particles start to separate from the tube surface. This, on the one hand, leads to elevated flow speeds at the tube surface. On the other hand the heat transfer rate decreases as fewer particles are in contact with the tube surface.
The point at which the particles start to separate from the tube surface can be influenced by the tube arrangement. Narrow tube arrangements promote a late separation of the

particles which again is conducive to the heat transfer rate. Furthermore, bulk materials with a large angle of internal friction tend to separate early from the tube surface.

Below the tube a void area forms where no particles are in contact with the tube surface anymore. The heat transfer rate is then governed by the heat transfer through the gas phase in the cavity. The extent of this void zone was approximately constant for all investigated cases, except to a slight influence of the internal friction angle.

Summarizing, the following factors lead to a flow pattern with enhanced heat transfer rate, and thus compact and efficient designs:

- A narrow tube arrangement (both vertical and horizontal tube spacing).
- A tube surface with a small wall friction coefficient.
- A bulk material with a small angle of internal friction.

The 2D CFD model is based on effective quantities of the bulk such as a granular viscosity and thermal conductivity. The model is less accurate than the DEM model, but includes heat transport and is applicable to larger time scales and geometries.

The CFD-model was used to calculate the profile of the local heat transfer coefficient α_{loc} along the tube surface and to compare the simulation results to measurement data. The investigated cases comprised three different tube arrangements, two different particle sizes and four different mass flow rates (inlet flow speeds).

The model well captures the influence of the flow speed and the particle size on the heat transfer rate. Qualitative differences between simulation and experiment occur in particular in the stagnant zone at the tube vertex. In this area, even small deviations regarding the particle motion and the extent of the stagnant zone have a large impact on the local heat transfer coefficient.

From the calculated and measured profiles of the local heat transfer coefficient α_{loc}, the average heat transfer coefficient per tube was calculated. For two of the investigated tube arrangements the model deviated by less than 6 % from the measurement data. For the third tube arrangement a maximum deviation of 20 % was observed. Hence, within these limits of accuracy, the model is considered a reliable tool for the prediction of the thermal performance of a given heat exchanger design.

The macro-scale model is an enhanced version of an existing model from literature. It is based on characteristic flow sections which offer a basic description of the flow pattern around the tubes. They describe the size and extent of the stagnant and void area and

define the velocity profile along the tube surface. These characteristic flow sections were obtained from DEM simulations as functions of the relevant influencing parameters.

This model was used to calculate the averaged heat transfer coefficient between tube and bulk material. The results were compared to the measurement data mentioned above at varying tube arrangement, particle size and mass flow rate. The maximum deviation between simulation and experiment was 13 %.

The results of this work show significant enhancement compared to existing models such as the one of Baumann [1], Niegsch [2] or Schlünder [3], who exhibit deviations of 40 to 50 % from the experimental data.

Subsequent works may address on the following topics:

The continuum model still offers potential for further enhancement through including a hydrodynamic description of the void area below the tubes. So far, the void area is accounted for by a correction factor of the heat transfer rate in the corresponding area.

The interstitial gas phase between the particles is included in the current CFD model and showed a significant influence on the heat transfer rate in one specific case. However, the effect could not be verified by the experiment. As the influence of the gas phase is likely to increase at higher operating temperatures, further investigations are advisable.

The continuum model and the macro scale model offer the potential to evaluate the heat transfer in a sequence (of rows) of tubes. With respect to the experimental setup used in this work, only the heat transfer at a single tube has been investigated. However, the heat transfer coefficient at subsequent rows of tubes changes according to the evolution of the temperature profile inside the bulk. Thus, the models should also be validated based on an experimental setup with multiple rows of tubes.

This work has dealt in depth with the modelling of moving bed heat exchangers. Its results are to promote the cost-efficiency and compactness of these devices, which are a central element in solar thermal power plants with granular heat transfer fluids and, perspectively, in further applications that contribute to a sustainable power supply in the future.

Appendix A: Selected details on experimental procedures

A.1 Grain size distribution of quartz sand

For the measurement of the local heat transfer as described in section 3.2 two different samples of quartz sand were used with an average grain size of $d_p \approx 0.6$ mm and $d_p \approx 1.2$ mm. For the optical measurement of the flow field (section 3.1) the quartz sand with $d_p \approx 0.6$ mm was used. Here, the grain size distribution of the two materials are given.

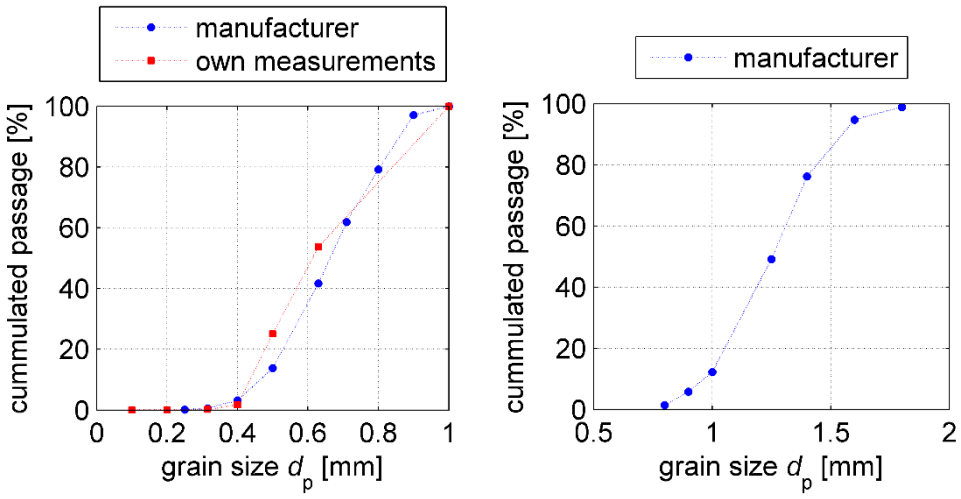

Figure 44. Grain size distribution of the quartz sand used in this work. Left: Sand with a median grain size of $d_{p50} \approx 0.6$ mm. Right: Sand with a median grain size of $d_{p50} \approx 1.2$ mm.

A.2 Error estimate of measurement of local heat transfer

In section 3.2 the setup for the measurement of the local heat transfer coefficient at the tube surface is described. The measurement is based on conductive heating of a stainless steel foil due to its ohmic resistance, resulting in a heat flux $\dot{q}$. In addition, the local wall temperature, $T_W(\omega)$, and the reference temperature, T_{ref}, are measured, and the heat transfer coefficient is calculated using equation (3)

$$\alpha_{\mathrm{loc}}(\omega) = \frac{\dot{q}}{T_{\mathrm{W}}(\omega) - T_{\mathrm{ref}}}, \tag{3}$$

with

$$\dot{q} = \frac{I^2 R}{A}.$$

The maximum measurement uncertainty of the derived heat transfer coefficient, $\Delta\alpha_{\mathrm{loc,max}}$, due to the uncertainties Δx_{i} of the quantities x_{i}, is calculated as follows (linear propagation of uncertainty):

$$\Delta\alpha_{\mathrm{loc,max}} = \sum_{\mathrm{i}} \left| \frac{\partial \alpha_{\mathrm{loc}}}{\partial x_{\mathrm{i}}} \Delta x_{\mathrm{i}} \right| \tag{59}$$

Subsequently, the measurement uncertainties of the parameters x_{i} are given:

Ohmic resistance *R*:

The manufacturer states a relative uncertainty of $\Delta R = 0.05$ %.

Electrical current *I*:

During the measurement fluctuations of the current of $\Delta I_{\mathrm{abs}} \approx 0.1$ A were observed which leads to

$$\Delta I = \frac{\Delta I_{\mathrm{abs}}}{I} = \frac{0.1\ A}{30\ A} = 0.3\ \% \tag{60}$$

Surface area, *A*, of the foil:

The surface area is $A = b \cdot l = (80 \cdot 300)$ mm² where the length and the width of the foil were measured with an absolute uncertaintiy of $\Delta b_{\mathrm{abs}} = \Delta l_{\mathrm{abs}} = 1$ mm. It follows

$$\frac{\Delta A_{\mathrm{abs}}}{A} = \frac{1}{A}\left(\frac{\partial A}{\partial b}\Delta b_{\mathrm{abs}} + \frac{\partial A}{\partial l}\Delta l_{\mathrm{abs}}\right) = 1.6\ \% \tag{61}$$

Total uncertainty of heat flux $\dot{q}$:

As discussed in section 3.2, the assumption that the current density is distributed homogeneously around the circumference of the tube leads to an uncertainty of the heat flux of about $\Delta\dot{q}_{\mathrm{l}} \approx 2.5$ %. Together with the uncertainties of *R*, *I* and *A* the maximum total error of the heat flux is:

$$\Delta\dot{q} = \Delta\dot{q}_1 + \Delta R + 2\Delta I + \Delta A \approx 4.5\ \% \tag{62}$$

Surface temperature $T_W(\omega)$ and reference temperature T_{ref}:

The thermocouples for the measurement of the temperature data were calibrated beforehand. As only the difference ($T_W(\omega)$-T_{ref}) is used in equation (3) the uncertainty of the absolute measured temperature is not relevant. Due to fluctuations during the measurement, the precision of the temperature value is approximately 0.2 K for each thermocouple. Therefore, the uncertainty due to the precision of the temperature, ΔT, measurement is

$$\Delta T = \frac{2 \cdot 0.2\ K}{T_W(\omega) - T_{ref}}. \tag{63}$$

The error, ΔT, maximizes where the temperature difference takes its minimum value ($T_W(\omega)$ - T_{ref}) ≈ 19 K which is at the lateral sides of the tubes where the heat transfer reaches its maximum. This leads to a maximum $\Delta T_{max} \approx 2$ %.

Summarizing the results of the preceding paragraphs the maximum error of the local heat transfer coefficient according to equation (3) is

$$\Delta\alpha_{loc,max} = (\Delta T)_{max} + \Delta\dot{q} = 6.5\ \% \tag{64}$$

A.3 Error estimate of determination of internal granular flow speed

The flow inside the mockup cannot be measured directly. Therefore, the average flow speed in the free cross section of the heat exchanger is calculated from the mass flow rate.

This section gives an estimate on the deviation of the actual flow speed inside the mockup from the average flow speed which is

$$u_{ref} = \frac{\dot{m}}{\rho_{S0} A} \tag{65}$$

The cross-sectional area of the mockup is $A = 0.064$ m² with a negligible uncertainty. The effective density, ρ_{S0}, of the bulk material was measured under shear deformation using an annular shear cell. The effective density ranged from 1550 kg/m² to

1650 kg/m³ depending on the applied normal force, which corresponds to an uncertainty of approximately 3 %.

To measure the mass flow rate, $\dot{m}$, a certain rotational speed of the chain conveyor was adjusted and the cumulated mass over a defined time span was measured. The estimated accuracy of this measurement is 2 %. Therefore, the overall measurement error of u_{ref} is approximately 5 %.

However, the results of the PIV measurements in section 3.1 indicate that the flow is not completely evenly distributed across the cross-section. Deviations of the local flow speed from the average of up to 25 % are observed at the front wall of the mockup (see Figure 8). Possible origins for this maldistribution are disturbing influences from the preceding tube rows and the change of the free cross-section between two subsequent tube rows due to the guiding plates at the lateral sides of the mockup (see Figure 5, p. 16).

Further disturbing effects might originate from the tube chain conveyor, transporting particles from the bottom of the test rig to the bulk storage at the top (see Figure 5, p. 16). In particular two effects are to be mentioned:

Firstly, the conveyor chain rotates counter clockwise in the two branches (pear-shaped tubes). In the left branch the chain with the conveyor plates moves downward. It then removes bulk material to the right and moves, loaded with particles, upward in the right branch. This means that the particles are removed asymmetrically to the right at the bottom of the test rig. Although, there is more than 600 mm distance between the bottom of the test rig and the outlet of the heat exchanger, this might induce horizontal asymmetries in the flow field in the heat exchanger.

Secondly, the conveyor plates which are removing the bulk material are installed in a certain distance to one another at the conveyor chain. This means that the bulk material is not removed in a perfectly continuously way. Instead, slight oscillations are induced on the flow rate at the bottom of the test rig which might still be noticeable upstream in the flow profile in the heat exchanger.

A.4 Measurement of the wall friction coefficient between quartz sand and an acrylic glass surface

In section 5.1 the discrete particle model is validated based on measurements of the granular flow field in a transparent heat exchanger mockup. The measurement, however, is restricted to the flow at the acrylic glass front wall of the mockup. Therefore, the wall friction coefficient between the front wall and the bulk material has to be taken into account.

The wall friction coefficient between quartz sand and an acrylic glass surface was measured using an annular shear cell. The shear stress was measured at different normal stresses and the measurement was repeated seven times. The averaged results of the measurements are shown in Figure 45. The vertical error bars denote the maximum deviation of the individual measurements.

As shown in Figure 45 the surface friction angle is a function of the normal stress. Therefore, to find the friction angle relevant for the measurement, the normal stress in the experimental setup, i.e. the normal (horizontal) stress on the acrylic glass front wall in the heat exchanger mockup, has to be estimated.

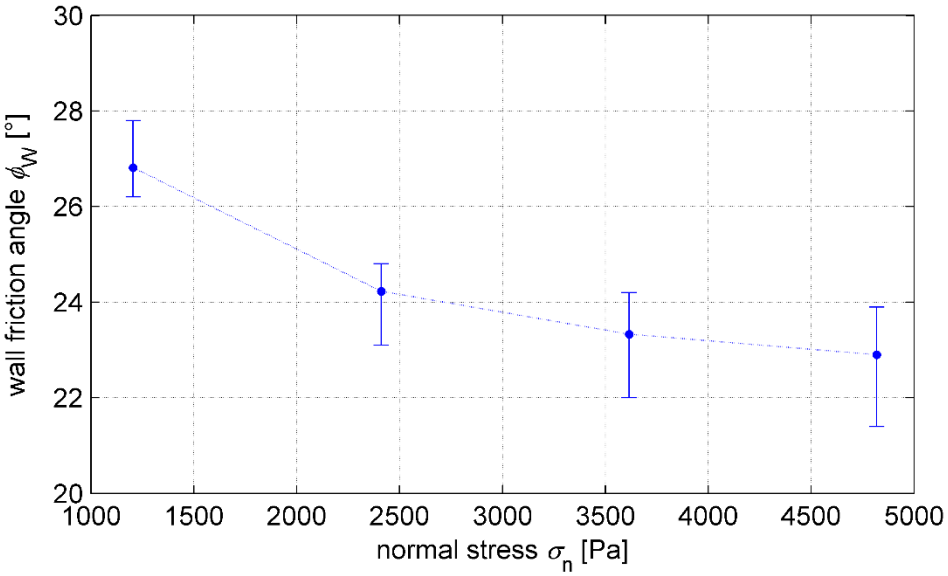

Figure 45. Measurement of surface friction angle between quartz sand and an acrylic glass surface at different normal stresses.

To this end, the well-known Janssen-model is used (e.g. in [17]) which has been developed to calculate the stresses in silos. In contrast to a liquid, the vertical and horizontal stresses in a silo filled with a granular material do not increase infinitely with the height of the silo. Instead they approach a maximum stress which primarily depends on the diameter of the silo. The Janssen-model yields the following formulation for the maximum horizontal stress $\sigma_{\mathrm{H,max}}$:

$$\sigma_{\mathrm{H,max}} = \frac{g \rho_{S0} A}{\tan(\phi_W)\, U} \tag{66}$$

With the cross-sectional area A = 0.064 m² and the perimeter U = 1.04 m of the test rig a maximum horizontal stress is $\sigma_{\mathrm{H,max}}$ = 1800…2100 Pa, depending on the wall friction angle. At this upper bound for σ_{H}, Figure 45 yields a wall friction angle of $\phi_{\mathrm{W}} \approx$ 25°…27°, which corresponds to $\mu_{\mathrm{W}} = \tan(\phi_{\mathrm{W}}) \approx 0.5°$.

Appendix B: Selected details on the continuum model

B.1 Heat transfer through the void area below the tubes

The convective heat transport through the cavity below the tubes, α_{conv}, is calculated according to equation (39) (see p. 61):

$$\alpha_{\mathrm{conv}}(\omega = 180°) = \frac{\lambda_{\mathrm{f}}}{H_{\mathrm{VZ}}} Nu \tag{39}$$

Here, H_{VZ} is the height of the void area (see further below) and Nu is a Nusselt correlation according to Churchill and Chu [112] which has already been used by Niegsch [86] for the same purpose. The correlation has actually been developed for a vertical plate. Correlations for cylinders also exist, but they yield only averaged values for the whole circumference.

$$Nu = (0.825 + 0.387\left(Ra^{\frac{1}{6}} \cdot \mathrm{f(Pr)}\right)^2, \text{with}$$
$$\mathrm{f(Pr)} = \left(1 + \left(\frac{0.492}{\mathrm{Pr}}\right)^{9/16}\right)^{-8/27} \tag{67}$$

The Rayleigh number $Ra = Gr \cdot Pr$ is defined in terms of the Prandtl number Pr and the Grashof number Gr:

$$Gr = \frac{g l^3}{\nu^2} \frac{T_{\mathrm{W}} - T_{\mathrm{S0}}}{T_{\mathrm{mK}}}, \text{with } l = \pi D_{\mathrm{T}} \frac{\phi_{\mathrm{r}}}{360°} \tag{68}$$

In equation (68) T_{mK} is the mean Kelvin temperature between wall temperature T_{W} and the bulk temperature T_{S0}. The characteristic length l is the arc length of the uncovered tube wall.

The height, H_{VZ}, of the void area is

$$H_{VZ} = \frac{D_T}{2}\left(\frac{1}{\cos(\phi_{\mathrm{r}})} - 1\right) \tag{69}$$

Equation (69) assumes that the flanks of the void area below the tube are tangential to the tube surface which is in accordance with the results of the DEM-simulations.

In the range of $\omega_{VZ} < \omega < 180°$, the convective heat transfer, $\alpha_{conv}(\omega)$, is interpolate linearly between $\alpha_{conv}(\omega = 180°)$ and $\alpha_c(\omega = \omega_{VZ})$ which is calculated according to equation (18) (p. 33) with $\varphi(\omega_{VZ}) = 0$:

$$\alpha_{\mathrm{conv}}(\omega) = \frac{\alpha_{\mathrm{conv}}(180°) - \alpha_c(\omega_{VZ})}{180° - \omega_{VZ}}(\omega - \omega_{VZ}) + \alpha_c(\omega_{VZ}) \tag{70}$$

B.2 Thermal contact resistance

The thermal contact resistance, $(\alpha_c)^{-1}$, between the tube surface and the bulk material is calculated according to equation (18)

$$\alpha_{\mathrm{c}} = \varphi\alpha_{\mathrm{WP}} - (1 - \varphi)\alpha_{\mathrm{con}} + \alpha_{\mathrm{rad}} \tag{18}$$

The factor φ is the local ratio of the tube surface, covered with particles (see section 4.1.2.1). In the range of $\omega_{SZ} \leq \omega \leq \omega_{sep}$, φ is approximately constant. In the range of $\omega_{SZ} \leq \omega \leq \omega_{sep}$, it changes as the particles gradually detach themselves from the tube surface. In this range, $\varphi(\omega)$ can be approximated using a *tanh*-function:

$$\varphi(\omega) = -0.5\varphi_0\left\{\tanh\left[\frac{4}{\omega_{\mathrm{VZ}} - \omega_{\mathrm{sep}}}\left(\omega - \frac{\omega_{\mathrm{sep}}}{2}\left(1 + \frac{\omega_{\mathrm{VZ}}}{\omega_{\mathrm{sep}}}\right)\right)\right] - 1\right\} \tag{71}$$

This formulation results in the plot shown in Figure 27 (p. 61) and has been used to modify the continuum model as described in section 5.2.2 where a value of $\varphi_0 = 0.65$ is used.

Subsequently, the formulations for the coefficients α_{rad}, α_{con} and α_{WP} in equation (18) are given according to Schlünder and Tsotsas [3] [115].

α_{rad} is the heat transfer due to radiation. Schlünder [3] recommends the following correlation:

$$\alpha_{\mathrm{rad}} = 4C_{12}T_{\mathrm{m}}^3 \tag{72}$$

with

$$T_{\mathrm{m}} = \frac{T_1 + T_2}{2}. \tag{73}$$

T_1 and T_2 are the temperature of the wall and the temperature of the bulk material close to the wall, respectively. C_{12} is a radiation coefficient:

$$C_{12} = \frac{C_\mathrm{s}}{\frac{1}{\varepsilon_1} + \frac{1}{\varepsilon_2} - 1} \tag{74}$$

ε_1 and ε_2 are the emission coefficients of the wall ($\varepsilon_1 = 0.1$[8]) and the bulk ($\varepsilon_2 = 0.9$[9]), respectively. C_s is the radiation coefficient of a black body $C_\mathrm{s} = 5.67 \cdot 10^{-8}\ \mathrm{Wm^{-2}K^{-4}}$.

α_con in equation (18) accounts for the heat transfer through the gas phase to the second layer of particles. It is calculated as follows:

$$\alpha_\mathrm{con} = \frac{\frac{2\lambda_\mathrm{f}}{d_\mathrm{p}}}{\sqrt{2} + \frac{2(l + h_\mathrm{R})}{d_\mathrm{p}}} \tag{75}$$

The mean free path l of the molecules of the fluid is

$$l = 2\frac{(2-\gamma)}{\gamma}\sqrt{\frac{2\pi T R_\mathrm{g}}{M_\mathrm{f}}}\frac{\lambda_\mathrm{f}}{p\left(2c_\mathrm{p,f} - \frac{R_\mathrm{g}}{M_\mathrm{f}}\right)} \tag{76}$$

In equation (76) R_g is the universal gas constant, M_f is the molar mass of the gas molecules and γ is the accommodation coefficient of the fluid phase which is for air:

$$\lg\left(\frac{1}{\gamma} - 1\right) = 0.6 - \frac{\frac{1000}{T} + 1}{2.8} \tag{77}$$

The heat transfer coefficient from the wall to a contacting particle has already been given in equation (20):

$$\alpha_{WP} = \frac{4\lambda_\mathrm{f}}{d_\mathrm{p}}\left\{\left[1 + \frac{2(l + h_\mathrm{R})}{d_\mathrm{p}}\right]\ln\left[1 + \frac{d_\mathrm{p}}{2(l + h_\mathrm{R})}\right] - 1\right\} \tag{20}$$

[8] For polished steels values of $\varepsilon \approx 0.1$ [117]

[9] For ‚rough sand' $\varepsilon \approx 0.85$ [117]

B.3 Thermal conductivity in the continuum model

The effective thermal conductivity of the granular material is calculated using a model proposed by Zehner and Schlünder [3] for a monodisperse bulk material with spherical particles:

$$\lambda_{S0} = \lambda_f\left(1-\sqrt{1-\varepsilon_f}\right)\left(\frac{\varepsilon_f}{\varepsilon_f - 1 + \frac{\lambda_f}{\lambda_D}} + \varepsilon_f\frac{\lambda_{rad}}{\lambda_f}\right) + \sqrt{1-\varepsilon_f}\left[\varphi_P\frac{\lambda_P}{\lambda_f} + (1-\varphi_P)\frac{\lambda'_{S0}}{\lambda_f}\right] \tag{78}$$

The first summand in equation (78) accounts for the heat transport through the gas phase with $\left(1-\sqrt{1-\varepsilon_f}\right)$ being an empirical weighting factor. The second summand accounts for the heat transport through the solid phase which involves transport through the gas gap between particles (λ'_{S0}) and through the contact point (λ_p)[10]. The two mechanisms (λ'_{S0} and λ_P) are weighted according to the factor φ_P which accounts for the flattening of the particle surface at the contact point. For ceramic spheres Schlünder states φ_P = 0,0077.

The heat transport through the gas gap between particles, λ'_{S0}, is calculated as follows:

$$\frac{\lambda'_{S0}}{\lambda_f} = \frac{2}{K}\left\{\frac{B\left(\frac{\lambda_P}{\lambda_f}+\frac{\lambda_{rad}}{\lambda_f}-1\right)\frac{\lambda_f}{\lambda_D}\frac{\lambda_f}{\lambda_P}}{K^2}\ln\frac{\left(\frac{\lambda_P}{\lambda_f}+\frac{\lambda_{rad}}{\lambda_f}\right)\frac{\lambda_f}{\lambda_D}}{B\left[1+\left(\frac{\lambda_f}{\lambda_D}-1\right)\left(\frac{\lambda_P}{\lambda_f}+\frac{\lambda_{rad}}{\lambda_f}\right)\right]} + \frac{B+1}{2B}\left\{\frac{\lambda_{rad}}{\lambda_f}\frac{\lambda_f}{\lambda_D} - B\left[1+\left(\frac{\lambda_f}{\lambda_D}-1\right)\frac{\lambda_{rad}}{\lambda_f}\right]\right\} - \frac{B-1}{K}\frac{\lambda_f}{\lambda_D}\right\} \tag{79}$$

with

$$K = \frac{\lambda_f}{\lambda_D}\left[1+\left(\frac{\lambda_{rad}}{\lambda_f} - B\frac{\lambda_D}{\lambda_f}\right)\frac{\lambda_G}{\lambda_P}\right] - B\left(\frac{\lambda_f}{\lambda_D}-1\right)\left(1+\frac{\lambda_{rad}}{\lambda_f}\frac{\lambda_f}{\lambda_P}\right) \tag{80}$$

$$B = 1.25\left(\frac{1-\varepsilon_f}{\varepsilon_f}\right)^{10/9} \tag{81}$$

[10] λ_P is the pure substance conductivity of the particles (the solid phase)

$$\frac{\lambda_{\mathrm{rad}}}{\lambda_{\mathrm{f}}} = \frac{4C_{\mathrm{s}}}{\frac{2}{\varepsilon_{\mathrm{P}}} - 1} T^3 \frac{d_{\mathrm{p}}}{\lambda_{\mathrm{f}}} \tag{82}$$

and

$$\frac{\lambda_{\mathrm{f}}}{\lambda_{\mathrm{D}}} = 1 - \frac{l}{d_{\mathrm{p}}} \tag{83}$$

The effective thermal conductivity λ_{S0} of the bulk material has to be split up into the two thermal conductivities of the solid and the fluid phase, λ_s and λ_f, respectively. To this end, the approach of Kuipers et al. [78] is used.

The splitting must satisfy the following condition:

$$\lambda_{\mathrm{S0}} = \varepsilon_{\mathrm{f}}\lambda_{\mathrm{f}} + \varepsilon_{\mathrm{s}}\lambda_{\mathrm{s}} = \varepsilon_{\mathrm{f}}\lambda_{\mathrm{f}} + (1 - \varepsilon_{\mathrm{f}})\lambda_{\mathrm{s}} \tag{84}$$

Based on the empirical weighting factor of the heat transport through the gas phase given by Schlünder (see equation (78)), Kuipers calculates for the gas phase:

$$\varepsilon_{\mathrm{f}}\lambda_{\mathrm{f}} = \left(1 - \sqrt{1 - \varepsilon_{\mathrm{f}}}\right)\lambda_{\mathrm{f,0}} \tag{85}$$

Where $\lambda_{f,0}$ is the conductivity of the pure substance of the fluid phase. The conductivity of the solid phase thus is

$$(1 - \varepsilon_{\mathrm{f}})\lambda_{\mathrm{s}} = \lambda_{\mathrm{S0}} - \varepsilon_{\mathrm{f}}\lambda_{\mathrm{f}} \tag{86}$$

B.4 Interphase heat transfer coefficient between phases

The heat exchange term between the granular and the fluid phase in the continuum model is given by equation (12) (p. 29):

$$Q_{\mathrm{ij}} = \alpha_{\mathrm{fs}} A_{\mathrm{fs}} (T_{\mathrm{i}} - T_{\mathrm{j}}) \tag{12}$$

The interfacial area A_{fs} is given by

$$A_{\mathrm{fs}} = \frac{6(1 - \varepsilon_{\mathrm{f}})}{d_{\mathrm{p}}} \tag{87}$$

The fluid-particle heat transfer coefficient α_{ij} is calculated according to a correlation of Gunn [96]

$$\alpha_{fs} = \frac{Nu_{fs}\lambda_{f,0}}{d_p} \tag{88}$$

with

$$\begin{aligned} Nu_{fs} = &\left(7 - 10\varepsilon_f + 5\varepsilon_f^2\right)\left[1 + 0.7\left(Re_p\right)^{0.2}(\mathrm{Pr})^{1/3}\right] \\ &+ \left(1.33 - 2.40\varepsilon_f + 1.20\varepsilon_f^2\right)\left(Re_p\right)^{0.7}(\mathrm{Pr})^{1/3} \end{aligned} \tag{89}$$

Re_p is the particle-Reynolds number

$$Re_p = \frac{\varepsilon_f \rho_f |\boldsymbol{u}_f - \boldsymbol{u}_s| d_p}{\mu_f} \tag{90}$$

Equation (90) is valid for a wide range of packing fractions ($0 < \varepsilon_s < 0.65$) and Reynolds-numbers ($Re_p < 10^5$)

B.5 Plasticity model without "critical state approximation"

In section 4.1.1 the constitutive relation for the frictional stresses in the granular material was given as:

$$\boldsymbol{\sigma}_c = p_c \boldsymbol{I} + \boldsymbol{\tau}_c = p_c \boldsymbol{I} + \frac{1}{\sqrt{2}}\tau(\varepsilon_s)\frac{\boldsymbol{S}}{|\boldsymbol{S}|} \tag{91}$$

with

$$\tau(\varepsilon_s) = \sqrt{2}\sin(\phi_i)\, p_c(\varepsilon_s) \tag{92}$$

Besides the material parameter ϕ_i, the yield criterion $\tau(\varepsilon_s)$ solely depends on the packing fraction ε_s, as p_c is a function only of ε_s. This assumption, that there is an explicit correlation between p and ε_s and τ and ε_s, is only true at the so-called "critical state" which is indicated in equation (91) and equation (92) by the subscript "c". This approximation is called the "critical-state approximation" [48], which is true at large strains and if the changes in volume fraction are small. However, if the volume fraction changes consid-

erably, the state of the material is far away from the critical state and in this case the yield criterion is a function both of the volume fraction ε_s and the pressure p. Such a yield condition $\tau(p,\varepsilon_s)$ has been proposed by Roscoe [52] (in [56]) which is known as the Cam-Clay model:

$$\tau(p,\varepsilon_s) = \sin\phi_i \, p_c(\varepsilon_s)\left(1 - \frac{\left(p - p_c(\varepsilon_s)\right)^2}{p_c(\varepsilon_s)^2}\right) \tag{93}$$

Where $\tau(p,\varepsilon_s)$ is the deviatoric stress and p is the pressure:

$$p = \frac{1}{3} tr(\boldsymbol{\sigma}) \tag{94}$$

$$\tau = |\boldsymbol{\tau}| = |\boldsymbol{\sigma} - p\boldsymbol{I}| \tag{95}$$

p_c is called the "Equation of State" (EOS) [57] and is the pressure at the critical state. At a given packing fraction (given $p_c(\varepsilon_s)$), equation (93) is a semicircle in the τ-p-space as depicted in Figure 46. The vertices of the semicircles form the "critical-state line" where $p = p_c$ and where the yield criterion $\tau(p,\varepsilon_s)$ (equation (93)) reduces to $\tau(\varepsilon_s)$ (equation (92)).

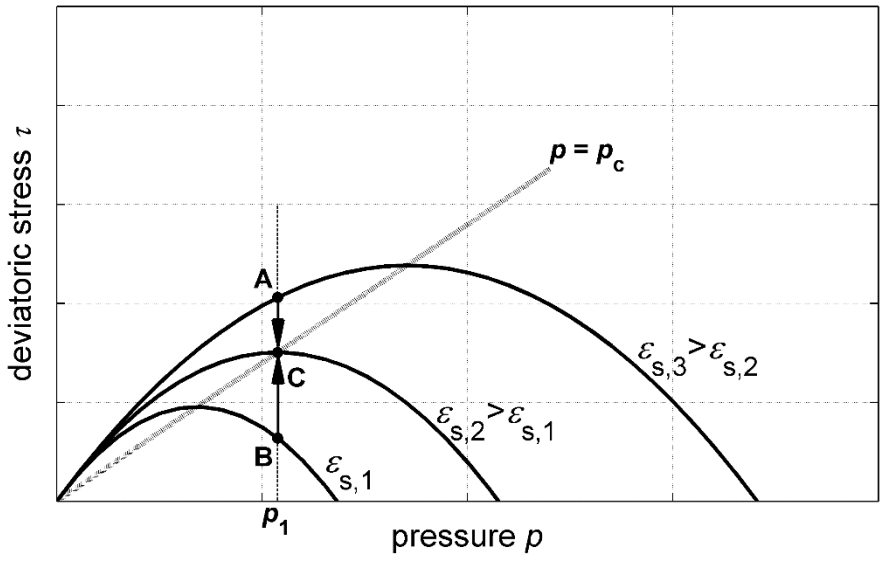

Figure 46. Yield function schematically according to equation (93) in τ-p-space.

Consider a granular material with an initially dense packing fraction $\varepsilon_{s,3}$ at pressure p_1. In the τ-p-space the state of the material is located above the critical-state line (point A).

If the material deforms (at constant pressure p_1) it delates ($\nabla \cdot \boldsymbol{u} > 0$) until it reaches the critical-state packing fraction $\varepsilon_c(p_1) = \varepsilon_{s,2}$ (point C), where it deforms without any volume change ($\nabla \cdot \boldsymbol{u} = 0$). In the same way, a material with an initially loose packing fraction ($\varepsilon_{s,1}$ at p_1, point B) will compact ($\nabla \cdot \boldsymbol{u} < 0$) until again it reaches the critical state at point C.

This dilation and compaction behavior is stipulated mathematically by the so-called normality condition which relates the rate of deformation of the material to the geometry of the yield surface:

$$\nabla \cdot \boldsymbol{u} = \frac{1}{\sqrt{2}} \frac{\partial \tau(p, \varepsilon_s)}{\partial p} |\boldsymbol{S}| \tag{96}$$

With equation (96) and equation (93), formulations for the granular pressure and the granular viscosity can be derived:

$$p = p_c \left(1 + \frac{\nabla \cdot \boldsymbol{u}}{\sqrt{2} \sin(\phi_i) \, |\boldsymbol{S}|} \right) \tag{97}$$

$$\mu = \frac{\tau(p, \varepsilon_s)}{\sqrt{2} |\boldsymbol{S}|} \tag{98}$$

B.6 Grid independence of simulation results

The numerical mesh for the reference geometry in Table 4 (s_V = 50 mm, s_H = 57 mm) is shown in Figure 47 (left). The mesh is refined at the tube surface (Δx = 0.6 mm) to properly resolve the temperature gradient at the tube surface.

Figure 47 (right) shows the dependence of the simulation results on the mesh size (u_{ref} = 5.0 mm/s). For a further refinement (Δx = 0.3 mm) the heat transferred per tube changes by less than 2 % and remains constant at even further refinement (Δx = 0.15 mm).

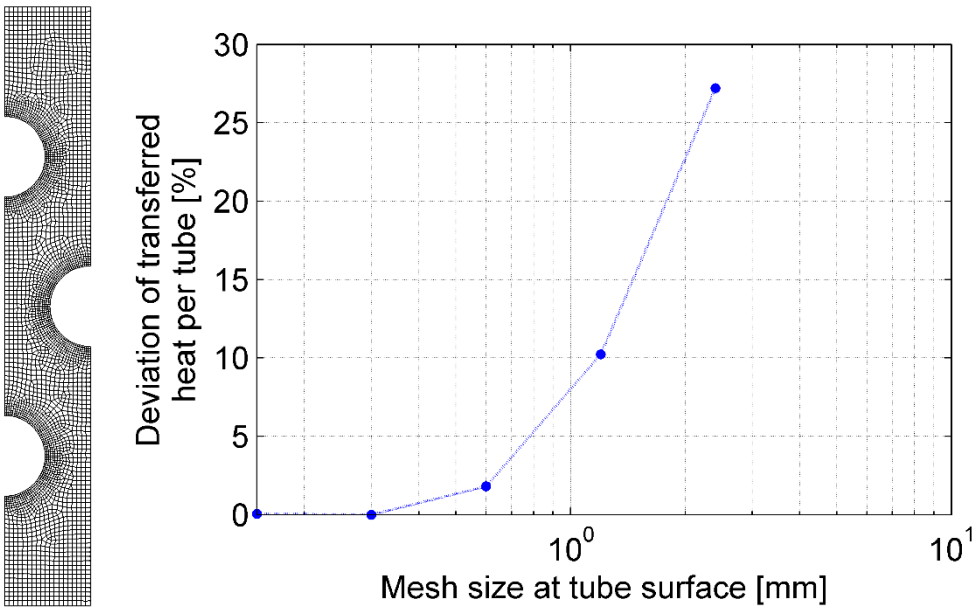

Figure 47. Left: Numerical mesh for continuum model (reference case, s_V = 50 mm, s_H = 57 mm). Right: Convergence of the simulation results for the heat transferred per tube, normalized by the simulation results of the finest grid.

Appendix C: Simplified model - Analytical approximation of effective heat transfer coefficient

To evaluate the average heat transfer coefficient for each section I - III, equation (56) (p. 91) has to be integrated numerically. An analytical approximation is obtained by integrating and averaging each of the different thermal resistances, $(\alpha_j)^{-1}$, individually:

$$\left(\frac{1}{\alpha_j}\right)_{i,av} = \frac{1}{\Delta\omega}\int_{\omega_0}^{\omega_0+\Delta\omega}\frac{1}{\alpha_j}d\omega \tag{57}$$

Subsequently, the total heat transfer coefficient is calculated from the average values of the individual resistances:

$$\alpha_{i,av} \approx \frac{1}{\sum_j \left(\frac{1}{\alpha_j}\right)_{i,av}} \tag{58}$$

In the following section the solutions for the averaged thermal resistances $(\alpha_j)^{-1}_{i,av}$ are given.

C.1 Section I

In the stagnant area, the total effective heat transfer coefficient, $\alpha_{I,av}$, is approximated by

$$\alpha_{I,av} \approx \left(\left(\frac{1}{\alpha_c}\right)_{I,av} + \left(\frac{1}{\alpha_{S0}}\right)_{I,av} + \left(\frac{1}{\alpha_{SZ}}\right)_{I,av}\right)^{-1} \tag{99}$$

α_c and α_{S0} are constant in the stagnant area and hence

$$\left(\frac{1}{\alpha_c}\right)_{I,av} = \frac{1}{\alpha_c} \tag{100}$$

and

$$\left(\frac{1}{\alpha_{S0}}\right)_{I,av} = \frac{1}{\alpha_{S0}} \tag{101}$$

The penetration resistance, $(\alpha_{S0})^{-1}$, is calculated using the residence time at the beginning of section I. At the first row of tubes, the residence time is calculated according to equation (54) (p. 90). For the subsequent row of tubes it is the residence time at the end of the preceding row of tubes.

The conduction resistance $(\alpha_{SZ})^{-1}$ depends on the radial height, $H_{SZ,rad}(\omega)$ (see Figure 48) of the stagnant zone and is calculated according to equation (49) (p. 86). The shape of the stagnant zone is approximated by a parable using equation (41) to (43) (p. 74).

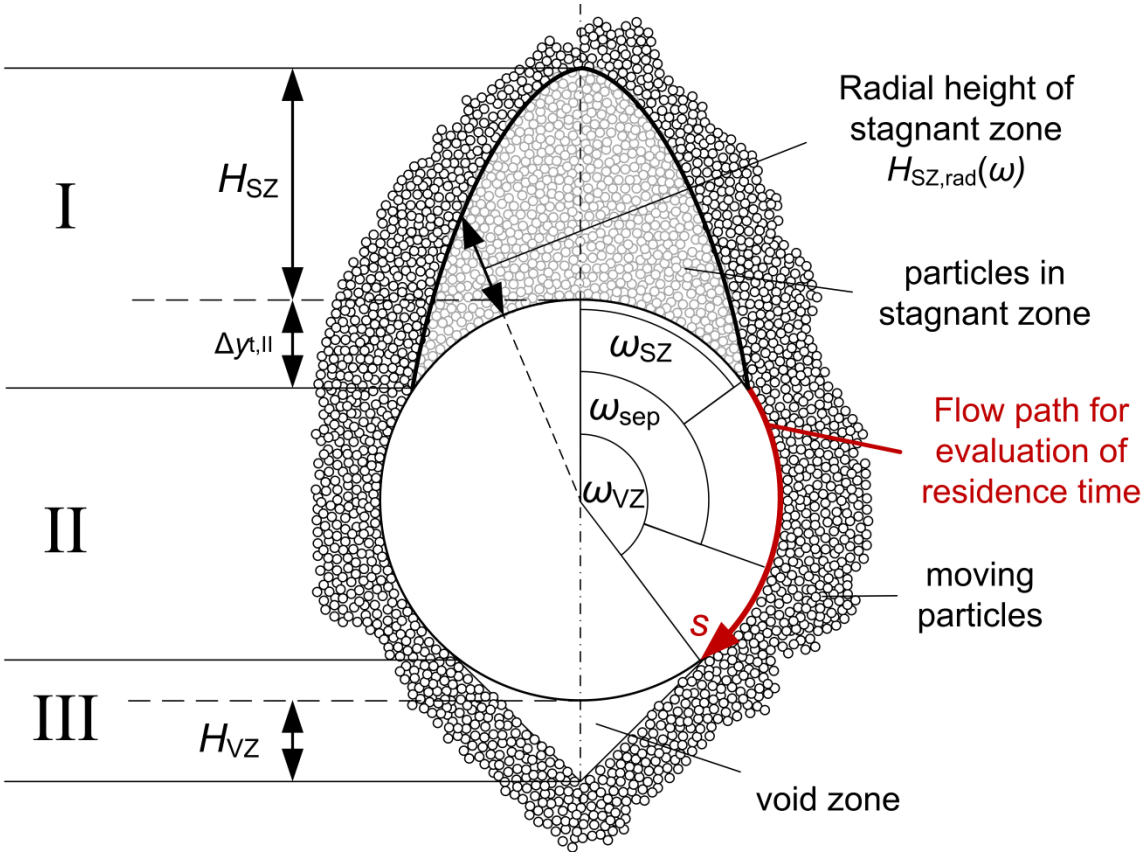

Figure 48. Schematic of flow field for enhanced model.

The radial height $H_{SZ,rad}(\omega)$ of the parabolic stagnant zone in the range of $0° \leq \omega \leq \omega_{SZ}$ is.

$$H_{\mathrm{rad,SZ}}(\omega) = \frac{\cos(\omega) - \sqrt{\cos^2(\omega) - 4a\,\sin^2(\omega)\,y_{\max}}}{2a\,\sin^2(\omega)} - \frac{D_T}{2} \tag{102}$$

This formulation cannot be integrated analytically. Alternatively, the shape of the stagnant zone can be approximated by a triangle instead of a parabola which is easier to integrate and leads to

$$\left(\frac{1}{\alpha_{\mathrm{SZ}}}\right)_{\mathrm{I,av}} = \frac{2}{\lambda_{\mathrm{S0}}\pi^2}\frac{1}{\Delta\omega}\left[\frac{2t\,\operatorname{arctanh}\left(\frac{m+\tan\left(\frac{\omega}{2}\right)}{\sqrt{m^2+1}}\right)}{\sqrt{m^2+1}} - \frac{D_T}{2}\omega\frac{\pi}{180°}\right]_0^{\omega_{\mathrm{SZ}}} \tag{103}$$

With

$$m = \frac{\frac{D_{\mathrm{T}}}{2}\cos(\omega_{\mathrm{SZ}}) - t}{\frac{D_{\mathrm{T}}}{2}\sin\left(\omega_{\mathrm{SZ}}\right)} \tag{104}$$

$$t = H_{\mathrm{SZ}} + \frac{D_{\mathrm{T}}}{2} \tag{105}$$

With equation (100), (101) and (103) the effective heat transfer coefficient in section I can be approximated using equation (58) (p. 92). With respect to the investigated configurations given in Table 1, the results deviate by up to 11 % from the exact solution of equation (56) (p. 91).

C.2 Section II

In section II the averaged heat transfer coefficient, $\alpha_{\mathrm{II,av}}$, is approximated by

$$\alpha_{\mathrm{II,av}} \approx \left(\left(\frac{1}{\alpha_{\mathrm{c}}}\right)_{\mathrm{II,av}} + \left(\frac{1}{\alpha_{\mathrm{S0}}}\right)_{\mathrm{II,av}}\right)^{-1} \tag{106}$$

The penetration resistance $(\alpha_{\mathrm{S0}})^{-1}$ (equation (48), p. 86) depends on the residence time t which again is a function of the average velocity $\bar{u}(\omega)$ (equation (55), p. 91) in the flow cross-section between the tubes. Therefore, to allow analytical integration of $(\alpha_{\mathrm{S0}})^{-1}$, a constant average flow speed, $u_{\mathrm{av,II}}$, is used in section II according to

$$u_{\mathrm{II,av}} = \frac{1}{\omega_{\mathrm{VZ}} - \omega_{SZ}}\int_{\omega_{\mathrm{SZ}}}^{\omega_{\mathrm{VZ}}} \bar{u}(\omega)d\omega \tag{107}$$

With $\bar{u}(\omega)$ according to equation (55) one gets:

$$u_{\mathrm{II,av}} = -\frac{u_{\mathrm{ref}} s_{\mathrm{H}}}{(\omega_{\mathrm{VZ}} - \omega_{\mathrm{SZ}})} \left[\frac{2 \arctan\left(\frac{D_{\mathrm{T}} - s_{\mathrm{H}} \tan\left(\frac{\omega}{2}\right)}{\sqrt{s_{\mathrm{H}}^2 - D_{\mathrm{T}}^2}} \right)}{\sqrt{s_{\mathrm{H}}^2 - D_{\mathrm{T}}^2}} \right]_{\omega_{\mathrm{SZ}}}^{\omega_{\mathrm{VZ}}} \tag{108}$$

The averaged penetration resistance in section II then can be calculated according to:

$$\left(\frac{1}{\alpha_{\mathrm{S0}}}\right)_{\mathrm{II,av}} = \frac{2}{3}\frac{1}{\Delta\omega}\sqrt{\frac{\pi D_{\mathrm{T}}}{2\left(\lambda\rho c_{\mathrm{p}}\right)_{\mathrm{S0}} u_{\mathrm{II,av}}}}\left((\omega_0 - \omega_{\mathrm{SZ}} + \omega'')^{\frac{3}{2}} - (\omega_0 - \omega_{\mathrm{SZ}} + \omega')^{\frac{3}{2}}\right) \tag{109}$$

With $\Delta\omega = \omega'' - \omega'$ being the considered angle range. ω_0 is the angle which corresponds to the residence time t_0 at the beginning of the considered row of tubes. For the first row of tubes t_0 is calculated according to equation (54) (p. 90). For the n-th row of tubes, ω_0 is

$$\omega_0 = \frac{2 t_0(n) u_{\mathrm{av}}}{D_{\mathrm{T}}} \frac{180°}{\pi} \tag{110}$$

The contact resistance, $(\alpha_{\mathrm{c}})^{-1}$ (equation (18), p.33), is constant in the range of $\omega_{\mathrm{SZ}} \leq \omega \leq \omega_{\mathrm{sep}}$. In the range of $\omega_{\mathrm{sep}} \leq \omega \leq \omega_{\mathrm{VZ}}$ it increases as the number of particles in touch with the tube surface decreases. The local ratio of the tube surface, covered with particles $\varphi(\omega)$ (see section 4.1.2.1) can be approximated using a *tanh*-function (see equation (71), p. 105). Alternatively, $\varphi(\omega)$ can be approximated by a simple linear profile:

$$\varphi(\omega) = \begin{cases} \varphi_0 & \text{for } \omega_{\mathrm{SZ}} \leq \omega \leq \omega_{\mathrm{sep}} \\ \dfrac{\varphi_0}{\omega_{\mathrm{sep}} - \omega_{\mathrm{VZ}}}(\omega - \omega_{\mathrm{VZ}}) & \text{for } \omega_{\mathrm{sep}} \leq \omega \leq \omega_{\mathrm{VZ}} \end{cases} \tag{111}$$

A value of $\varphi_0 = 0.65$ is used, according to Figure 26 (p. 60). For simplicity, the formulation of α_{c} is approximated as follows:

$$\alpha_c(\omega) = \varphi(\omega)\alpha_{\mathrm{WP}} - \big(1 - \varphi(\omega)\big)\alpha_{\mathrm{con}} + \alpha_{\mathrm{rad}} \approx \varphi(\omega)\alpha_{\mathrm{WP}} + \alpha_{\mathrm{con}} + \alpha_{\mathrm{rad}} \tag{112}$$

This simplification is justified as the heat transfer by conduction through the gas phase, α_{con}, is only relevant in case of $\varphi(\omega) \rightarrow 0$. In the rest of the cases, the dominating term is $(\varphi(\omega) \cdot \alpha_{WP})$.

The averaged contact resistance in section II is subsequently calculated:

For $\omega_{SZ} \leq \omega \leq \omega_{sep}$

$$\left(\frac{1}{\alpha_c}\right)_{II,av} = \frac{1}{\alpha_c(\varphi_0)} \tag{113}$$

For $\omega_{sep} \leq \omega \leq \omega_{VZ}$

$$\left(\frac{1}{\alpha_c}\right)_{II,av} = \frac{1}{\alpha_{WP}\varphi_0}\left[\ln|\alpha_{rad} + \alpha_{con} + \alpha_{WP}\varphi_0| - \ln|\alpha_{rad} + \alpha_{con}|\right] \tag{114}$$

With equation (109), (113) and (114) the effective heat transfer coefficient in section II can be approximated using equation (58) (p. 92). With respect to the investigated configurations given in Table 1, the results deviate by up to 7 % from the exact solution of equation (56) (p. 91).

C.3 Section III

In section III the average heat transfer coefficient, $\alpha_{III,av}$, is obtained directly, proceeding the same way as in section B.1. The *local* effective heat transfer coefficient at the end of section III (ω = 180°) is

$$\alpha_{III,loc}(\omega = 180°) = \left(\frac{1}{\alpha_{conv}(\omega = 180°)} + \frac{1}{\alpha_{S0}}\right)^{-1} \tag{115}$$

Where $\alpha_{conv}(\omega = 180°)$ is calculated according to equation (39) (p. 104) and α_{S0} is calculated using the residence time, t_{III}, at the end of section II. The *local* heat transfer coefficient at the beginning of section III (at the end of section II) is

$$\alpha_{III,loc}(\omega = \omega_{VZ}) = \left(\frac{1}{\alpha_c(\omega = \omega_{VZ})} + \frac{1}{\alpha_{S0}}\right)^{-1} \tag{116}$$

The contact heat transfer coefficient $\alpha_c(\omega = \omega_{VZ})$ is calculated using equation (18) (p. 33) with $\varphi = 0$. Given the local heat transfer coefficient, $\alpha_{III,loc}$, at the beginning and end of section III, it is interpolated linearly between the two values which means that the average heat transfer coefficient is

$$\alpha_{III,av} = \frac{\alpha_{III,loc}(\omega_{VZ}) + \alpha_{III,loc}(180°)}{2} \tag{117}$$

Appendix D: DEM model – sensitivity on different model parameters

In this chapter, the sensitivity of the simulation results of the discrete particle model on different model parameters is briefly investigated. Furthermore, additional details are given on the variation of the tube arrangement which has been addressed in sections 6.1.1 and 6.1.2.

D.1 Sensitivity to variation of Young's modulus

In the discrete particle model the Young's modulus of the particles is set to $E_p = 10^6$ N/m², which is about three orders of magnitude below the actual value of typical bulk materials. Here, a simulation with $E_p = 10^8$ N/m² is juxtaposed. As visible from Figure 49 the variation of the Young's modulus shows negligible influence on the simulation results.

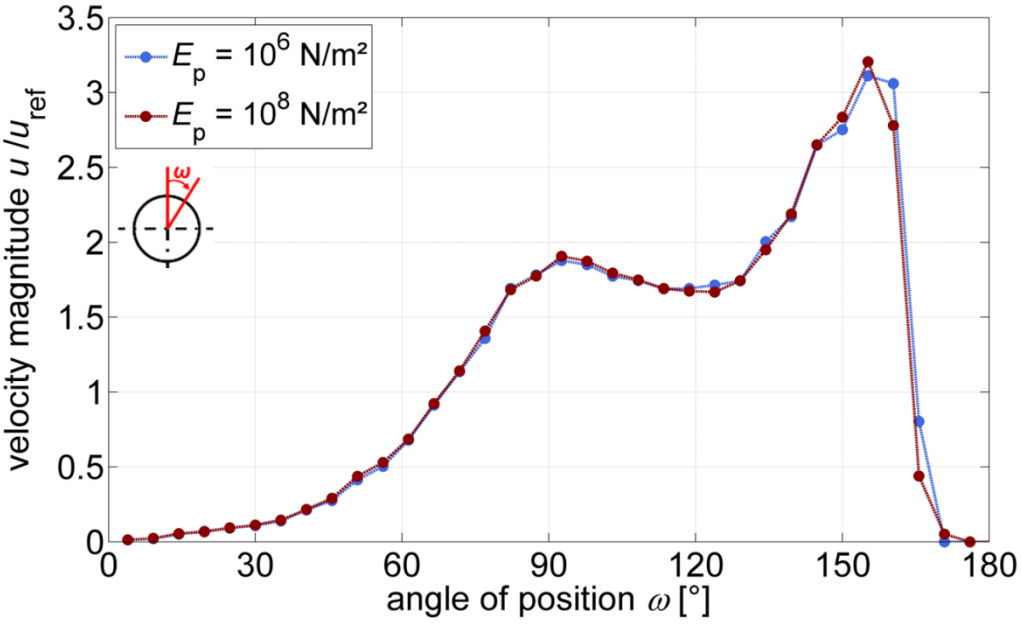

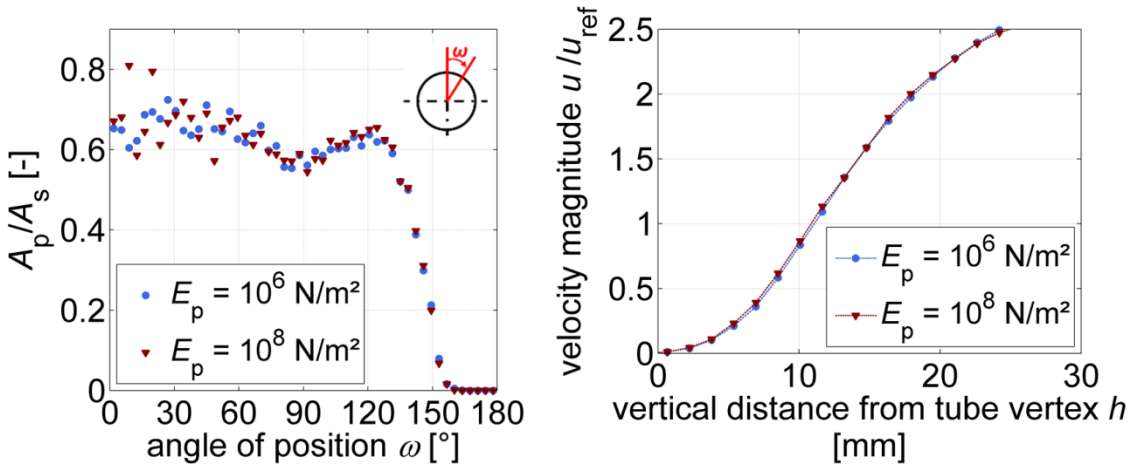

Figure 49. Influence of Youngs modulus, E_p, of the particles on the simulation results. Top: Velocity profile along the tube surface. Bottom left: Local share of tube surface covered by particles (see section 4.1.2.1). Bottom right: Velocity profile along vertical section above the tube (see Figure 24, p.57).

D.2 Sensitivity to variation of tube arrangement (supplement to section 6.1)

In section 6.1, amongst others, the influence of the tube arrangement on the flow pattern was investigated. The results were summarized in the form of contour plots in Figure 35 (p. 77) and Figure 39 (p. 82). Here, some more details are given on the variation of the tube arrangement. To this end, the horizontal spacing s_H is varied at a fixed vertical spacing of s_V = 50 mm (1.86·D_T) and the vertical spacing s_V is varied at a fixed horizontal spacing of s_H = 57 mm (2.12·D_T). For every arrangement three kinds of diagrams are shown:

- The plot of the flow speed along the tube surface
- The flow speed along the vertical profile above the tube
- The profile of local share of the tube surface covered with particles ($\varphi(\omega)$)

In Figure 50, the results of the variation of the horizontal spacing, s_H, are shown. The variation of s_H primarily influences the flow speed at the lateral sides of the tubes due to the varying flow cross-section between the tubes (Figure 50, top). The single symbols at $\omega = 90°$ show the hypothetical velocity at $\omega = 90°$, assuming plug-flow. The gap between the symbols and the corresponding graphs indicate that with decreasing s_H, the flow approaches plug-flow condition, which is conducive for the heat transfer.

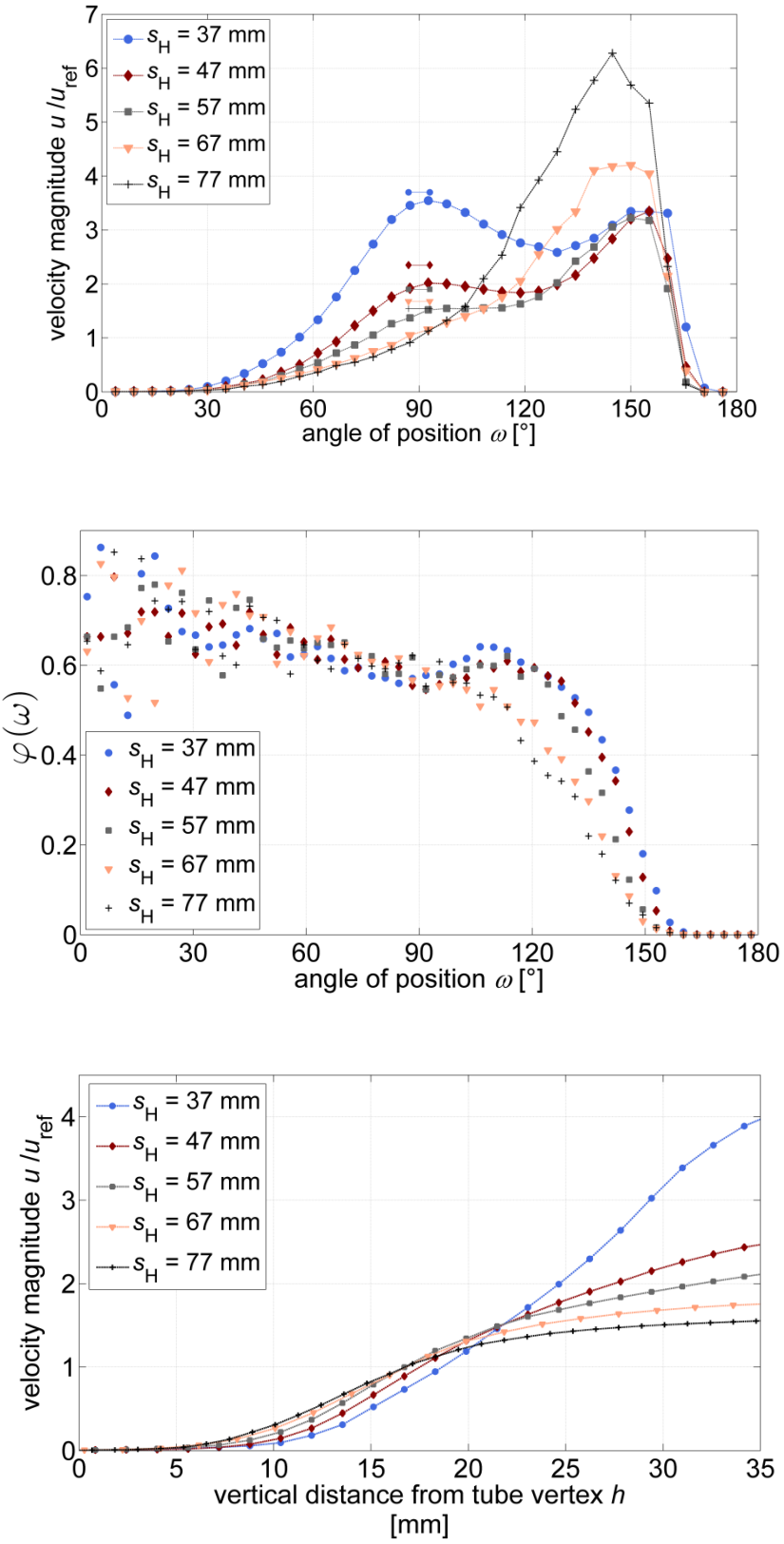

Figure 50. Variation of horizontal spacing s_H. Top: Velocity profile along the tube surface. Middle: $\varphi(\omega)$ at the tube surface. Bottom: Velocity profile along the vertical profile above the tube.

Figure 50 (middle) shows that with increasing s_H the particles tend to separate earlier from the tube surface (ω_{sep} is shifted to smaller values). The more ω_{sep} decreases, the larger is the flow speed in the lower part of the tube (Figure 50 (top)). This is because the earlier the particles detach themselves from the tube surface, the more time they have to accelerate along the slope.

The impact of s_H on the height of the stagnant zone is small (Figure 50, bottom). The height of the stagnant zone slightly increases with decreasing s_H.

In Figure 51, the results of the variation of the vertical spacing at intermediate s_V are shown. For very small vertical spacings, separate figures is given further below.

The variation of the vertical spacing shows little influence in the velocity profile at the tube surface Figure 51 (top). The extent of the stagnant zone remains approximately unaffected for all investigated cases. At very large s_V, the velocity profile approaches that of a single (solitary) tube (see plot 'Single Tube' in Figure 51 (top)). In this case, the plateau of flow speed around $\omega \approx 90°$ vanishes and the flow speed reaches maximum values below the tube.

Figure 51 (middle) shows, that with increasing s_V the particles tend to separate earlier from the tube surface (ω_{sep} is shifted to smaller values). Minimum values of $\omega_{sep} \approx 90°$-$100°$ are observed for large vertical spacings and for the single tube.

The impact of s_V on the size of the stagnant zone is very distinct (Figure 51, bottom). The size of the stagnant zone increases significantly with increasing s_V until a maximum height is reached. At even larger vertical spacings, the stagnant zone diminishes and approaches that of a single tube.

Figure 52 shows simulation results at very small values of s_V. The same results have been shown in the form of contour plots in section 6.1.1 (Figure 37). Here the corresponding profiles at the tube surface are given.

Figure 52 (top) shows that for very small values the extent of the stagnant zone reduces significantly. Likewise, the size of the stagnant zone reduces significantly as visible from Figure 52 (bottom). A tendency is observed, that the particles separate earlier from the tube surface at small vertical spacings (Figure 52 (middle). This effect, however, diminishes at smaller horizontal spacings as can be seen from the contour plot in Figure 39.

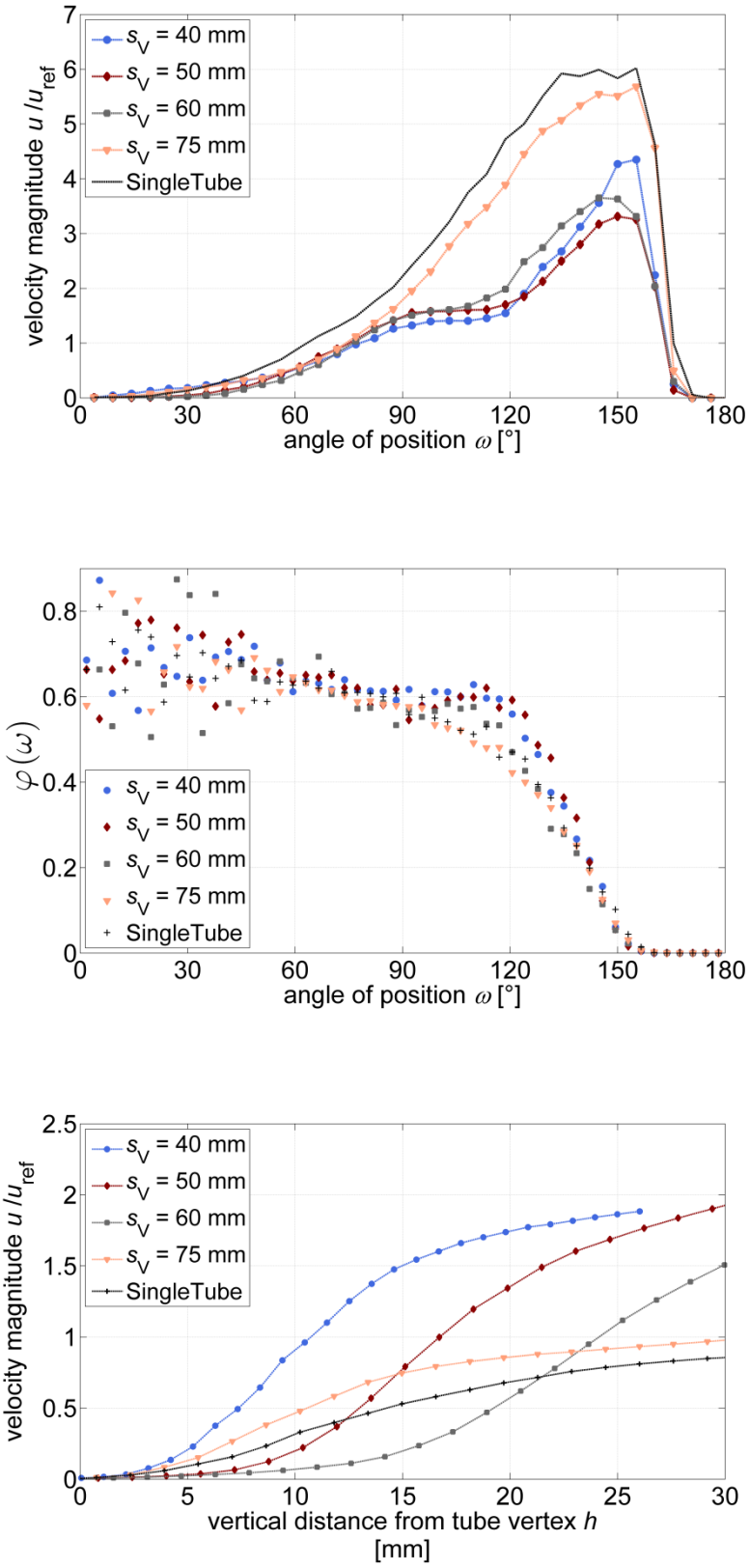

Figure 51. Variation of the vertical spacing s_V. Top: Velocity profile along the tube surface. Middle: $\varphi(\omega)$ at the tube surface. Bottom: Velocity profile along the vertical profile above the tube.

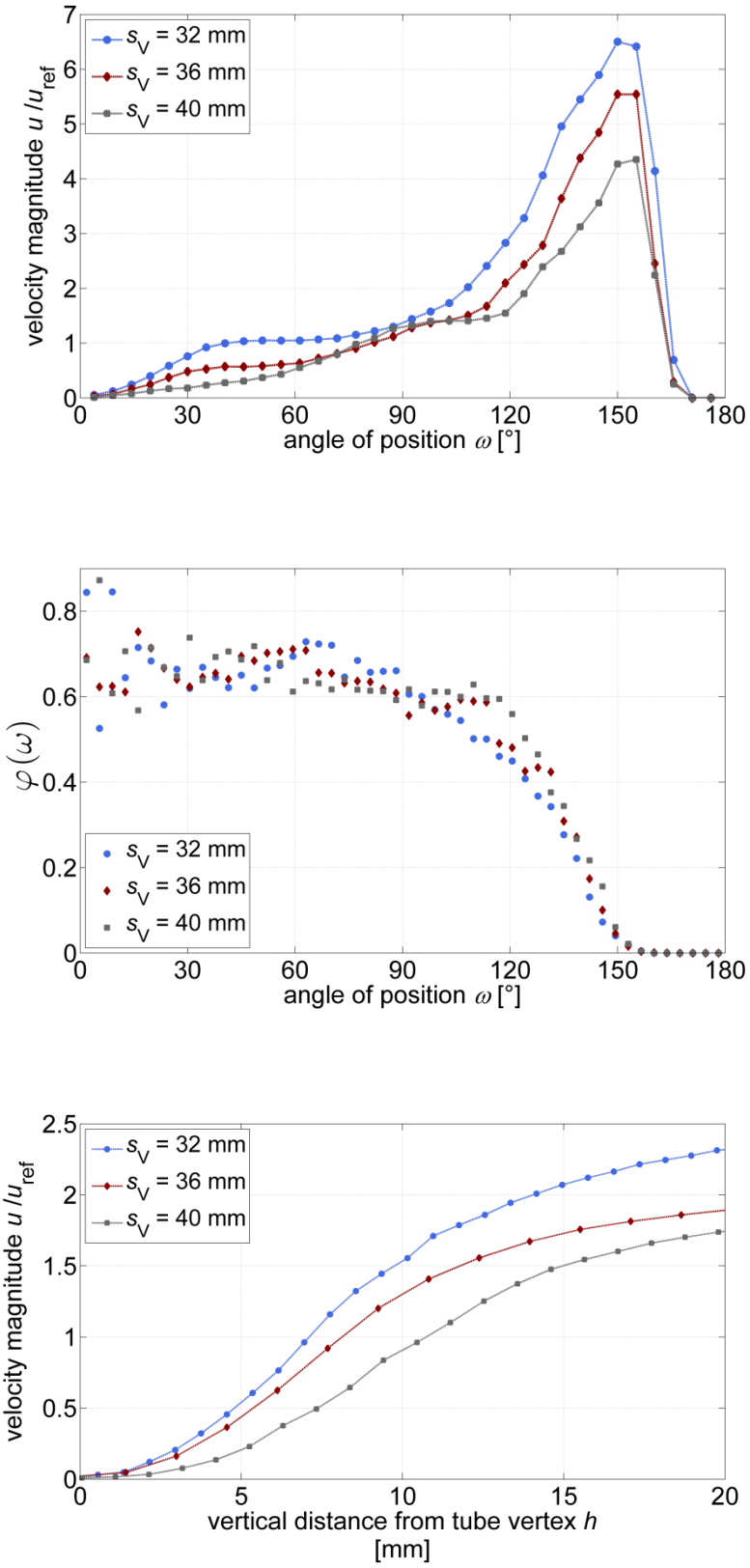

Figure 52. Variation of the vertical spacing, s_V, at very small values of s_V. Top: Velocity profile along the tube surface. Middle: $\varphi(\omega)$ at the tube surface. Bottom: Velocity profile along the vertical profile above the tube.

D.3 Sensitivity to variation of inner friction angle (supplement to section 6.1)

In section 6.1 it was stated that the inner friction angle, ϕ_i, does not influence the size and extent of the stagnant zone. In Figure 53 the corresponding velocity profiles are shown. Influence of the inner friction angle is only observed in the lower part of the tube. This influence has been discussed in section 6.1. In the upper part of the tube and in the stagnant zone the simulation results are insensitive to ϕ_i.

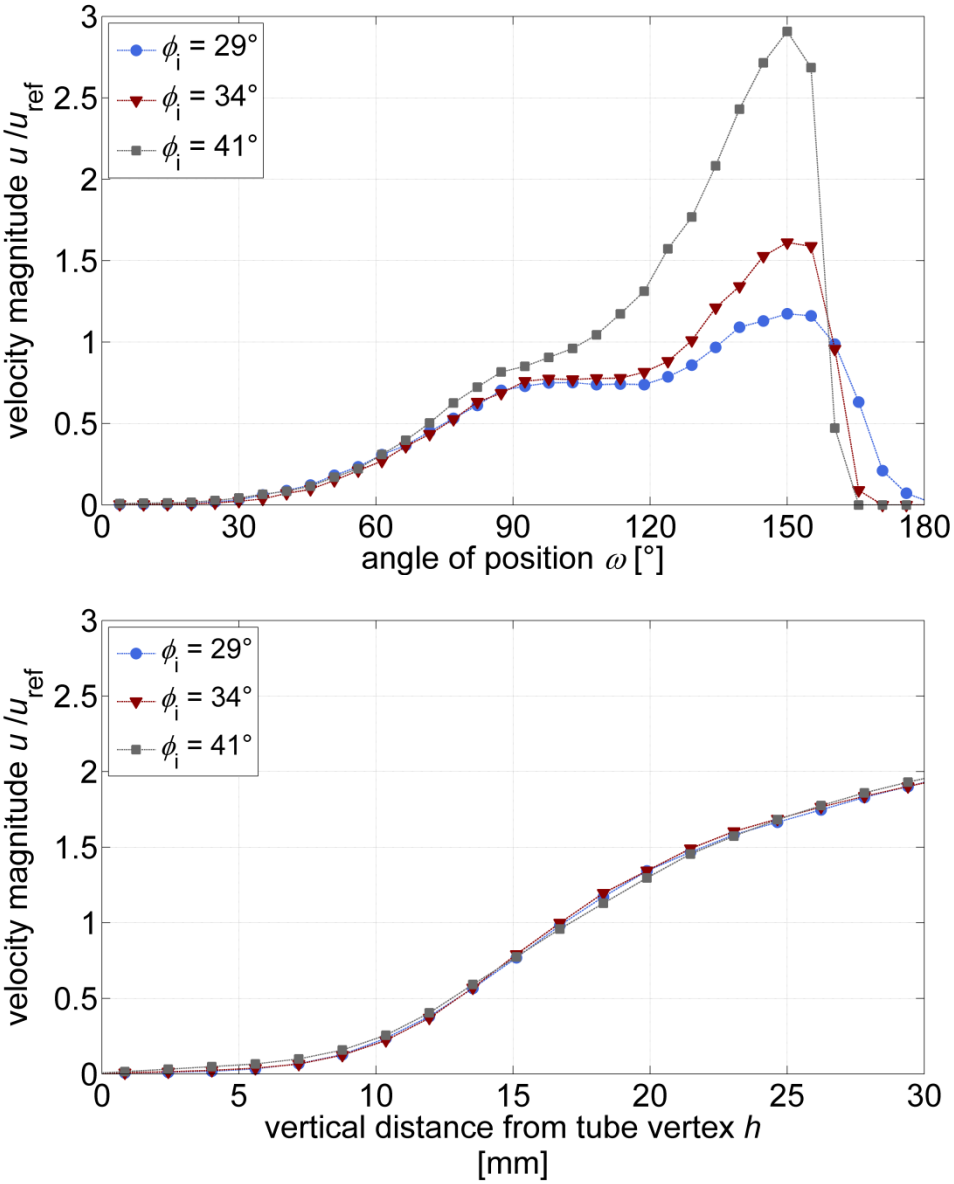

Figure 53. Variation of the inner friction angle ϕ_i. Top: Velocity profile along the tube surface. Bottom: Velocity profile along the vertical profile above the tube.

D.4 Sensitivity to variation of internal friction parameters

The calibration procedure of the inner friction coefficients of the bulk, μ_{pp} and μ_{roll}, is described in section 4.3.2. The procedure was as follows: The inter-particle coefficient of friction μ_{pp} was set according to measurement data from literature [109]. The rolling friction coefficient was calibrated afterwards such that the measured static angle of repose of $\phi_r \approx 34°$ was attained. This lead to $\mu_{pp} = 0.2$ and $\mu_{roll} = 0.3$.

In this section the sensitivity of the simulation results on a variation of the friction coefficients is tested. Three combinations of μ_{pp} and μ_{roll} are compared which all yield $\phi_r \approx 34°$. For $\mu_{pp} < 0.2$ it was not possible to obtain $\phi_r \approx 34°$ which is in accordance with the results of Derakhshani et al. [116]. The three combinations are given in Table 5.

Table 5. Tested combinations of inner friction coefficients, μ_{pp} and μ_{roll}, which yield an angle of repose of $\phi_r \approx 34°$.

Inter-particle coefficient of friction μ_{pp}	Rolling friction coefficient μ_{roll}
0.2	0.3
0.3	0.15
0.4	0.1

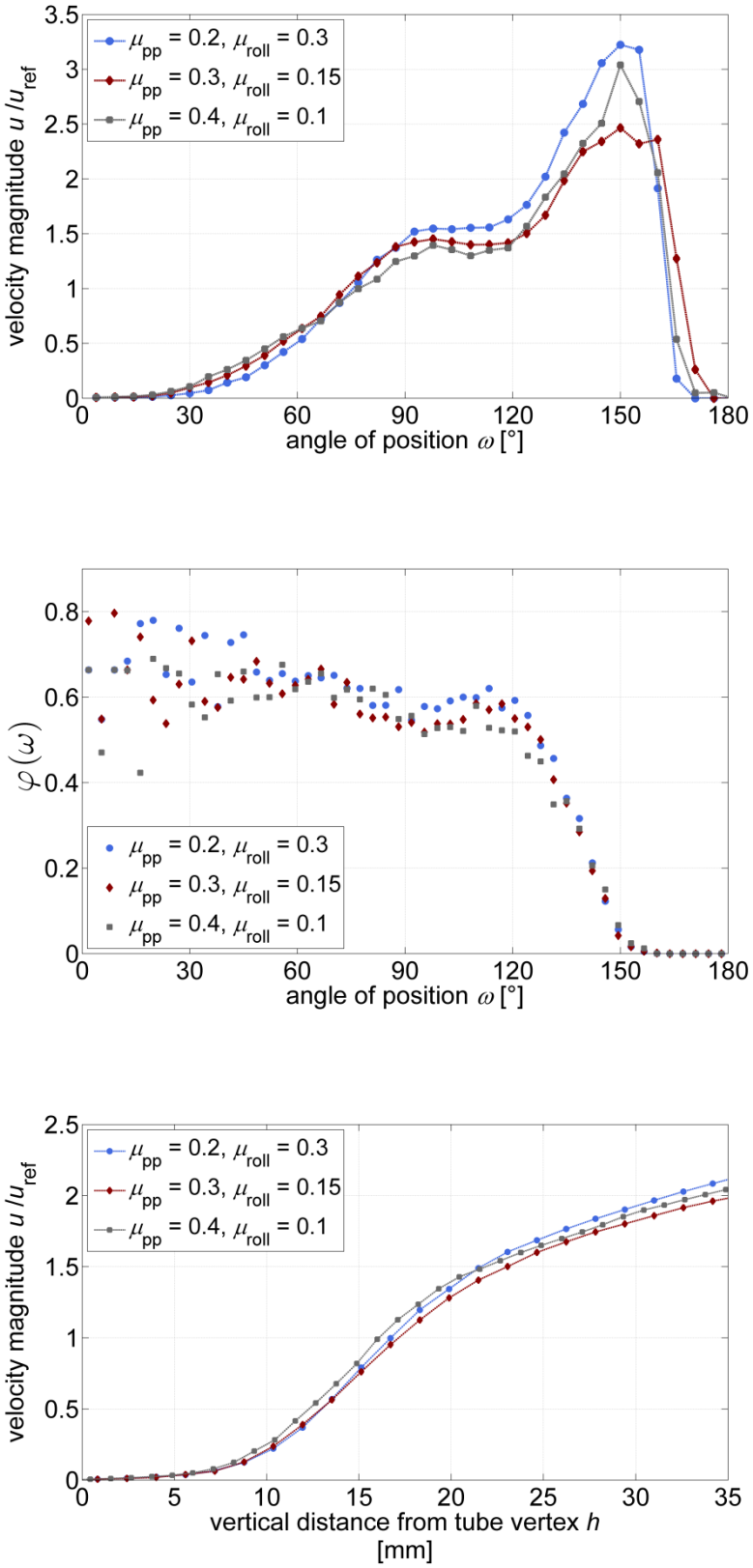

Figure 54. Variation of the inner friction coefficients μ_{pp} and μ_{roll} at constant repose angle ϕ_r. Top: Velocity profile along the tube surface. Middle: $\varphi(\omega)$ at the tube surface. Bottom: Velocity profile along the vertical profile above the tube.

The results are shown in Figure 54. Minor influence is observed regarding the velocity profile at the tube surface (Figure 54, top). With increasing μ_{pp} (decreasing μ_{roll}) the velocity at the lateral sides of the tube slightly decreases and the transition from the stagnant to the flowing regime becomes more continuous. The magnitude of the flow speed in the lower half of the tube decreases with increasing μ_{pp} (decreasing μ_{roll}).

Figure 54 (middle) and Figure 54 (bottom) show, that the variation of the friction coefficients shows only very small influence on the size of the stagnant area and on the position at which the particles start to separate from the tube surface (ω_{sep}).

To conclude, the most relevant simulation results (H_{SZ}, ω_{SZ}, ω_{sep}, ω_{VZ}) are relatively insensitive to the variation of the inner friction coefficients μ_{pp} and μ_{roll}, provided that the static angle of repose is retained.

D.5 Sensitivity to variation of the reference velocity

In this work $u_{ref} = 5.0$ mm/s has been used for all DEM-simulations. The following diagrams show that at reference (inlet) velocities of this order, the simulation results are virtually independent of the reference velocity.

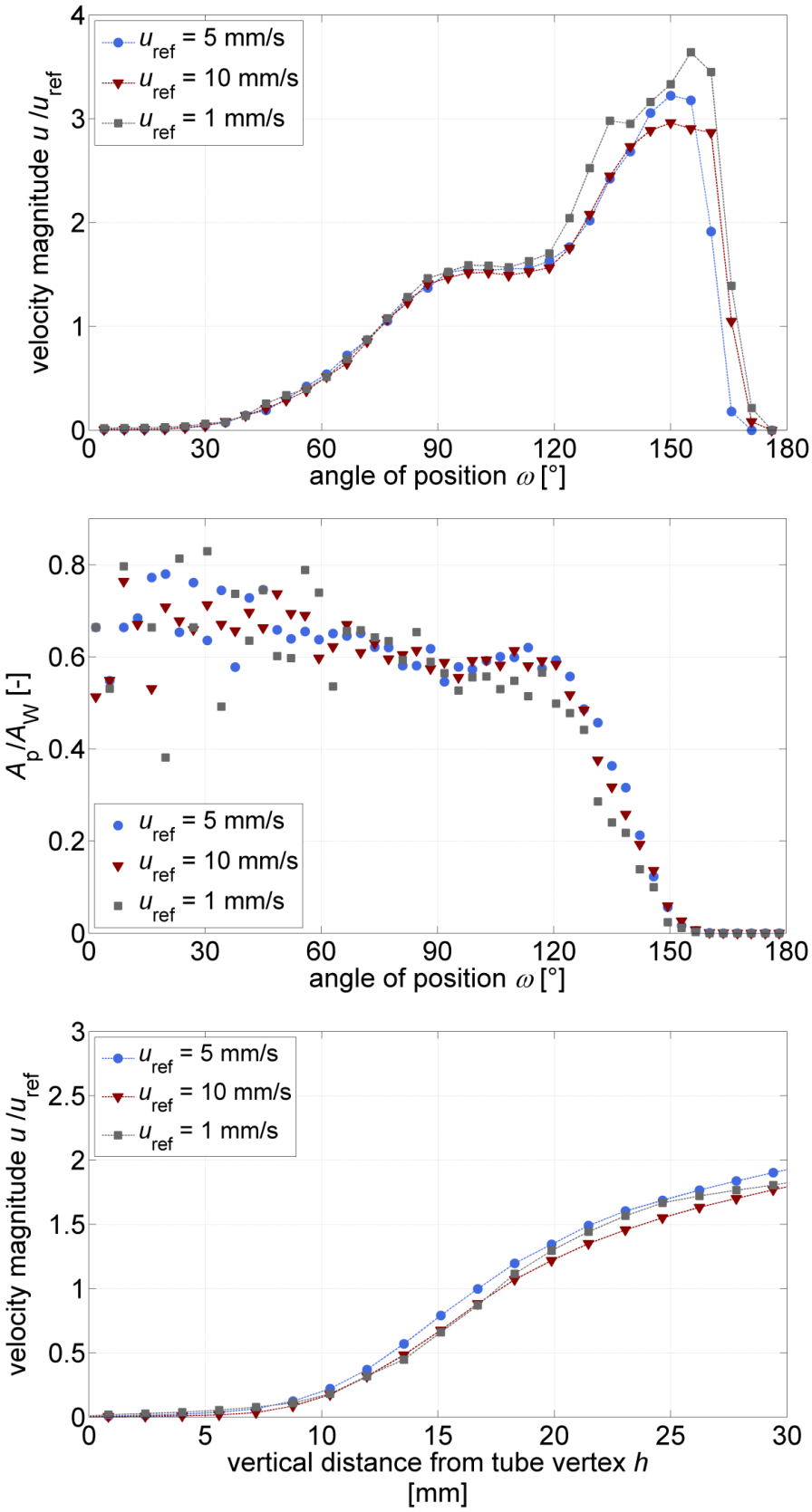

Figure 55. Variation of the of the reference velocity (inlet velocity). Top: Velocity profile along the tube surface. Middle: $\varphi(\omega)$ at the tube surface. Bottom: Velocity profile along the vertical profile above the tube.

References

[1] T. Baumann, *Wärmeauskopplung aus heißen Partikelschüttungen zur Dampferzeugung,* Stuttgart: Stuttgart University, 2014.

[2] J. Niegsch et al., "Heat transfer and flow of bulk solids in a moving bed," *Chemical Engineering and Processing,* vol. 33, pp. 73-89, 1994.

[3] E.-U. Schlünder and E. Tsotsas, Wärmeübertragung in Festbetten, durchmischten Schüttgütern und Wirbelschichten, Stuttgart; New York: Thieme, 1988.

[4] P. Bartsch and S. Zunft, "Granular flow around the horizontal tubes of a particle heat exchanger: DEM-simulation and experimental comparison," *Solar Energy,* vol. 182, pp. 48-56, 2019.

[5] P. Bartsch and S. Zunft, "Numerical investigation of dense granular flow around horizontal tubes: Qualification of CFD model with validated DEM model," *Solar Energy,* vol. 182, pp. 298-303, 2019.

[6] "World Energy Outlook 2007 - Executive Summary," International Energy Agency (IEA), 2017.

[7] H. J. Schellenhuber, D. Messner and C. Leggewie et al., "Kassensturz für den Weltklimavertrag - Der Budgetansatz," Wissenschaftlicher Beirat der Bundesregierung Globale Umweltveränderungen (WBGU), Berlin, 2009.

[8] V. Dreissigacker, "Power-to-heat in adiabatic compressed air energy storage power plants for cost reduction and increased flexibility," *Heat and Mass Transfer,* vol. 54, pp. 955-962, 2018.

[9] K. Stahl, M. Siebert and S. Kessler et al., "Flexibilisierung von Gas- und Dampfturbinenkraftwerken durch den Einsatz von Hochtemperature-Wärmespeichern (FleGs)," 2012. [Online]. Available: https://www.tib.eu/de/suchen/download/?tx_tibsearch_search%5Bdocid%5D=TIBKAT%3A780045068&cHash=807994068447a7421c09d328fd4541cf#download-mark. [Accessed August 2018].

[10] A. Gil, M. Medrano and I. Martorell et al., "State of the art on high temperature thermal energy storage for power generation. Part 1 - Concepts, materials and modellization," *Renewable and Sustainable Energy Reviews,* vol. 14, pp. 31-55, 2010.

[11] S. Kuravi, J. Trahan and D. Y. Goswami et al., "Thermal energy storage technologies and systems for concentrating solar power plants," *Progress in Energy and Combustion Science,* pp. 285-319, 2013.

[12] P. K. Falcone, J. E. Noring and C. E. Hackett, "Evaluation and application of solid thermal energy carriers in a high temperature solar central receiver system," in *IECED '82; Proceedings of the Seventeenth Intersociety Energy Conversion Engineering Conference*, Los Angeles, 1982.

[13] J. M. Hruby, B. R. Steele and V. P. Burolla, "Solid particle receiver experiments: radiant heat test," US Department of Energy, N. p., 1984.

[14] B. Gobereit, *Theoretische und experimentelle Untersuchung zur Weiterentwicklung von solaren Partikelreceivern,* Berlin: Logos Verlag, 2015.

[15] T. Baumann and S. Zunft, "Properties of granular materials as heat transfer and storage medium in CSP application," *Solar Energy Materials and Solar Cells,* vol. 143, pp. 38-47, 2015.

[16] T. Baumann, S. Zunft and R. Tamme, "Moving Bed Heat Exchangers for Use With Heat Storage in Concentrating Solar Plants: A Multiphase Model," *Heat Transfer Engineering,* vol. 35, pp. 224-231, 2014.

[17] B. Andreotti et al., Granular Media - Between Fluid and Solid, Cambridge: Cambridge University Press, 2013.

[18] H. G. Matuttis, S. Luding and H. J. Herrmann, "Discrete element simulations of dense packings and heaps made of spherical and non-spherical particles," *Powder Technology,* vol. 109, pp. 278-292, 2000.

[19] S. Luding, M. Lätzel and W. Volk et al., "From discrete element simulations to a continuum model," *Computer Methods in Applied Mechanics and Engineering,* vol. 191, pp. 21-28, 2001.

[20] P. A. Cundall and O. D. L. Strack, "A discrete numerical model for granular assemblies," *Géothechnique,* vol. 29, pp. 47-65, 1979.

[21] B. Alder and T. Wainwright, "Studies in Molecular Dynamics. I. General Method," *The Journal of Chemical Physics,* vol. 31, pp. 459-466, 1959.

[22] J. Baxter, U. Tüzün and J. Burnell, "Granular dynamics simulations of two-dimensional heap formation," *Physical Review E,* vol. 55, pp. 3546-3554, 1997.

[23] M. Lätzel, *From microscopic simulations towards a macroscopic description of granular media,* Stuttgart University, 2003.

[24] J. Lee and H. Herrmann, "Angle of repose and angle of marginal stability: molecular dynamics of granular particles," *Journal of Physics A: Mathmatical and General,* vol. 26, pp. 373-383, 1993.

[25] O. R. Walton and R. L. Braun, "Viscosity, granular-temperature, and stress calculations for shearing assemblies of inelastic, frictional disks," *Journal of Rheology,* vol. 30, pp. 949-980, 1986.

[26] H. Kruggel-Emden, S. Wirtz and V. Scherer, "Applicable Contact Force Models for the Discrete Element Method: The Single Particle Perspective," *Journal of Pressure Vessel Technology,* vol. 131, pp. 024001-1-11, 2009.

[27] P. Knödler, "Thermo-Mechanical Investigations of Packed Beds for High Temperature Heat Storage: Uniaxial Compression Test Experiments and Particle Discrete Simulations," *Applied Science,* vol. 9, pp. 1600-1-11, 2019.

[28] M. Van Zeebroeck, E. Tijskens and E. Dintwa et al., "The discrete element method (DEM) to simulate fruit impact damage during transport and handling: Case study of vibration damage during apple bulk transport," *Postharvest Biology and Technology,* vol. 41, pp. 92-100, 2006.

[29] W. R. Ketterhagen, M. T. Am Ende and B. C. Hancock, "Process Modeling in the Pharmaceutical Industry using the Discrete Element Method," *Journal of Pharmaceutical Science,* vol. 98, pp. 442-470, 2009.

[30] M. Paulick, M. Morgeneyer and A. Kwade, "Review on the influence of elastic particle properties on DEM simulation results," *Powder Technology,* vol. 283, pp.

66-76, 2015.

[31] Z. Zhou, H. Zhu and A. Yu et al., "Discrete Particle Simulation of Solid Flow in a Model Blast Furnace," *ISIJ International,* vol. 45, pp. 1828-1837, 2005.

[32] V. Dreissigacker, S. Zunft and H. Müller-Steinhagen, "A thermo-mechanical model of packed-bed storage and experimental validation," *Applied Energy,* vol. 111, pp. 1120-1125, 2013.

[33] B. D. Lubachevsky, "How to Simulate Billiards and Similar Systems," *Jorunal of computational physics,* vol. 94, pp. 255-283, 1991.

[34] H. Herrmann and S. Luding, "Modeling granular media on the computer," *Continuum Mechanics and Thermodynamics,* vol. 10, pp. 189-231, 1998.

[35] M. J. V. Goldschmidt, R. Beetstra and J. Kuipers, "Hydrodynamic modelling of dense gas-fluidised beds: Comparison of the kinetic theory of granular flow with 3D hard-sphere discrete particle simulations," *Chemical Engineering Scinece,* vol. 57, pp. 2059-2075, 2002.

[36] S. Luding, E. Clément, A. Blumen and e. al., "Studies of columns of beads under external vibrations," *Physical Review E,* vol. 49, pp. 1634-1646, 1994.

[37] J. J. Moreau, "New computaion methods in granular dynamics," *Powders & Grains,* vol. 93, pp. 227-232, 1993.

[38] M. Jean, "The non-smooth contact dynamics method," *Computer Methods and Applied Mechanics and Engineering,* vol. 177, pp. 235-257, 1999.

[39] F. Radjai and V. Richefeu, "Contact dynamics method," *European Journal of Environmental and civil engineering,* vol. 12, pp. 871-900, 2008.

[40] P.-Y. Lagrée, L. Satron and S. Popinet, "The granular column collapse as a continuum: validity of a two-dimensional Navier Stokes model with a μ(I)-rhoelogy," *Journal of Fluid Mechanics,* vol. 686, pp. 378-408, 2011.

[41] J. Fortin and P. Coorevits, "Selecting contact particle dynamics granular mechanis systems," *Journal of Computational and Applied Mathematics,* vol. 168, pp. 207-213, 2004.

[42] K.-W. Lim, K. Krabbenhoft and J. E. Andrade, "A contact dynamics approach to the Granular Element Method," *Computer Methods in Applied Engineering,* vol. 268, pp. 557-573, 2014.

[43] L. Brendel, T. Unger and D. E. Wolf, "Contact Dynamics for Beginners," in *The Physics of Granular Media*, Weinheim, Wiley Verlag, 2004, pp. 325-343.

[44] W. Siu and S.-K. Lee, "Transient temperature computation of spheres in three-dimensional random packings," *International Jounal of Heat and Mass Transfer,* vol. 47, pp. 887-898, 2004.

[45] Y. Feng, K. Han and C. Li et al., "Discrete thermal element modelling of heat conduction in particle systems: Basic formulations," *Journal of Computational Physics,* vol. 227, pp. 5072-5089, 2008.

[46] G. Cheng, A. Yu and P. Zulli, "Evaluation of effective thermal conductivity from the structure of a packed bed," *Chemical Engineering Science,* vol. 54, pp. 4199-4209, 1999.

[47] W. L. Vargas and J. McCarthy, "Heat Conduction in Granular Materials," *AIChE Journal,* vol. 47, pp. 1052-1059, 2001.

[48] K. K. Rao and P. R. Nott, An Introduction to Granular Flow, Cambridge: Cambridge University Press, 2008.

[49] I. Goldhirsch, "Rapid Granular Flows," *Annual Review of Fluid Mechanics,* vol. 35, pp. 267-293, 2003.

[50] D. Gidaspow et al., "Hydrodynamics of circualting fluidized beds: Kinetic theory approach," in *7th Fluidization Conference*, 1992.

[51] J. H. Atkinson and P. L. Bransby, The Mechanics of Soil: An Introduction to Critical State Soil Mechanics, England: McGraw-Hill, 1978.

[52] A. Schofield and P. Wroth, Critical State Soil Mechanics, New York: McGraw-Hill, 1968.

[53] E. Mase, Theory and Problems of Continuum Mechanics, New York: McGraw-Hill Book Company, 1970.

[54] I. Gildhirsch and C. Goldenberg, "Static Properties," in *The Physics of Granular Media*, Weinheim, Wiley Verlag, 2004, pp. 1-22.

[55] D. Drucker and W. Prager, "Soil mechanics and plastic analysis of limit design," *Quarterly of Applied Mathematics,* vol. 10, pp. 157-165, 1952.

[56] G. Tardos, "A fluid mechanistic approach to slow, frictional flow of powders," *Powder Technology,* vol. 92, pp. 61-74, 1997.

[57] S. Dartevelle, "Numerical modeling of geophysical granular flows: 1. A comprehensive approach to granular rheologies and geophysical multiphase flows," *Geochemistry Geophysics Geosystems,* vol. 5, pp. 1-28, 2004.

[58] S. A. Elaskar, L. A. Godoy and D. D. Gray et al., "A viscoplastic approach to model the flow of granular solids," *International Journal of Solids and Structures,* vol. 37, pp. 2185-2214, 2000.

[59] J. R. Prakash and K. K. Rao, "Steady compressible flow of granular materials through a wedge-shaped hopper: the smooth wall, radial gravity problem," *Chemical Engineering Science,* vol. 43, pp. 479-494, 1988.

[60] R. de Borst, "Simulation of strain localization: A reapraisal of the cosserat continuum," *Engineering Computations,* vol. 8, pp. 317-332, 1991.

[61] D. Kolymbas, "An outline of hypoplasticity," *Archive of Applied Mechanics,* vol. 61, pp. 143-151, 1991.

[62] D. Mašín, "A hypoplastic constitutive model for clays," *International Journal for Numerical and Analytical Methods in Geomechanics,* vol. 29, p. 311–336, 2005.

[63] A. Srivastava and S. Sundaresan, "Analysis of a frctional-kinetic model for gas-particle flow," *Powder Technology,* vol. 129, pp. 72-85, 2003.

[64] S. Benyahia, "Validation of Two Continuum Granular Frictional Flow Theories," *Industrial & Engineering Chemistry Research,* vol. 47, pp. 8926-8932, 2008.

[65] S. Pudasaini, "A general two-phase debris flow model," *Journal of Geophysical Research,* vol. 117, pp. F03010-1-28, 2012.

[66] S. Nick, A. Tilliander, T. L. I. Jonsson and e. al., "Matematical Model of Solid

Flow Behavior in a Real Dimension Blast Furnace," *ISIJ International,* vol. 53, pp. 979-987, 2013.

[67] H. Norem, F. Irgens and B. Schieldrop, "A continuum model for calculating snow analanche velocities," in *Avanlanche Formation, Movement and Effects (Proceedings of the Davos Symposium, September 1987)*, Davos, 1987.

[68] P. C. Johnson and R. Jackson, "Frictional-collisional constitutive relations for granular materials, with application to plane shearing," *Journal of Fluid Mechanics,* vol. 176, pp. 67-93, 1986.

[69] I. S. Aranson and L. S. Tsimring, "Continuum theory of partially fluidized granular flows," *Physical Review E,* vol. 65, 2002.

[70] P. Jop et al., "A consititutive law for dense granular flows," *nature,* vol. 441, pp. 727-730, 2006.

[71] S. B. Savage, "Analyses of slow high-concentration flows of granular materials," *Journal of Fluid Mechanics,* vol. 377, pp. 1-26, 1998.

[72] M. Syamlal, W. Rogers and T. J. O'Brien, *MFIX Documentation Theory Guide,* Morgantown: U.S. Dept. of Energy, Office of Fossil Energy, Tech. Note, 1993.

[73] S. Yagi and D. Kunii, "Studies on Effective Thermal Conductivities in Packed Beds," *A.I.Ch.E. Journal,* vol. 3, pp. 373-381, 1957.

[74] A. J. Slavin, V. Arcas and C. A. Greenhalgh et al., "Theoretical model for the thermal conductivity of a packed bed of solid spheroids in the presence of a static gas, with no adjustable parameters except at low pressure and temperature," *International Journal of Heat and Mass Transfer,* vol. 45, pp. 4151-4161, 2002.

[75] M. Bahrami, M. M. Yovanovich and J. R. Culham, "Effective thermal conductivity of rough spherical packed beds," *International Journal of Heat and Mass Transfer,* vol. 49, pp. 3691-3701, 2006.

[76] M. Colakyan and O. Levenspiel, "Heat Transfer between Moving Bed of Solids and Immersed Cylinders," *AIChE Symposium Series,* vol. 80, pp. 156-168, 1984.

[77] N. S. Obuskovic, *Heat Transfer Between Moving Beds of Solids and a Vertical Tube,* Oregon State University, 1988.

[78] J. Kuipers, W. Prins and W. van Swaaij, "Numerical Calculations of Wall-to-Bed Heat-Transfer Coefficients in Gas-Fluidized Beds," *AIChE Journal,* vol. 39, pp. 1079-1091, 1992.

[79] M. Syamlal and D. Gidaspow, "Hydrodynamics of Fluidization: Prediction of Wall to Bed Heat Transfer Coefficients," *AIChE Journal,* vol. 31, pp. 127-135, 1985.

[80] H. S. Mickley and D. F. Fairbanks, "Mechanism of Heat Transfer to Fluidized Beds," *A.I.Ch.E. Journal,* vol. 1, pp. 374-384, 1955.

[81] R. Ernst, "Wärmeübergang an Wärmetrauschern im Moving Bed," *Chemie Ingenieur Technik,* vol. 32, pp. 17-22, 1960.

[82] A. P. Baskakov, "The mechanism of heat transfer between a fluidized bed and a surface," *Int. Chem. Eng.,* vol. 4, p. 320, 1964.

[83] E. U. Schlünder, "Wärmeübergang an bewegten Kugelschüttungen bei kurzfristigem Kontakt," *Chemie Ingenieur Technik,* vol. 43, pp. 651-654, 1971.

[84] A. O. O. Denloye and J. S. M. Botterill, "Heat Transfer in Flowing Packed Beds," *Chemical Engineering Science,* vol. 32, pp. 461-465, 1977.

[85] W. N. Sullivan and R. H. Sabersky, "Heat transfer to flowing granular media," *International Journal of Heat and Mass Transfer,* vol. 18, pp. 97-107, 1975.

[86] J. Niegsch, *Schüttgutbewegung und Wärmeübergang im Wanderbett,* Dortmund University, 1993.

[87] N. Obuskovic, M. Colakyan and J. G. Knudsen, "Heat Transfer Between Moving Beds of Solids and a Transverse Finned Tube," *Heat Transfer Engineering,* vol. 12, pp. 46-52, 1991.

[88] H. Al-Ansary, A. El-Leathy and Z. Al-Suhaibani et al., "Experimental Study of a Sand-Air Heat Exchanger for Use With a High-Temperature Solar Gas Turbine Systems," *Journal of Solar Energy Engineering,* vol. 134, pp. 041017-1-7, 2012.

[89] H. Takeuchi, "Particles Flow Pattern and Local Heat Transfer Around Tube in Moving Bed," *AIChE Journal,* vol. 42, pp. 1621-1626, 1996.

[90] W.-S. Lee, S.-K. Youn and S.-I. Park, "Finite element analysis of the flow and heat transfer of solid particles in moving beds," *International Journal of Energy Research,* vol. 22, pp. 1145-1155, 1998.

[91] T. Baumann and S. Zunft, "Developement and performance assessment of a moving bed heat exchanger for solar central receiver power plants," *Energy Procedia,* vol. 69, pp. 748-757, 2015.

[92] D. A. Steingart and J. W. Evans, "Measurements of granular flows in two-dimensional hoppers by particle image velocimetry. Part I: experimental method and results," *Chemical Engineering Science,* vol. 60, pp. 1043-1051, 2005.

[93] R. J. Adrain and J. Westerweel, Particle Image Velocimetry, Cambridge: Cambridge University Press, 2011.

[94] S. Schneiderbauer et al., "A comprehensive frictional-kinetic model for gas-particle flows: Analysis of fluidized and moving bed regimes," *Chemical Engineering Science,* vol. 80, pp. 279-292, 2012.

[95] M. Ishii, Thermo-fluid dynamic theory of two-phase flow, Paris: Eyrolles, 1975.

[96] D. Gunn, "Transfer of heat and mass to particles in figed and fluidised beds," *International Journal of Heat and Mass Transfer,* vol. 21, pp. 467-476, 1978.

[97] R. Jackson, "Some Mathematical and Physical Aspects of Continuum Models for the Motion of Granular Materials," *Theory of Dispersed Multiphase Flow,* pp. 291-337, 1983.

[98] B. G. M. van Wachem et al., "Comparative Analysis of CFD Models of Dense Gas-Solid Systems," *AIChE Journal,* vol. 47, pp. 1035-1051, 2001.

[99] P. C. Johnson et al., "Frictional-collisional equations of motion for particulate flows and their application to chutes," *Journal of Fluid Mechanics,* vol. 210, pp. 501-535, 1990.

[100] D. G. Schaeffer, "Instability in the Evolution Equations Describing Incompressible Granular Flow," *Journal of Differential Equations,* vol. 66, pp. 19-50, 1987.

[101] H. Kruggel-Emden, E. Simsek, S. Rickelt, S. Wirtz and V. Scherer, "Review and

extension of normal force models for the Discrete Element Methode," *Powder Technology,* vol. 171, pp. 157-173, 2006.

[102] ESSS - Engineering Simulation and Scientific Software, *Technical Manual Rocky 4, DEM Particle Simulator,* ESSS Rocky, 2017.

[103] C. M. Wensrich and A. Katterfeld, "Rolling friction as a technique for modelling particle shape in DEM," *Powder Technology,* vol. 217, pp. 409-417, 2012.

[104] R. Span, "Stoffwerte von Luft," in *VDI-Wärmeatlas*, 10 ed., Verein Deutscher Ingenieure, VDI Gesellschaft Verfahrentechnik und Chmieingenieurwesen (GVC), 2006.

[105] "Merkblatt 984, Rauheitsmaße bei Oberflächen von nichtrostendem Stahl," 2016. [Online]. Available: https://www.edelstahl-rostfrei.de/downloads/iser/MB_984_Rauheitsmasse.pdf. [Accessed 13th June 2018].

[106] C. J. Coetzee, "Review: Calibration of the discrete element method," *Powder Technology,* vol. 310, pp. 104-142, 2017.

[107] B. Vasarhelyi, "Some observations regarding the strength and deformability of sandstones in dry and satruated conditions," *Bull. Eng. Geol. Env.,* vol. 62, pp. 245-249, 2003.

[108] *Technical Manual Rocky 4, DEM Particle Simulator,* ESSS Rocky, 2017.

[109] K. Senetakis, M. R. Coop and C. M. Todisco, "The inter-particle coefficient of friction at the contacts of Leighton Buzzard sand quartz minerals," *Soils and Foundations,* vol. 53, pp. 746-755, 2013.

[110] D. Schulze, Pulver und Schüttgüter, Berlin: Springer, 2009.

[111] A. Nikolopoulos, N. Nikolopoulos, N. Varveris, S. Karellas, P. Grammelis and E. Kakaras, "Investigation of proper modeling of very dense granular flows in the recirculation system of CFBs," *Particuology,* 2012.

[112] S. W. Churchill and H. H. Chu, "Correlating equations for laminar and turbulent free convection from a vertical plate," *International Journal of Heat and Mass Transfer,* vol. 18, pp. 1323-1329, 1975.

[113] E. U. Schlünder, "Heat transfer between packed, agitated and fluidized beds and submerged surfaces," *Chemical engineering communications,* vol. 9, pp. 273-302, 1981.

[114] T. F. Ozkaynak and J. C. Chen, "Emulsion phase residence time and its use in heat transfer models in fluidized beds," *AIChE Journal,* vol. 26, pp. 544-550, 1980.

[115] E. Tsotsas, "Heat Transfer from a Wall to Stagnant and Mechanically Agitated Beds," in *VDI Heat Atlas*, Düsseldorf, VDI Verlag, 2010, pp. 1311-1326.

[116] S. M. Derakhshani, D. L. Schott and G. Lodewijks, "Micro-macro properties of quartz sand: Experimental investigation and DEM simulation," *Powder Technology,* vol. 269, pp. 127-138, 2015.

[117] S. Kabelac and D. Vortmeyer, "Radiation of Surfaces," in *VDI Heat Atlas*, V. V. u. Chemieingenieurwesen, Ed., Düsseldorf, Springer, 2010, pp. 947-959.